THE UNIVERSITY OF CHICAGO

SILICON COMPATIBLE OXIDE PLATFORM FOR ENGINEERING RARE-EARTH QUBITS

A DISSERTATION SUBMITTED TO

THE FACULTY OF THE PRITZKER SCHOOL OF MOLECULAR ENGINEERING

IN CANDIDACY FOR THE DEGREE OF

DOCTOR OF PHILOSOPHY

BY

MANISH KUMAR SINGH

CHICAGO, ILLINOIS

MARCH 2022

To my family

TABLE OF CONTENTS

LIST OF FIGURES

LIST OF TABLES

ACKNOWLEDGMENT

I'm grateful to my advisor Prof. Supratik Guha who gave me the opportunity, guidance, and latitude to lead the road to discovery on an important problem. You have encouraged me to pursue areas that were outside my intellectual comfort zone – which in the end helped me develop the perspectives and expertise that have made this research successful and my years in the lab productive. During my first year, I remember that you half-jokingly said, "Manish, you're my first Ph.D. student. I don't know if that a good thing or not." As I look back, it has been the perfect thing – I come out of this program a more confident, more ambitious, and a better researcher.

Dr. Tijana Rajh and Prof. Tian Zhong were instrumental in introducing me to the fascinating world of quantum defects. Prof. Awschalom, Prof. High, and Prof. Bernien helped guide the research direction throughout the years. Alan Dibos, Michael, and Sean for helping demonstrate the potential of a scalable platform that has been the goal of my doctoral work. My work relied heavily on the support from engineers and scientists at the Center for Nanoscale Materials (CNM) at Argonne National Laboratory (ANL). Brandon Fischer for the XRD characterization techniques, David Czaplewski, Ralu Divan, and Suzanne Miller for the excellent training and support inside the cleanroom.

Abhinav Prakash, you taught me much about UHV, and working with you was a great confidence builder when it came to vacuum systems! I was also lucky to have Bhaskar, Jiyuan, and Vamsi as my cleanroom gurus. Joe Heremans, thank you for being incredibly easy to talk to and for enabling all the optical experiments at Argonne. Gary Wolfowicz, for being an incredible collaborator, this would have been an entirely different thesis without you. Sean Sullivan, Jonghoon Ann, and Katie Sautter, for sticking with me through some of the crazier experiments! Nazar Deegan, it's always fun to discuss any topic with you – thank you for being a friend.

My group was primarily at the Argonne National Laboratory, which meant that I did not have a lab group at UChicago when I started. I am grateful to the members of the Awschalom lab for being so inviting and for the incredible people I became friends with – Grant, Peter, Elena, Amy, Chris, Shobhit, Jonathan – you made both my research and life better.

For our next batch of "quantum engineers" in the Guha lab – Greg, Connor, Cheng, and Katie – I am confident that the REI doped system is in very capable hands and that the future developments will be fantastic.

Lastly, I'm eternally grateful to my parents for all their love, sacrifice, understanding, and support. I am thankful for my brothers and sister-in-law for their love and continuous encouragement. Sneha, your academic career and the knack for picking up the right gift have both been an inspiration! And, to my wife, Leigh, for her untiring support and love through everything.

ABSTRACT

Over the last few years, the realization of the quantum network has become a real possibility – with small networks already demonstrated using diamond NV centers[1]. Using entanglement distribution and bound by the laws of quantum physics, these networks offer unconditional security and the promise of scalable quantum computing. The key demonstration that has been accomplished used single qubits, but a scalable system will be needed to give a meaningful rate over such a network. This would comprise of 1000s or millions of qubits at each node in such a network – necessitating the development of a platform that could allow us to scale towards that goal. Rare-earth ions are a good candidate for solid-state qubit as their first excitation levels are 4f-4f transitions shielded from electrical fluctuations in the environment through the full 5s, 5p shell. A rare-earth ions-based platform that is silicon compatible would allow us to develop such scalable systems and a rare-earth-doped oxide offers an attractive option.

In what follows, I have used my three papers along with intervening chapters to present key results, challenges, and outlook on this platform development effort. Chapter 2 discusses the Er:Y_2O_3 effort – one of the key findings here was the role of undoped buffer layers on the top and bottom in reducing the Γ_{inh}. We also, somewhat surprisingly, discovered that the traditional measure of crystallinity in the inhomogeneity (XRD FWHM) didn't have a correlation with the Γ_{inh} - a more sensitive measure of the dopant's local environment. Chapter 3 discusses the Er:TiO_2 effort, where we have built upon the Y_2O_3 effort and have been able to demonstrate a higher degree of control over inhomogeneous and spectral diffusion. Chapter 4 dives into the nanofabrication techniques and challenges faced during development. Y_2O_3, being hard to etch material, showed serious issues that drastically limited the usefulness when considering device fabrication. TiO_2, on the other hand, was relatively easy to etch film, and that has enabled us to demonstrate devices fabricated

on this platform. As we continue the development and future optimization on this platform, it is important to probe the systems where technologies that we are developing will be used - chapter 5 does precisely that. By performing system-level analysis, we estimate that a system demonstrating a coherence time of >10 ms would enable us to distribute entanglement up to 1000 km. Providing an important benchmark that future iteration and development should aim for.

To summarize, we have shown that REI doped oxide thin films on silicon are a viable platform for the development of quantum technologies. In the outlook, I have identified avenues where challenges remain and try to paint a picture of what an integrated platform might look like.

1 INTRODUCTION

1.1 RARE EARTH ELEMENTS

The rare earths are a group of 17 elements in the periodic table that includes the 15 Lanthanides, Scandium, and Yttrium. In contrast to what the name suggests, most of the elements in the group are relatively abundant in the earth's crust, with Ce at ~68 ppm being more abundant than copper. The technological importance of these rare earths[2] comes from their use in modern electronics – cameras, computers, phones. A subset of these elements (Nd, Sm, Gd, Dy) is critical as high power permanent magnets – used widely in wind turbines. These are also useful in defense technologies such as lasers, guidance systems, radar, satellites, etc. Erbium plays a vital role in communication over optical cables. To underscore the importance, consider the geo-political issue surrounding rare earths: today's production primarily comes out of China, which, owing to the technological importance of these elements, has become identified as a "subject of concern" by other countries.

Quantum information, which can exist as a superposition of multiple states, needs a quantum memory for storage and retrieval – critical tasks for a network capable of distributing entanglement over long distances. Rare-earth ions (REI) have also emerged as a potential enabler of quantum technology, particularly as a memory for quantum information. Researchers have demonstrated long spin-coherence time in Eu and Er isotopes of over 1.3 s[3] and six hours[4] respectively – an indicator of the potential as a quantum memory. Our estimates show that a quantum memory of ~10 ms will be sufficient for most medium distance networks[5] (up to a thousand kilometers). This remarkably high coherence time is possible in REI because the transitions of interest in rare earths are 4f-4f transitions shielded from external electric fields because of the full 5s and 5p orbitals.

In addition to this common property, these elements offer additional unique properties. E.g., Yb isotope, due to the simplicity of its energy levels, allows for deeper physics, such as interaction with the other nuclear spins in the host, to be investigated[6]. Er has been another REI of interest because of its telecom emission. In addition to being candidates for quantum memory REI are also leading candidates that could allow for transduction of wavelengths between visible and microwave wavelengths[7], allowing for the microwave qubits used in leading quantum computing architectures to be sent over long distances.

1.2 OXIDES AS QUBIT HOSTS

To utilize several units to perform a complex operation, it becomes necessary that these units be as identical as possible. For engineered systems, this is generally made possible through extensive optimization of the manufacturing process to the point that a billion transistors on today's microchips perform have properties within a narrow distribution to perform computations in unison. When it comes to quantum information sciences (QIS), atoms serve as these templates – each atom defined by a given number of protons, neutrons, and electrons behave identically to every other atom with the same configuration. It is little surprise then that the first demonstrations of key QIS milestones – quantum gates, entanglement swap, etc. – were performed on trapped ion systems[8–10]. Trapped ion systems have emerged as one of the leading ways to perform quantum computing as being commercialized by companies like IonQ and Honeywell – with (currently) a small number of qubits (~100) manipulated with remarkable fidelity in control and operations. However, these face several hurdles when scaling up to millions of qubits[11]. The other popular method uses superconducting microwave qubits[12] (IBM, Google, etc.), which offers a path to scalability but suffers from some challenges arising from the material variability in the metal/AlOx/metal Josephson junction used in these devices[13]. REIs in oxide could play a

significant role in both these challenges of scale and variability – oxides serve as a "solid-state vacuum." As we show later, for the qubits of interest, we can engineer the properties of these qubits through the thin film hosts and bring them close to demonstrated properties in bulk hosts. The thin film form factor is essential as it would allow us to take advantage of decades of progress in semiconductor fabrication technology, making it a massively scalable platform. The diamond NV center has been a front runner in the solid-state qubit category and has been a popular system for the quantum experimentalists – the initial experiments closely followed that trapped ion demonstrations and have informed and helped accelerate the rare-earth ion-based investigations currently underway in many labs across the world. Figure 1 shows the comparative trajectory of the three qubits systems.

When it comes to oxides, their development and in-depth study of oxide properties got a major technological push during the late 1990s, and early 2000s, driven by the need to replace SiO_2 then used as the primary gate oxide in CMOS transistors. As a result, many studies exploring the growth, electrical properties, and interface effects in great depth are now available in the literature. The large existing body of research makes for a low barrier of entry when exploring oxides as the host material for REI-based qubits. We chose to work with erbium as the dopant because, from a long-distance communication perspective, erbium, with its first emission in the telecom C-band (1530-1565nm), is a prime qubit candidate.

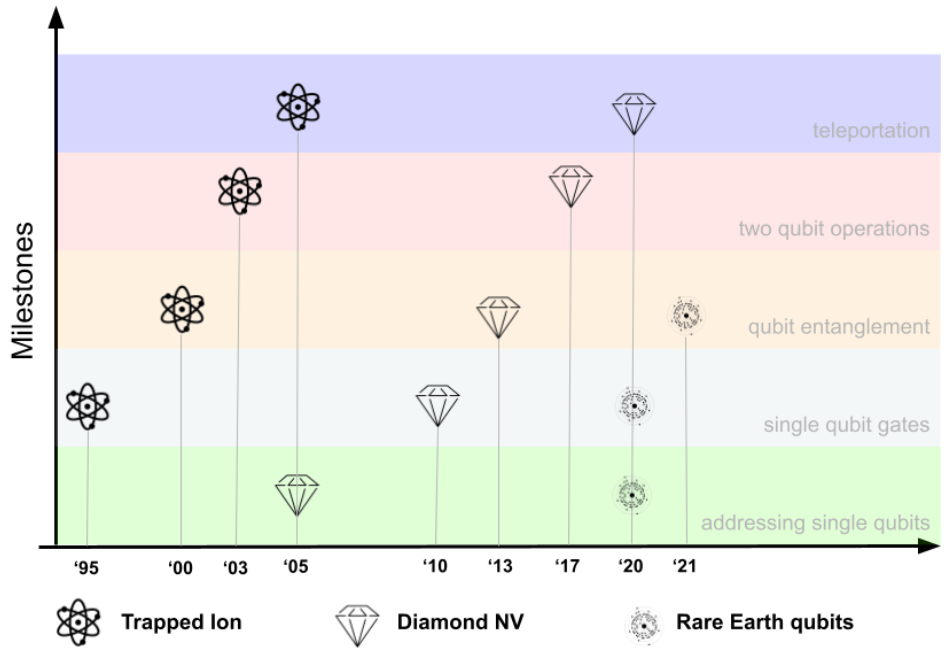

Figure 1 A comparison of the timeline over which key demonstrations in three systems were performed – (a) Trapped ion, (B) Diamond NV centers, and (C) rare earth qubits. While the demonstrations for REI are still underway, the accelerated trajectory – primarily driven by our learnings from the other systems - is apparent.

This Ph.D. work aimed to evaluate oxides as a host for erbium (a rare-earth qubit). As a part of my work, we have explored Y_2O_3, TiO_2, strontium titanate (STO), CeO_2 as hosts for erbium. Large band-gap oxides are preferred as they allow for transparency over a wider range of frequencies. We selected Y_2O_3 as our first target due to its compatibility with erbium (ion size, crystal structure, oxidation state, etc.) and because growth expertise was available in our lab. TiO_2 became an option due to encouraging reports in literature from other groups that showed the bulk rutile crystal to be a promising host for implanted erbium. STO has some very interesting properties at low temperatures (phase transition, ferroelectric properties) that could be used for qubit control, and CeO_2 as an inert host is another strong potential candidate. I have led the work on the first two – the description of which will form the bulk of this thesis – and enabled the work with the other two (currently led by my colleagues in Guha lab).

1.3 GROWTH TECHNIQUES

Today, metal oxides power a whole array of technologies built on the wide spectrum of magnetic, electric, thermal, and optical effects (e.g., non-linear effects). It is little surprise that an extensive array of methods has been developed to grow and engineer the properties of these oxides. We will describe the four most widely used techniques in the context of the work described here. The primary difference between them being (1) The typical mean free path of the chemical species (2) the variety of chemical species present during the deposition process

1.3.1 Sputtering

Sputtering is a widely used physical deposition method. It works by bombarding high-energy heavy ions (typically Argon) onto a pure metal or oxide target. This momentum transfer ejects atoms from the target material, which gets deposited onto the desired substrate (Silicon, glass, etc.). It becomes essential that there is a long enough mean free path of the impacting ions and the ejected atoms from the target; for this, Sputtering is performed at low pressures (typically $<10^{-4}$ Torr) – which corresponds to a mean free path longer than 10 cm. One variation on this method, reactive sputtering, allows for oxidation (nitridation) and stoichiometry control by adding an oxygen (nitrogen) plasma during the growth process and controlling the flow rate of these gases. Another variation called co-sputtering refers to the ability to deposit two or more materials from different sputter targets simultaneously. Figure 2 shows the schematic for a typical sputter chamber is. The flow rate of the gasses is controlled via a mass flow controller, and a computer-controlled gate valve on a cryo or turbo pump mounted onto the reaction chamber dynamically controls the in-chamber pressure. The plasma power, flow rate, mean free path, and substrate temperature forms the optimization parameter set for optimizing the growth process.

Due to the physical, line-of-sight nature of the deposition, deposition conformity on existing features is poor and is a major drawback of the process. However, the ability to use an external target allows us to use very high purity bulk material as targets for deposition. Process & equipment simplicity makes this a cheaper deposition process (compared to CVD, ALD) and sputtering the method of choice for many applications.

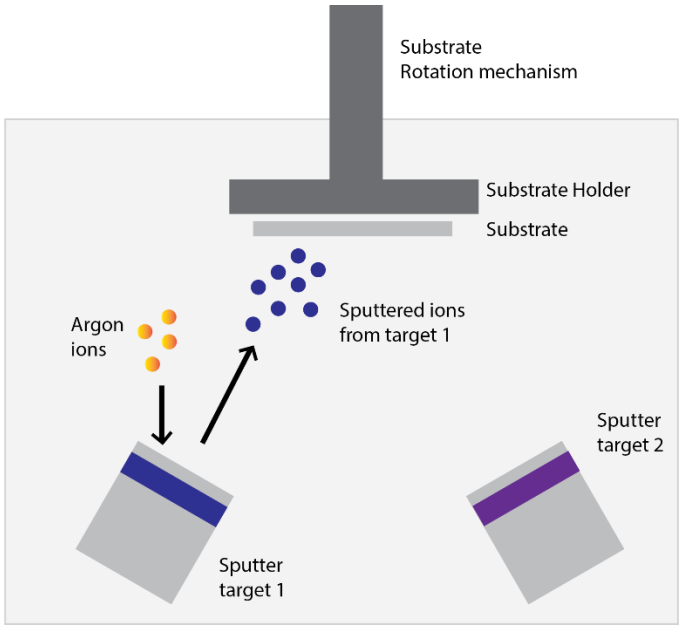

Figure 2 Schematic of a sputter deposition chamber. A heavy ion (like Argon) is accelerated. This physical impact ejects atoms off the target materials, depositing them on the substrate of choice kept in proximity.

1.3.2 Chemical Vapor Deposition (CVD)

A typical CVD process relies on the decomposition of chemical precursors through reaction with other gases on the substrate to produce the desired film on the process. In a high vacuum, controlled environment with a high mean free path, it is likely that the chemical reaction will happen on the substrate and during the flight of the molecules. The method is only viable for precursors that have volatile by-products (low molecular weight molecules) that can promptly desorb from the substrate surface, allowing for further deposition of the desired compound. Variations include plasma-

enhanced CVD, which use plasma to enhance the chemical reaction, and MOCVD, which covers the use of metal-organic precursor in the CVD process. Substrate temperature, flow rates, plasma power, are important optimization parameters.

Due to the need for specialized precursors, the costs associated with the CVD process are in general higher than the sputtering process. However, the line-of-sight requirement is not there, allowing for batch processing; the conformity with existing structures is better. It gives a higher degree of control over the growth process and, through careful optimization, offers a method to grow high-quality crystalline material – notably in the case of lab-grown diamond (CVD process).

1.3.3 Atomic Layer Deposition (ALD)

Films deposited by CVD and sputter exhibit high pin-hole density – this results in limits to electrical behavior, thereby limiting technological application. Historically, this is seen as a key driver for the development of an alternate method for thin-film deposition[14]. ALD works on the principle of self-limiting saturation of the substrate surface by the precursors – in the reaction chamber, the substrate is exposed to alternate reaction species. For example, in the case of Al2O3 deposition using the precursor trimethyl aluminum (TMA) and H2O as the oxidizer goes through the following steps (1) the substrate (with an OH termination) is exposed to a cycle of TMA – this saturates the substrate surface via dissociative absorption (2) A purge with an inert gas (e.g., Argon) removes all the residual TMA (3) H2O is introduced as an oxidizing agent – this results in the formation of hydroxylated Al2O3 (4) A purge with an inert gas removes residual H2O and byproducts. This is shown in figure 3. And the cycle repeats again, depositing a monolayer of Al2O3 with every cycle. Important optimization parameters include the substrate temperature and the residence time. Variations on the method include thermal ALD (control of substrate

temperature) and plasma ALD (e.g., using oxygen plasma for oxidation), among other specialized variants.

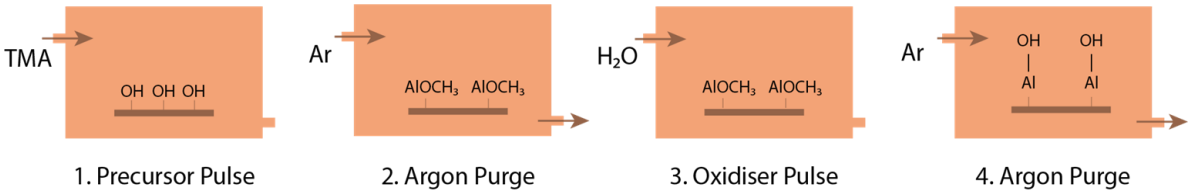

Figure 3 the deposition of a monolayer of Al2O3 thin films using trimethyl aluminum (TMA) as a precursor and H2O as the oxidizer is a 4 step process. In step 1, TMA is introduced into the reaction chamber (with a hydroxyl-terminated substrate (grey)). This is followed by a purge with argon which removes any residual TMA (step 2). This, in turn, is followed for the introduction and purge of the oxidizer (steps 3 & 4). At the end of step 4 we have a hydroxyl-terminated oxide layer, ready for step 1 – the process can be repeated to get the desired film thickness. The typical growth rate is ~0.1nm per cycle.

1.3.4 Molecular Beam Epitaxy (MBE)

The "beam" in MBE refers to the capability to obtain a "beam" of atoms that traverse the distance between source and substrate without collision with environmental elements. Inside the reaction chamber of an MBE, a combination of cryo and turbopumps gives a background pressure of $<10^{-9}$ Torr to get to ultrahigh vacuum (UHV) – this corresponds to a mean free path of >1 km. This low standby pressure removes or limits any background contamination (typically carbon) during the growth process. Additionally, a cryo shroud with liquid nitrogen prevents stray atoms from scattering off the chamber wall and redepositing on the substrate during growth. Together these measures allow for direct reaction at the substrate allowing for a great degree of control over epitaxial growth. This crucial capability has played a central role in the early demonstration of several material systems in semiconductor and laser development.

An MBE chamber's design allows us to incorporate several sources of precursors using specialized sources or cells to this growth chamber. One of the most commonly used types is the Knudsen cell (also referred to as the effusion or doping cell) for the high-temperature evaporation of metals. It

produces a steady beam of atoms from very low vapor pressure materials with some designs capable of heating the source to 2000 °C. Using variations on this principle and a range of crucible materials, we can incorporate high vapor pressure metals and sources into an MBE setup. E-beam sources are also used to evaporate high melting point materials like Ti or easily oxidizable materials like Si. On the other hand, in high-vapor pressure, metal-organic precursors can be introduced using an external precursor source and a diffusor cell. This has allowed the community to bring in a new set of capabilities through metal-organic MBE or MOMBE and is of interest for complex oxides such as $BaSnO_3$[15].

The schematic in figure 4 shows the standard components of an MBE. The most important is the reaction chamber, on which we have a large cryo and a large turbopump to achieve UHV static pressure. The substrate is suspended from the top using a rotation mechanism - the deposition surface faces down towards the sources. Heaters on this mechanism, with a filament made of graphite in our case, provide control over the substrate temperature going all the way to 1200 °C. An electron gun mounted on the chamber aligned with the substrate holder provides in-situ feedback on material growth. Shutters on all active sources and surfaces offer another layer of control over the deposition. Sources towards the bottom of the chamber provide the “molecular beam” of precursors during growth – the beam flux is monitored using a beam flux monitor (a particular type of ion gauge) inserted into the chamber for measurements and retracted for growth. Finally, we have a cryo-shroud at the bottom of the chamber (blue) filled with liquid nitrogen during a run. The substrate transfer itself happens through a load lock chamber which in our case is attached to a transfer chamber – a central hub with a robotic arm that allows us to move the substrate from load lock to a degas chamber before transferring to the main chamber for growth.

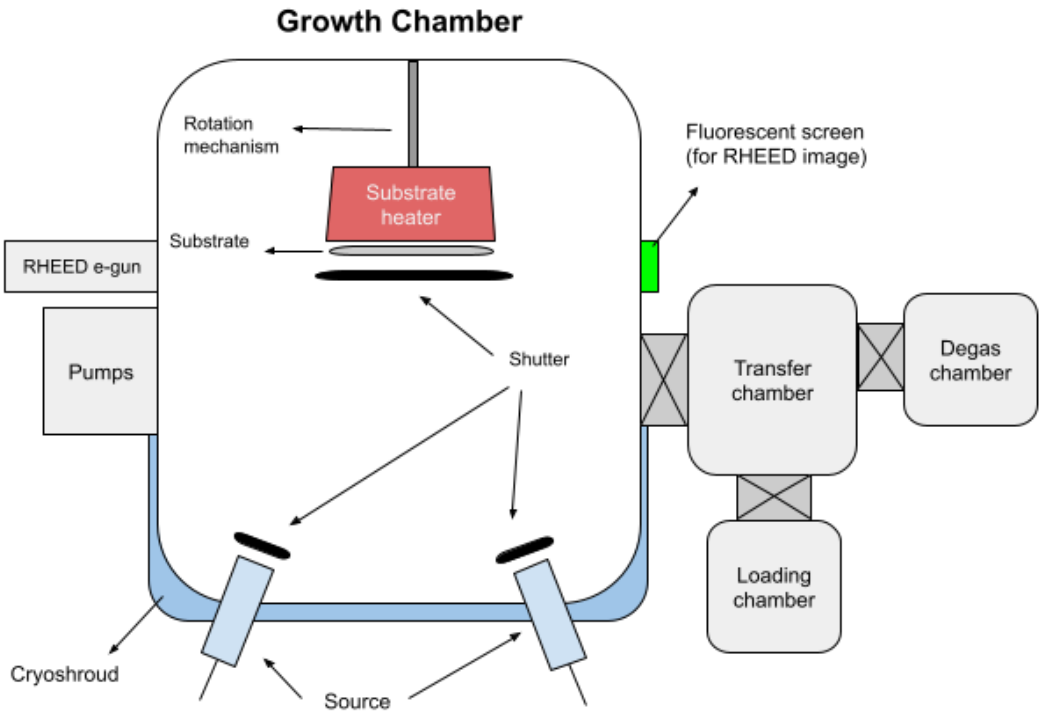

Figure 4 Schematic of a typical MBE chamber. A combination of chambers is used to isolate and protect the growth chamber. Cryo and turbopumps on the growth chamber ensure a low background pressure. In our tool, the substrate is suspended from the top with a heather backing; sources from the bottom supply the material for film growth. In addition, an e-gun allows us to perform in-situ characterization of the film growth using the reflected high energy electron diffraction (RHEED) technique.

1.4 CHARACTERIZATION OF THIN FILMS

The films that we had planned to grow for this research were primarily binary oxides doped with erbium on substrates with and without the epitaxial matching conditions – this included growth on silicon (Si (100) and Si (111)), strontium titanate (STO), r-plane sapphire, CeO2 substrates. There were two sets of metrics that we needed feedback on – one targeted the host thin film: crystallinity, lattice matching condition, the film/substrate interface, surface roughness, optical loss, etc. and the other targeted the behavior of the erbium atoms added to the films during the growth – this included emission lifetime, site substitution, emission frequency, inhomogeneity in individual erbium environment, spectral diffusion, etc. Several characterization methods were employed to complete

these two sets of characterizations – shown as I & II in figure 5. They are described below, focusing on how each method added to our understanding of this system.

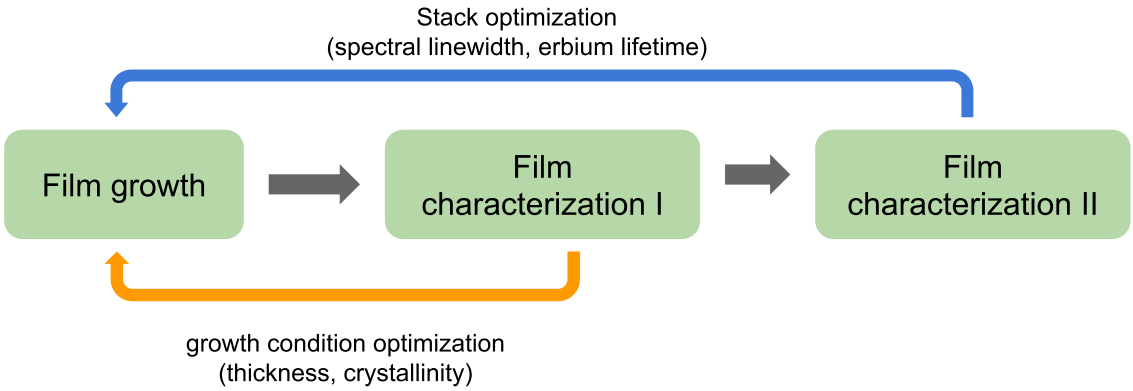

Figure 5 Process Loop for growth optimization. For our films, we used two sets of film characterization. Feedback from the first set (orange) allowed us to optimize the growth condition and develop control over film thickness, crystallinity, etc. Feedback from the second, more time taking set (blue line) guides us on optimization of dopant properties.

1.4.1 Reflected high energy electron diffraction (RHEED)

RHEED is a popular in-situ characterization technique for high vacuum chamber material growth and is employed routinely in MBE setups. The method uses high energy (5-100 keV) electron beams incident on the surface at a low angle of incidence (<1°). This small angle limits the penetration depth to a few monolayers. It gives diffraction and intensity oscillations that contain crystallinity and monolayer growth information, making it an excellent tool for in-situ characterization. The diffraction pattern results from the wave nature of electrons and the periodic arrangement of atoms, and the intensity oscillations result from monolayer by monolayer growth.

The unit cell of a crystal defines the lattice in the real space, bound by the condition of constructive interference; a corresponding reciprocal lattice can similarly be defined in momentum space. For a given wavelength, a geometric construction called the Ewald sphere is used to predict the diffraction pattern. The sphere construction is a result of the elastic scattering assumption, in which

case the incident and reflected beam have the same energy and thereby the same length; this them implies that the diffraction will only occur at the points on the Ewald sphere. The incident wave vector and the reflected wave vectors are represented in figure 6.

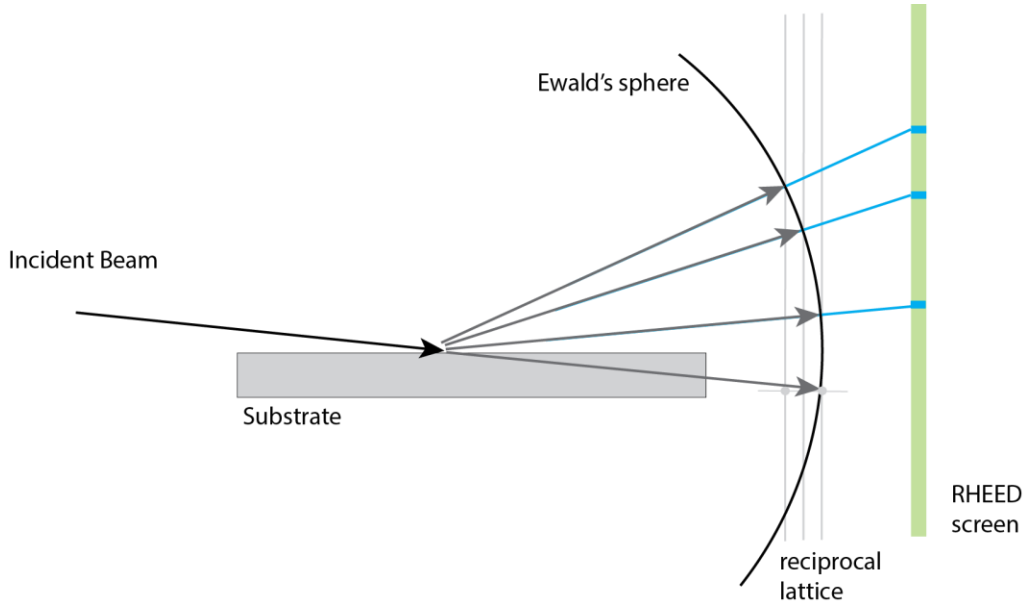

Figure 6 A high-energy e-beam is incident on a substrate, and the elastic diffraction results in a pattern on the fluorescent screen. This pattern corresponds to the points in the allowed diffraction condition and thereby the reciprocal lattice, giving direct information about the lattice structure and crystallinity.

An example of the power of in-situ characterization is shown in figure 7. In 7(a), we have a TiO_2 film that is being grown at the rate of ~1nm/min. At t=0, we start doping the films with a high concentration of erbium (est. 3500 ppm). This changes the crystalline structure, which can be observed directly within a few min – figure 7(b) shows the RHEED after 5.5 min of high concentration erbium doping – the pattern has become diffused, indicative of an amorphous growth. We see in figure 7(c) that the polycrystallinity of the film has been restored at t=20 min, which is 7 minutes after stopping the erbium growth.

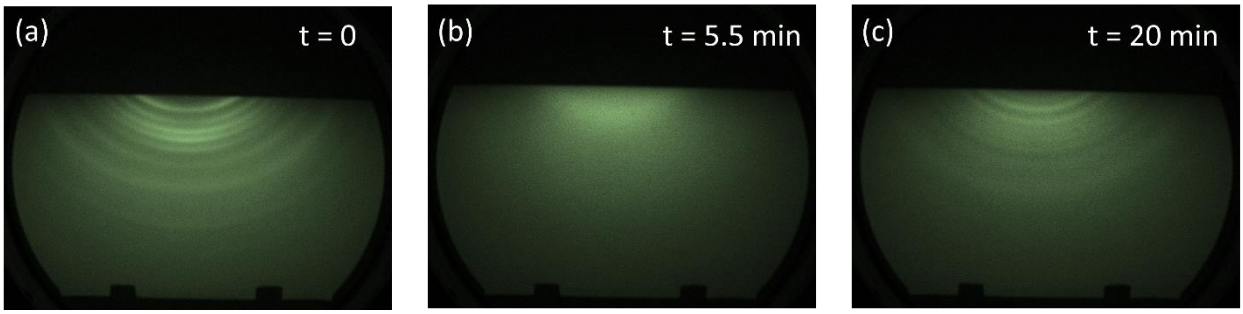

Figure 7 (a) RHEED image of an undoped TiO2 thin after ~50nm of growth. (b) Five minutes after doping with ~3500 ppm of erbium, the RHEED pattern shows clear change indicating amorphous growth (c) 7 minutes after stopping the erbium doping, the rings corresponding to the polycrystalline structure has returned.

1.4.2 X-Ray Diffraction (XRD)

X-Ray is the term used for electromagnetic radiation in the 10 pm – 10 nm range. The typical wavelength of the X-Ray used in modern setups is 1.54A, corresponding to $Cu\ k\alpha_1$. The small wavelength allows us to probe the nature of the separation between layers of atoms arranged in a crystalline structure (typical unit cell size ~0.5-1nm), giving us information on film crystallinity, thickness, and strain based on peak position. Bragg's law used to explain the interference pattern obtained using XRD is summarized as

$$n\lambda = 2d \sin(\theta)$$

Where n is an integer, λ the wavelength of the X-Ray, d is the distance between parallel atomic layers, and θ is the angle of incidence of the X-Ray. Constructive interference only occurs when Bragg's condition is satisfied and knowing the θ and λ, d can be estimated. For well-characterized materials, experimental data can be compared to the existing database, and the stoichiometry and strain be determined. d is related to the crystal structure (as described by the miller indices [h, k, l] through the following relation (for the case of a cubic structure with a unit cell of size a)

$$d = \frac{a}{\sqrt{h^2 + k^2 + l^2}}$$

1.4.3 Scanning electron microscopy (SEM)

In SEM, a focused beam of high energy (few keV) electrons is directed onto the sample surface and are subsequently scattered and detected. By collecting the incident energy and the detector signal strength (following scattering), an image revealing the sample's topography is generated. This signal is from the secondary electrons generated by the atoms impacted by the high-energy incident beam in a typical setup. Since the energy is lower, these secondary electrons that are detected come from the surface of the sample.

Due to the direct electron incidence, one limitation is the requirement of electrical conductivity in the sample being imaged. Charging of insulators (such as oxides) is common and is typically overcome using methods like a conductive tape or silver paste – these methods, however, damage the sample making SEM a “destructive” technique in some cases. A user also needs to be mindful of stigmatic correction, which might produce distorted images.

This technique was used extensively to image nanofabricated devices and provide feedback on important metrics like etch rate, angle etc.

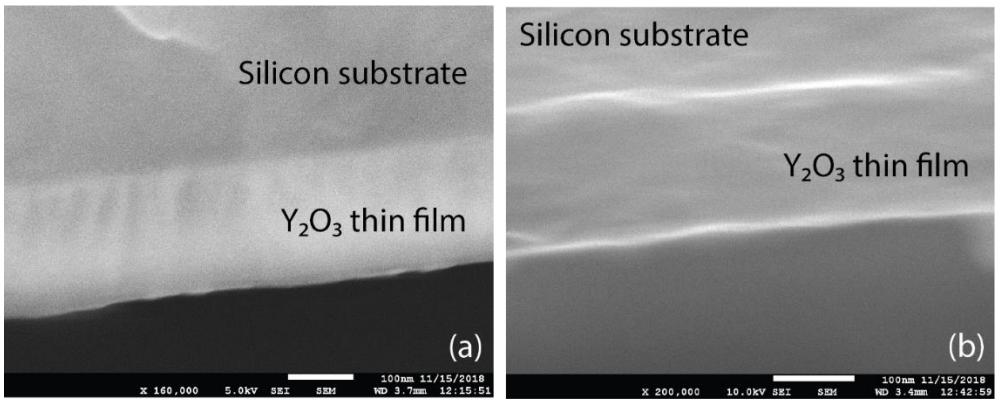

Figure 8 (a) SEM image showing Y2O3 thin film on a silicon substrate. Y2O3 with a higher resistivity shows up as brighter than the silicon substrate, allowing us to use this as another measure of film thickness. The image was taken at an energy of 5 keV. (b) charging effects (bright lines) bordering the Y2O3 film become clearly visible when the beam energy is increased to 10 keV.

1.4.4 Tunneling electron microscopy (TEM)

A TEM uses a focused e-beam to image specially prepared samples with very high resolution and is typically employed for studying the films, interfaces, elemental analysis via electron energy loss spectroscopy (EELS), or energy-dispersive x-ray spectroscopy (EDS), etc. With our collaborators, we performed a cross-sectional analysis of the thin film. For sample preparation, the substrate is cleaved along a crystal plane, and then using ion-milling, polishing, or a combination of both, is thinned down to a point where it is transparent to the electron beam (<100 nm). Cross-sectional analysis using TEM has been crucial in our studies for confirming the crystal structure, epitaxial relationship, and the nature of the film/substate interface. Elemental analysis of post-processed films using EDS has been especially important in understanding the effect of post-processing dry etch of the TiO_2 films for device fabrication.

1.4.5 Atomic force microscopy (AFM)

Unlike SEM and TEM, which rely on the use of focused electron beams, am AFM relies on physical sensing. Using a cantilever (with the AFM tip), any force interaction between the tip and the sample surface is measured via a laser deflection off the top of the cantilever. The measurements can be very accurate; however, some artifacts may arise depending on the age of the tip used for characterization. Figure 9(a) shows an AFM of a TiO2 film on silicon where the prominent triangular features are simply a result of using an old tip on a shared AFM tool. Figure 9(b) is another image of a similar film with a new tip.

This technique was used to characterize film roughness – as it is important for the scattering loss in waveguide-like structures.

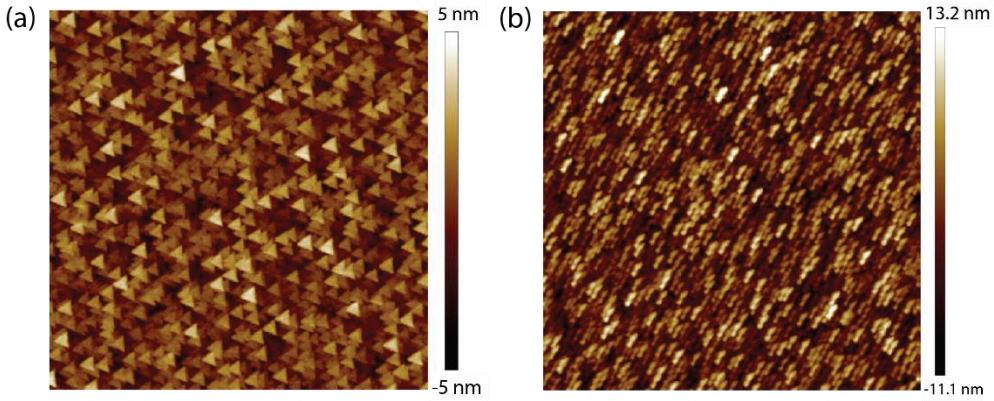

Figure 9 Damage to the AFM tip can introduce artifacts in the scanning that can severely reduce the measurement accuracy and introduce features unrelated to the film surface.

1.4.6 Ellipsometry

This is another method that is used to characterize thin films. An ellipsometer works by using polarized light and detecting changes in the polarization to determine film properties like thickness, refractive index, etc. Polarized light is incident onto the film, and the change in the s and p component is measured by the detector

$$\rho = \frac{R_p}{R_s} = \tan(\Psi)\, e^{i\Delta}$$

Here, R_p, R_s are the p & s components after reflection; $\tan(\Psi)$ captures the change in amplitude and $e^{i\Delta}$ the change in phases following reflection from the film. In work reported here, ellipsometry was used to characterize the films grown directly on silicon and to characterize multi-layer formed from depositing the hard mask on top of the films.

1.4.7 Electron paramagnetic resonance (EPR)

This is an important method that can be used to study materials that have at least one unpaired electron. In the presence of an external magnetic field (B), the energy is given by:

$$E = m_s g_e \mu_B B$$

Where m_s is the magnetic spin, m_s the g factor and μ_B is the Bohr magnetron. Without the application of the electric field, the two spin states ½ and -½ are degenerate; however, the application of a field creates an energy difference $\Delta E = g_e \mu_B B$ that increase with the magnetic field (shown in the figure below). A simultaneously applied microwave field with energy equal to this difference results in an electronic transition that can be recorded. For this condition, we need $\Delta E = g_e \mu_B B = h\nu$. Out of all the terms in this equation g_e is the only unknown, and the rest are either constants or controlled experimental parameters. For crystalline material, the full g-factor tensor can be characterized by performing the experiment with different combinations of the crystal plane and magnetic field.

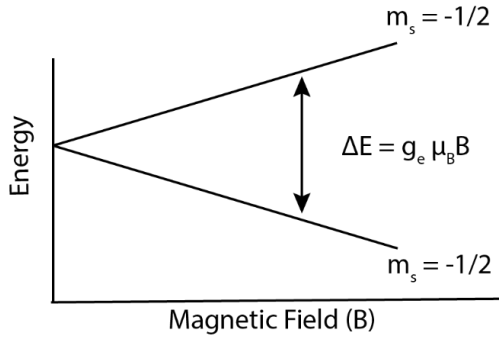

Figure 10. A schematic showing the difference in energy for the two spin states with the application of magnetic field

1.4.8 Photoluminescence (PL)

Photoluminescence is a powerful tool for characterizing optically active defects and has been used extensively used for the set of metrics identified in "Film Characterization II" in figure 5. In the materials described in this thesis, the erbium is investigated as the defect of interest and is excited using off-resonant and on-resonant pulses for different experiments. The off-resonant excitation wavelength can be selected based on the energy levels that we want to investigate. We were primarily interested in the $^4I_{15/2}$ to $^4I_{13/2}$ transition in erbium (~5700 cm^{-1}), which was investigated

using a 905 nm laser (9360 cm^{-1}) with energy higher than the level of interest but smaller, so the higher levels are not excited. For obtaining the spectrum from the energy levels, the off-resonant excitation is incident on a grating and is then on to the liquid nitrogen cooled InGaS detector. The peaks resolution from a spectrometer is limited by the grating but is useful in identifying the peak positions.

Resonant excitation is used to get the inhomogeneous linewidths for the peaks of interest. This is accomplished using a tunable laser and creating laser pulses using acusto-optic modulators. The output is then directed to a single photon nanowire detector (SNSPD). The inhomogeneous linewidth is an envelope of all the homogeneous linewidths, and the FWHM gives a measure of inhomogeneities in the local environment of individual erbium atoms.

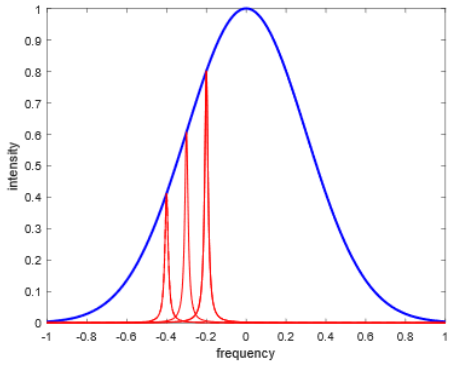

Figure 11 Homogeneous linewidths are represented by Lorentzian curves (red). During a laser scan across the resonance frequency, we get an envelope of all the homogeneous peaks with different centers - giving what is called the inhomogeneous broadening curve (blue).

Another method that we have employed is spectral hole burning which can be used to measure spectral diffusion. By using a resonant laser with a small linewidth, an ensemble of atoms can be removed from the population, creating a "hole" – this schematic is shown in figure 12. This is typically much narrower than inhomogeneous linewidth and allows for more sensitive measurements of local environments.

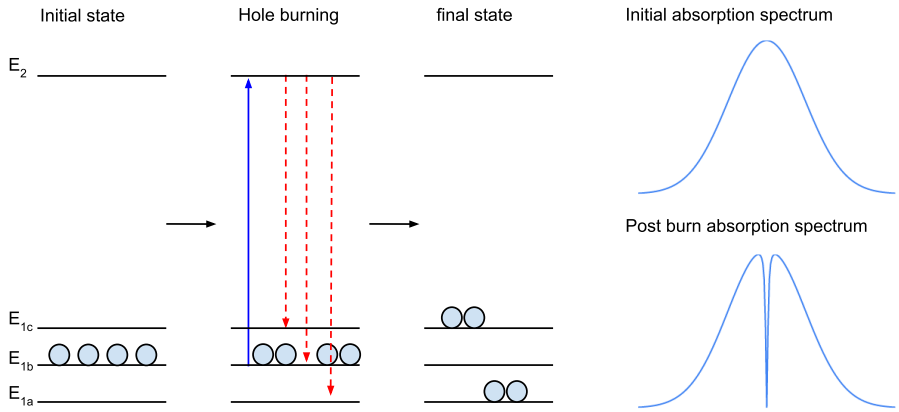

Figure 12 Schematic of the hole burning process. The series of figures on the left represents the ground state, excitation by narrow laser, and post-burn state. The representative absorption spectrum given on the right shows the "hole."

1.5 PLATFORM DEVELOPMENT

We started with an ambitious plan that laid out a roadmap for the development of a wafer-scale, telecom compatible platform. The capstone of this original plan was the demonstration of quantum memory on this platform, a goal that couldn't be achieved in the stipulated amount of time due to unforeseen hurdles that included a pivot from the originally proposed Y2O3/Si platform to the TiO2/Si platform and the great COVID-19 pandemic which is well into its third year as I write this thesis. Nevertheless, TiO2 on silicon was a successful pivot which has led to a number of insights in the REI doped oxide system, as discussed in Chapter 3. The goal of this work was to explore, via material engineering, if we could create an REI doped oxide thin film platform that was compatible with the CMOS processes and had properties comparable to that of bulk oxides. We have largely succeeded in this goal. Our capstone now is the demonstration of a high Purcell enhancement via 1D nanophotonic devices – developed working with our collaborators.

For execution, I identified three stages. First was the development of processes and optimization to get a reliable growth rate on the materials of interest – this includes film characterization

techniques such as RHEED, XRD, TEM, etc. Second, the characterization of the quantum relevant properties – the inhomogeneous linewidth, spectral diffusion, and a Hahn-echo measurement. This would provide feedback to the first step and result in further optimization. They are listed as separate as they involved capabilities across multiple labs – growth capabilities in Guha lab and characterization capabilities in our collaborator's labs, and each represented its own independent set of challenges. The final step – the capstone – was the development of devices on this platform. This was the most formidable challenge as it was also furthest removed from our core capabilities and required us to develop close functional collaborations. The challenge came from two sources: one, quantum photonics is in a nascent stage with the protocols and setups primarily in the leading laboratories across the world. While we were building on an existing body of research on thin-film/bulk characterization and nanophotonics – capabilities and methods had to be developed simultaneously for characterizing a low-intensity defect like erbium. And this necessitated long optimization cycles on both the material and simulation/fabrication sides. The challenges, progress, future goals, and outlook is discussed in detail in the following chapters.

2 EPITAXIAL ER-DOPED Y_2O_3 ON SILICON FOR QUANTUM COHERENT DEVICES

Manish K. Singh[1], Abhinav Prakash[1, 2], Gary Wolfowicz[1, 2], Jianguo Wen[2], Yizhong Huang[1], Tijana Rajh[2, †], David D. Awschalom[1, 2], Tian Zhong[1, †], Supratik Guha[1, 2, †]

[1]Pritzker School of Molecular Engineering, University of Chicago, Chicago, IL, USA, 60637

[2]Argonne National Laboratory, Lemont, IL, USA, 60439

[†]Corresponding authors: Supratik Guha (guha@uchicago.edu), Tian Zhong (tzh@uchicago.edu), and Tijana Rajh (rajh@anl.gov)

 The published manuscript is available at DOI: 10.1063/1.5142611

2.1 ABSTRACT

Rare-earth ions have incomplete 4*f* shells and possess narrow optical intra-4*f* transitions due to shielding from electrons in the 5*s* and 5*p* orbitals, making them good candidates for solid-state optical quantum memory. The emission of Er^{3+} in the telecom C-band (1530 nm – 1565 nm) makes it especially attractive for this application. In order to build practical, scalable devices, the REI needs to be embedded in a non-interacting host material, preferably one that can be integrated with silicon. In this paper, we show that Er^{3+} can be isovalently incorporated into epitaxial Y_2O_3 thin films on Si (111). We report on the synthesis of epitaxial, single-crystalline Er:Y_2O_3 on Si with low inhomogeneous linewidth in the photoluminescence spectra – 7.9 GHz at 4 K (5.1 GHz at 7 mK) and an optical excitation lifetime of 8.1 ms, paving the way for monolithic fabrication of quantum coherent nanophotonic devices for potential quantum memory applications. The choice of Y_2O_3 was driven by its low nuclear spin and small lattice mismatch with Si. Using photoluminescence (PL) and electron paramagnetic resonance, we show that Er^{3+} substitutes for Y in the crystal lattice. The role of interfacial SiO_x, diffusion of silicon into the film, and the effect of buffer layers on inhomogeneous PL linewidth are examined. We also find that the linewidth decreased monotonically with film thickness but, surprisingly, exhibits no correlation with the film crystalline quality as measured by the x-ray rocking curve scans suggesting other factors at play that limit the inhomogeneous broadening in Y_2O_3 films.

2.2 INTRODUCTION

The need for quantum memory devices has been increasingly apparent in networked coherent quantum systems that use an optical quantum communication link within a distributed network of processors or a secure communication network that uses quantum repeaters[16–18]. The role of a quantum memory is to store quantum information during entanglement events, and multiple mechanisms and systems for storage have been identified by researchers[19,20]. A promising and convenient approach among them is to use the spin-optical interfaces of rare-earth ions (REIs)[21–26]. Rare-earth ions have full 5*s* and 5*p* orbitals that shield the inner 4*f* levels from the local environment resulting in narrow 4*f*−4*f* electronic transitions. This shielding results in a low spectral diffusion not achievable in other systems such as the nitrogen-vacancy center defects[25]. Additionally, they are well suited for the development of coherent microwave to optical transduction[27]. These properties make REIs ideal for the solid-state optical quantum memory system, provided they can be embedded in a sufficiently inert (low nuclear spin and no unpaired electrons) solid-state host material and are capable of being modulated electrically or optically in an efficient manner. Among REIs, Er^{3+} is particularly attractive since it has an optical transition (~1535 nm for $^4I_{13/2} \rightarrow {}^4I_{15/2}$) that lies in the telecom C-band (λ = 1530 nm – 1565 nm), enabling the use of existing in-ground fiber links and leveraging the extremely low transmission loss in this wavelength range (0.2 dB/km).

So far, efforts to study the properties of active REIs in crystalline host materials[28,29] have focused on bulk crystals such as yttrium orthosilicate (Y_2SiO_5 or YSO), yttrium vanadate (YVO_4 or YVO), and yttrium aluminum garnet ($Y_3Al_5O_{12}$ or YAG). These studies have demonstrated long coherence times for the hyperfine transitions in these host materials – coherence time is a key metric for the duration that quantum information can be stored in a system. Recent work, using a

combination of methods, has demonstrated a hyperfine coherence time of 1.3 seconds (T = 1.4 K, B = 7 T) in an Er^{3+}:YSO host[30] and over 6 hours (T = 2 K) for Eu^{3+} [4]. Recent studies have also demonstrated nanophotonic devices that can be used to isolate single atoms in these systems. For instance, Dibos et al.[21] explored fabricating an evanescently coupled structure out of silicon and stamping onto the bulk. A different approach used focused ion beam milling to create nanobeam structures from bulk crystal[31]. These demonstrations show the promise of REIs, but they are limited by bulk platforms and fabrication methods that are not scalable. From a device perspective, deployment of REIs for quantum memory needs a convenient and scalable means of interrogating the REI—i.e., *storing* a qubit and *retrieving* it from memory.

One way of accomplishing scalability and compact operability is via the use of Er^{3+} ions embedded in a thin film solid-state host that can be integrated on a silicon platform, enabling potential integration with silicon photonic components and fabrication of low mode volume, high Q-factor compact resonators, and electronics that will enable us to address the hyperfine states. This is the objective of the current research, and in this paper, we explore and evaluate the microstructural, chemical, and optical properties of Er^{3+} in epitaxial oxide heterostructures on Si wafers for their suitability in scalable quantum memories. The host material is preferred to be single-crystalline to minimize heterogeneous variations in the environment surrounding embedded REI ions that are expected to induce additional spin-lattice, spin-spin relaxation pathways and reduce the optical and spin coherence times. There are a few considerations that govern the selection of good host material for optically active REIs –

(i) A cubic host is preferable with low lattice mismatch between the host material and silicon for high−quality epitaxial growth and silicon integration,

(ii) Low or zero nuclear spin is preferred in the host material,

(iii) Isovalent incorporation of the REI ion at a substitutional site, and

(iv) Low optical loss or absorption in the telecom band

When considering Er^{3+}, several rare-earth sesquioxides satisfy criteria (i) and (iii) (small lattice mismatch and isovalence). Among these, the lowest nuclear spin is offered by Y_2O_3, Gd_2O_3, Tb_2O_3 with nuclear spins of 1/2, (0, 3/2) and (0, 3/2) respectively, along with lattice mismatches of -2.4%, -0.48%, and -1.22%. The ionic radii of Y^{3+} and Er^{3+} are similar (Shannon radius of 102 pm and 103 pm respectively) and therefore, local strain effects are expected to be minimal. Additionally, as yttrium has only one stable isotope with ½ nuclear spin, it provides a *uniform* distribution of nuclear spins around Er^{3+} ions. These properties make Y_2O_3 an attractive host material for erbium.

While the growth of epitaxial Y_2O_3/Si structures has been studied before using both MBE [32,33] and pulsed laser deposition techniques (PLD)[34,35], Er-doped Y_2O_3 ($Er:Y_2O_3$) and the evaluation of such heterostructures for quantum memory and related devices has remained unexplored. In this paper, we demonstrate the successful epitaxial growth of $Er:Y_2O_3$ on Si (111) substrates and carry out a detailed microstructural and optical characterization study of these films. Through careful optimization of the growth conditions, we show that narrow photoluminescence inhomogeneous linewidths (7.9 GHz at 4 K, 5.1 GHz at 7 mK) for the first optical transition of Er^{3+} can be obtained, indicating that Y_2O_3 epitaxial films can act as an inert, high quality host for Er^{3+}. The hyperfine levels from the 7/2 nuclear spin isotope of Er (^{167}Er) can be seen clearly in the Electron Paramagnetic Resonance (EPR) spectrum. We show that the catalytic interfacial oxidation of the Si/Y_2O_3 interface, the diffusion of silicon into the oxide layer, and possible diffusion/contamination effects from surfaces are key material phenomena that need to be controlled and demonstrate how a buffer layer approach can mitigate these effects. No correlation between the Er^{3+} photoluminescence linewidths and the crystal quality as determined by X-ray

rocking curves was observed, indicating that structural distortions due to mosaicity and dislocations in the film may not play a significant role for quantum device development in such heterostructures. On the other hand, we observe a clear inverse correlation between PL linewidth and film thickness, lending further support to the potential role of the proximity of surfaces and interfaces. Finally, we show that alloying this system (Y_2O_3) with high quantity of lanthanum, which leads to a closer lattice matching condition[32], also results in broadening of the PL linewidth.

2.3 METHODS

2.3.1 Growth of epitaxial thin films

Epitaxial growths of Y_2O_3 (a = 10.60 Å, space group $Pm\bar{3}m$) thin films were performed on Si (111) substrates in a Riber oxide MBE system with a background pressure of ~10^{-10} torr. Substrates were prepared using a piranha clean followed by a dilute hydrofluoric acid (HF) dip. Epitaxial growth was initiated on 7×7 reconstructed Si (111) surfaces. A range of substrate temperatures between 600°C to 920°C was explored for growth. Ultra-high purity yttrium and erbium were evaporated using high-temperature effusion cells and an RF plasma source was used for oxygen (325 W, 2.8 sccm) corresponding to a pressure of ~2×10^{-5} torr in the growth chamber. Er concentrations between 5 ppm – 200 ppm were used for different samples by varying the Er cell temperature (between 700 °C and 900 °C). Er concentration was estimated using an Er_2O_3 film grown with Er cell temperature of 1200 °C and extrapolating the vapor pressure[36] to lower cell temperatures. The epitaxial growth was monitored in situ with reflection high-energy electron diffraction (RHEED).

2.3.2 Film characterization

Ex situ structural characterization was performed using a high-resolution X-ray diffractometer (Bruker D8 Discover). Optical characterization was realized in a confocal microscopy setup. Off-

resonant optical spectra were obtained following excitation with a 976 nm laser and the emission detected using a nitrogen-cooled InGaAs camera. Resonant optical spectra for the transition at ~ 1535 nm were realized using a tunable C-band laser (ID photonics CoBrite DX1) with the photoluminescence (PL) detected using a single nanowire single photon detector (SNSPD, Quantum Opus). In this case, the excitation and the PL signal were temporally isolated from each other using a combination of optical switches and acousto-optic modulators. The samples were mounted on a copper cold-finger in a closed-cycle cryostat (Montana Instruments).

X-band EPR was conducted using a Bruker Elexsys E500 system equipped with a variable-temperature cryostat (Oxford). The measurements were performed in a flow cryostat at 4.2 K. The *g*-factors were calibrated for homogeneity and accuracy by comparison to the Mn^{2+} standard in a SrO matrix (g = 2.0012 + 0.0002)[37] and by using coal samples with g = 2.00285 ±0.00005[38], respectively.

High-resolution transmission electron microscopy (HRTEM) was carried out using the Argonne Chromatic Aberration-corrected TEM (ACAT, FEI Titan 80-300ST TEM/STEM) with a field-emission gun and an image corrector to correct both spherical and chromatic aberrations, enabling information limit better than 0.8 Å at an accelerating voltage of 200 kV. High-angle annular dark-field imaging and energy-dispersive X-ray spectroscopy mapping were carried out using a Talos F200X S/TEM (operating at accelerating voltage of 200 kV) equipped with an X-FEG gun and a Super X-EDS system.

2.4 RESULTS AND DISCUSSION

2.4.1 Film Structure

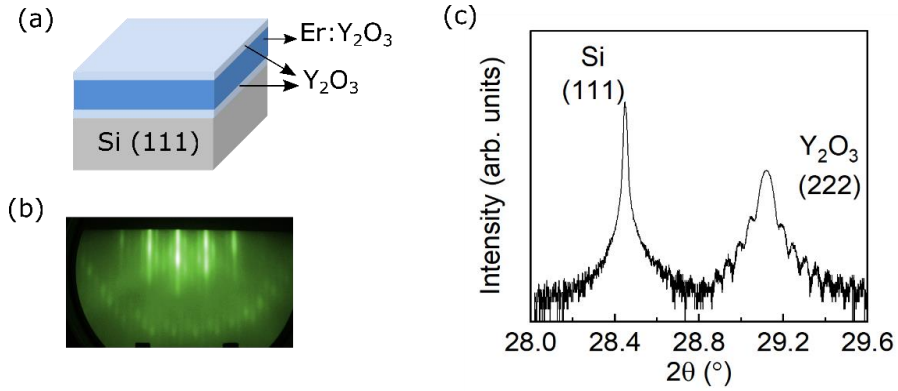

Figure 13 (a) Schematic of the film for which the data is shown, (b) shows the streaky RHEED pattern following the end of growth, indicating smooth and crystalline film. (c) XRD pattern showing the substrate Si (111) and film Y_2O_3 (222) peaks.

Figure 13(a) shows wide-angle (2θ-ω) X-ray diffraction pattern for a 180 nm film (~140 nm Er:Y_2O_3 with 10 ppm Er with a top cap and bottom buffer each of ~20nm undoped Y_2O_3) grown on Si (111) substrate at 850 °C showing Y_2O_3(222)//Si(111) epitaxial relationship. The presence of finite-size thickness (Pendellösung) fringes and streaky RHEED pattern (figure 13(b)) suggest smooth and crystalline film.

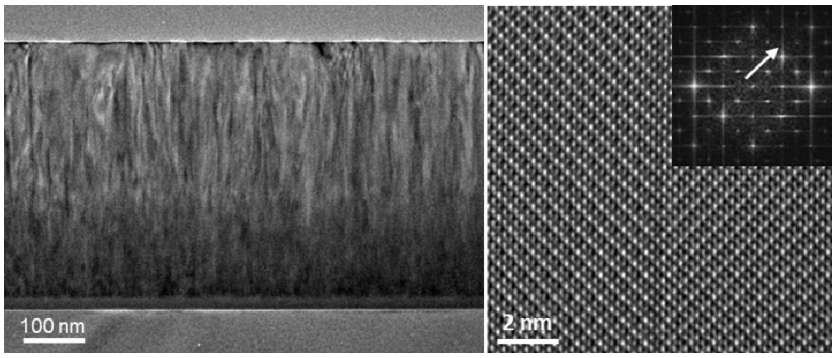

Figure 14 (a) Cross-sectional TEM of a 460 nm film grown at 920 °C (growth time = 80 min). The interfacial layer is visible. (b) A high-resolution TEM image showing Y2O3 film with a coincidence boundary. The inset shows diffraction pattern (arrow points in the 400 direction) confirming the bixbyite structure.

The crystalline and epitaxial nature of film growth was further studied using transmission electron microscopy (TEM). Figure 14(a) shows a cross-section transmission electron micrograph of the 460 nm Y_2O_3 film grown on Si (111) along with a high-resolution TEM image and a selected area electron diffraction (inset) of the film consistent with the bixbyite structure of Y_2O_3. In the bixbyite structure of Y_2O_3, there are 32 cation (Y^{3+}) site out of which 8 are centrosymmetric sites (C_{3i} symmetry with a 3-fold axis) and 24 non-centrosymmetric sites (C_2 symmetry with a 2-fold axis)[39]. As we show later, the Er^{3+} ions substitute for Y^{3+} at both of these sites. The high-resolution TEM image of the film/substrate interface and the energy dispersive spectroscopy (figure 15), indicates a double amorphous layer caused by Si oxidation at the Si interface– SiO_x near the Si surface which transitions to a phase consisting of Y, Si, and O due to Si diffusion as we move towards the Y_2O_3 film. This is due to the catalytic behavior of rare−earth oxide overlayers that results in silicon oxidation[40]. The interfacial oxidation occurs after epitaxial growth of Y_2O_3 via the diffusion of reactive oxygen through the film either during growth or ex-situ. This oxidation can be minimized by reducing the post-growth exposure to oxygen[41].

2.4.2 Engineering the film-interfaces

We investigated the effect of growth time and temperature on the presence of interfacial oxides and found that the thickness of the amorphous oxide interface increases with increase in growth time and substrate temperature. Figures 15(a) to 15(d) show the cross-sectional TEM image and 3(e) and 3(f) show the EDS line scans across the interface for two samples grown at 920°C and 790°C for 80- and 60-minutes long growths respectively. As seen in the scan, the interfacial oxidation leads to the formation of a silicon diffusion tail into the Y_2O_3 layer. The width of silicon contaminated zone in Y_2O_3 reduces with decrease in growth temperature from 920 °C to 790 °C.

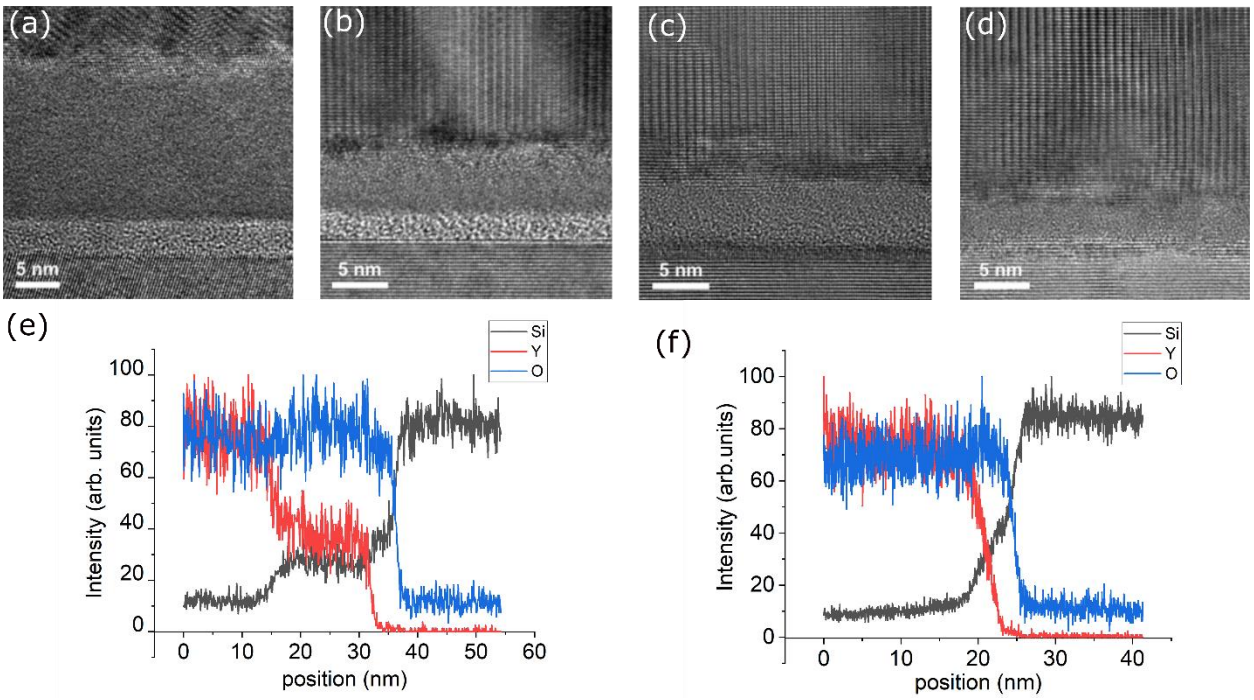

Figure 15 Cross-sectional TEM showing the interface for four different conditions of temperature (T) and time (t). Thickness of amorphous layer seen between crystalline Y2O3 and SiO2 can be directly estimated from the TEM (a) 24 nm for T = 920 °C, t = 80 min (b) 8 nm for T = 850 °C, t = 80 min (c) 5 nm for T = 790 °C, t = 60 min (d) 5 nm for T = 790 °C, t = 180 min. The EDS of the interface for (a) and (d) is given in figure (e) and (f) respectively.

In order to further probe the effect of possible silicon diffusion in the film and to examine the role of surface defects on the optical properties of Er^{3+}, we studied the photoluminescence for three samples with different structures – (i) 400 nm Er:Y_2O_3/Si, (ii) 400 nm Er:Y_2O_3/100 nm Y_2O_3/Si, and (iii) 200 nm Y_2O_3/400 nm Er:Y_2O_3/100 nm Y_2O_3/Si. Er concentration in these films were kept constant at ~ 50 ppm level. The inhomogeneous linewidth (Γ_{inh}) measured from the resonant PL for the first sample was 37.4 GHz (figure 16(d)). Insertion of a 100 nm undoped buffer layer decreased the linewidth to 24.0 GHz (figure 16(e)). This decrease in PL linewidth is attributed to an increased separation between the active Er^{3+} ions from the film/substrate interface. Further decrease in the PL linewidth was observed when the Er^{3+} ions are away from top interface, condition shown in 5(f). The inhomogeneous linewidth for this sample was found to be 19.6 GHz.

This *sandwiching* of the optically active Er^{3+}:Y_2O_3 layer between undoped Y_2O_3 helped reduce the inhomogeneous linewidth by about 50%, suggesting that both interfaces contribute to the broadening seen here.

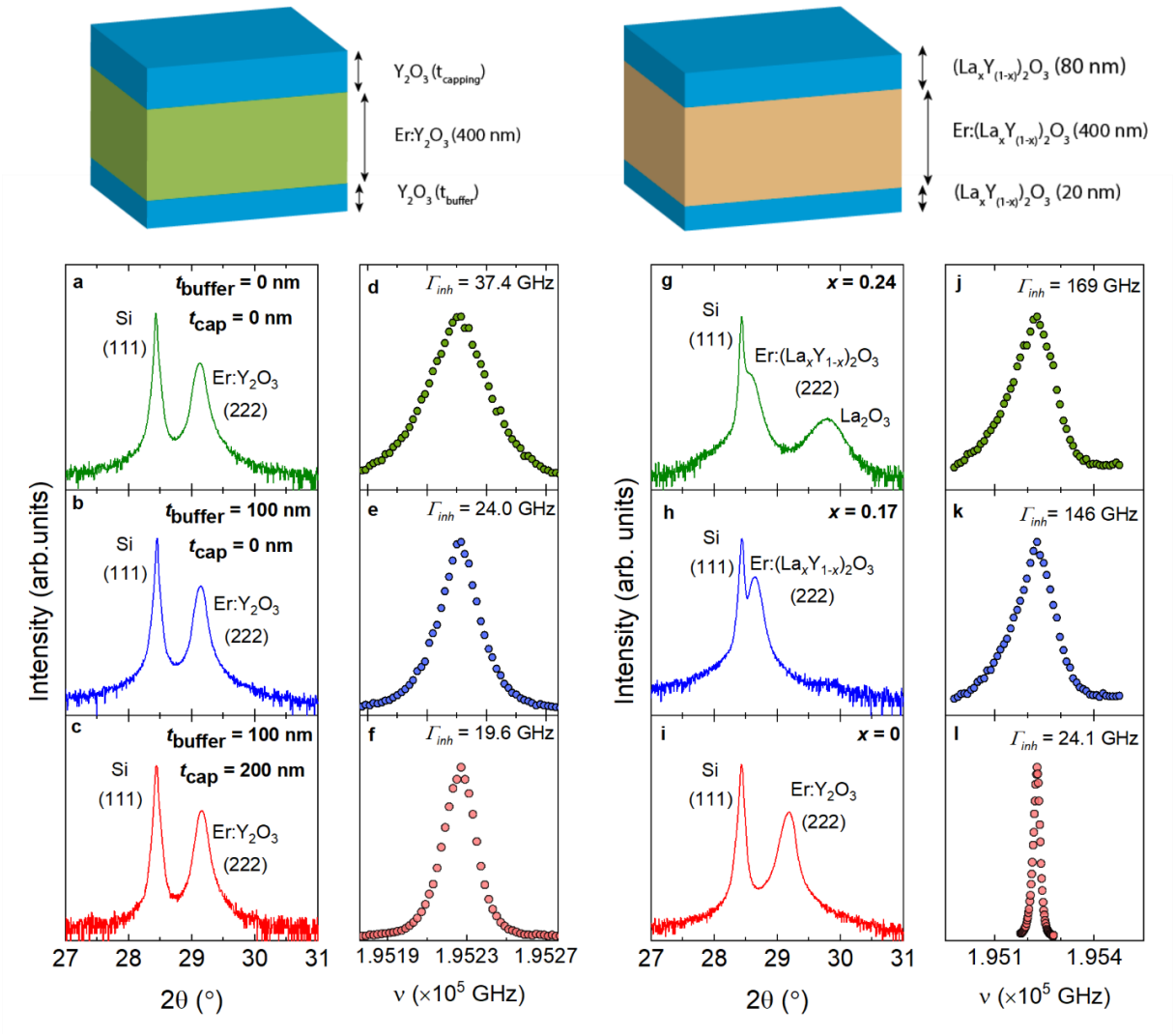

Figure 16 The schematic at the top left represents the structure (Y2O3)/(Er:Y2O3)/(Y2O3) used to probe the effect of the interface. (a-c) The XRD curve for the three films suggest similar crystal quality, (d) The baseline linewidth with no cap or buffer layer gives a Γinh of 37.4 GHz. (e) The addition of a bottom undoped layer improves this to 24.0 GHz. Further adding a top undoped layer improves the linewidth to 19.6 GHz (f) giving an improvement of almost 50% over the baseline. On the top right the schematic represents the structure (20 nm Y_2O_3)/(400 nm Er:$(La_xY_{(1-x)})_2O_3$)/(80 nm Y_2O_3) used to study the effect of the La alloying of Y_2O_3. The improvement in lattice match is clearly indicated by the shift in film XRD peak to Si (g-i). However, the inhomogeneous optical linewidth also broadens as more La is added (j-l).

Due to a large lattice mismatch (2.4% tensile), relaxed Y_2O_3 will contain dislocations that relieve the elastic strain. It has been shown earlier that alloying Y_2O_3 with La can reduce the lattice mismatch with silicon[32]. To explore the possibility of using a lattice-matched host material for Er^{3+}, a 80 nm $(La_xY_{1-x})_2O_3$/400 nm Er:$(La_xY_{1-x})_2O_3$/ 20 nm $(La_xY_{1-x})_2O_3$ /Si (111) film was grown with x = 0, 0.17, and 0.24. Er concentration in these films were kept constant at ~ 200 ppm level. Figure 16(g)-(i) shows wide-angle x-ray diffraction pattern for the three sample with x = 0.17 corresponding to the lattice−matched condition. A separation of ~ 720 arcsec between the Y_2O_3 (222) and Si (111) Bragg peak in the 2θ−ω scan for the lattice-matched film resulted from the difference in the thermal expansion coefficient between Y_2O_3 and Si ($\Delta\alpha = 4\times10^{-6}$ K^{-1}). However, the inhomogeneous linewidth for the lattice-matched film (x = 0.17) was found to be 7× larger than the unalloyed film (figure 16(j)-(l)). This broadening is attributed to the presence of random substitutional disorder in the film due to La substituting at the Y site similar to the results reported for Sc alloyed Er:Y_2O_3[42] and Eu:Y_2O_3[43]. Increasing the amount of La (x = 0.24) further increases the inhomogeneous linewidth due to enhanced disorder as well as phase segregation of hexagonal La_2O_3 as evidenced by an additional diffraction peak in the corresponding 2θ−ω scan.

2.4.3 Spectroscopic Characterization

The presence of Er^{3+} and its incorporation into the crystal structure was confirmed using EPR measurements. Figure 17(b) shows the EPR spectra for a 650 nm Er:Y_2O_3 film at 4.2 K (Er concentration ~ 10 ppm). Naturally occurring Er has multiple isotopes – ^{166}Er, ^{167}Er, ^{168}Er, ^{170}Er – which constitute 33.50%, 22.87%, 26.98%, 14.91% of naturally occurring erbium, respectively. ^{167}Er is the only isotope with non-zero nuclear spin (spin = 7/2). The contribution from ^{167}Er is seen as eight smaller peaks in figure 17(b) distributed around the main peak at 548.24 ± 0.2 G that

comes from the zero nuclear spin isotopes. A schematic is shown in figure 17(a). The relative intensities of these peaks are indicative of the abundance of different isotopes. The effective *g*-factor calculated for the central peak from the data shown in figure 17(b) is 12.2 – this is a composite of the contributions coming from the Er^{3+} ion sitting at both the C_2 and C_{3i} sites (C_2 and C_{3i} sites are described earlier in the text and in ref [25]). The peak position was found to have a dependence on the angle between the magnetic field and the (111) crystallographic plane[44].

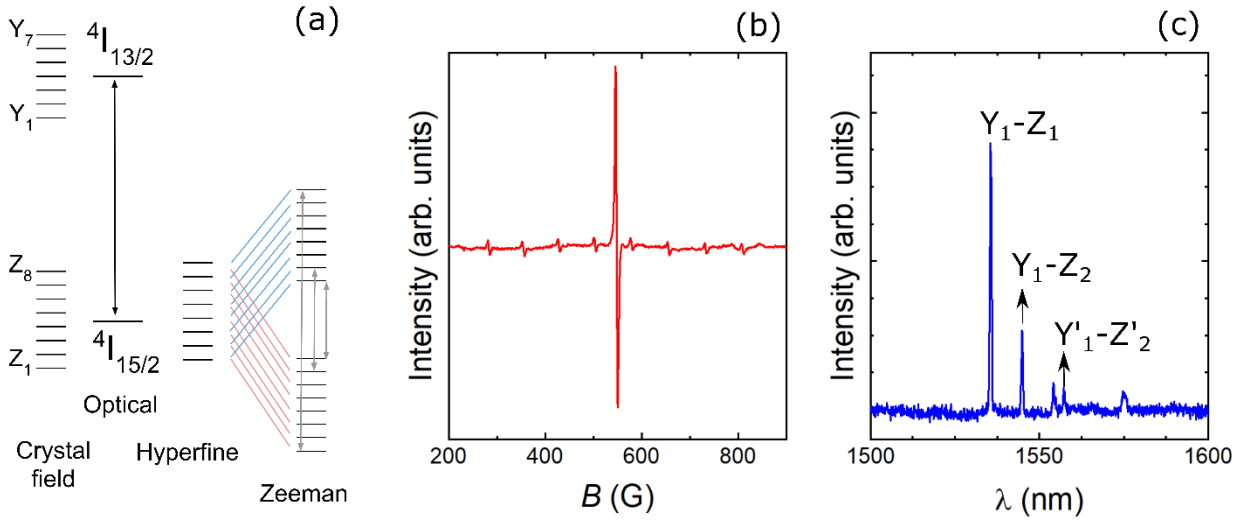

Figure 17 (a) A schematic of the energy levels of interest in the Er3+ - Stark levels from the crystal field effect (emission spectra) and the Zeeman splitting of the hyperfine levels which is seen in EPR. . (b) EPR spectra shows a large central peak from the zero nuclear spin isotopes of Er. Eight smaller peaks from the hyperfine transitions contributed by 167Er are also seen. (c) Photoluminescence spectra from Er:Y_2O_3 films. Contribution from C_2 and C_{3i} sites are identified by the energies reported in literature. This confirms the substitution of Er^{3+} for Y^{3+} in the bixbyite structure.

The crystal field effect breaks the spherical symmetry of the free ion and this results in the splitting of the ground state ($^4I_{15/2}$) into 8 Stark levels and the first excited state ($^4I_{13/2}$) into 7 Stark levels – where the number of levels is dictated by the total angular momentum quantum number[28]. These energy levels of these Stark levels are represented as Z_i (Z_1 to Z_8) for the split $^4I_{15/2}$ levels and Y_i (Y_1 to Y_8) for the split $^4I_{13/2}$ levels as shown in figure 17(a), and similarly as Y_i' and Z_i' for the C_{3i}

sites. Figure 17(c) shows the PL data collected at 10 K in the wavelength range 1500 nm – 1600 nm. Emission peaks in this range is due to transitions between the Stark level manifold of the first excited state ($^4I_{13/2}$) and the ground state ($^4I_{15/2}$). Using data reported in literature[45] the PL peaks at 1535.6±0.01 nm, 1544.9±0.04 nm, 1554.2±0.1 and 1575.1±0.3 nm can be identified as the $Y_1 \rightarrow Z_1$, $Y_1 \rightarrow Z_2$, $Y_1 \rightarrow Z_3$ and $Y_1 \rightarrow Z_5$ transition at the C_2 cite. The peak at 1557.3±0.3 nm is identified as likely coming from the $Y'_1 \rightarrow Z'_2$ transition at the C_{3i} site. This confirms that Er^{3+} is substituting for Y^{3+} in the crystal lattice.

Figure 18(a) shows X-ray rocking curve full width at half maxima ($\Delta\omega$) (indicative of crystalline quality) and the film thickness as a function of the photoluminescence linewidth, Γ_{inh}. The data shows no clear correlation between the crystalline quality of the film and Γ_{inh}. This suggests that the optical properties of Er^{3+} in the Y_2O_3 host might not be limited by variations in lattice strain and the presence of defects such as dislocations in the host. This trend is unlike what is typically observed in band edge related emission in semiconductors, where poor crystal quality results in poor band edge photoluminescence. On the other hand, the plot of films thickness versus Γ_{inh} shows a strong inverse trend—thicker layers result in narrower photoluminescence linewidths. We attribute this to isolation of an increasing proportion of the active Er^{3+} from interfacial and surface effects due to increase in the film thickness. Our best PL linewidth for C_2 site emission was found to be 7.9 GHz at 4 K and 5.1 GHz at 7 mK as shown in figure 18(b). The optical excitation decay rate measured for this emission was found to be 8.1 ms (shown in figure 18(c)) which is comparable to the reported value of 8.5 ms in bulk crystal[46].

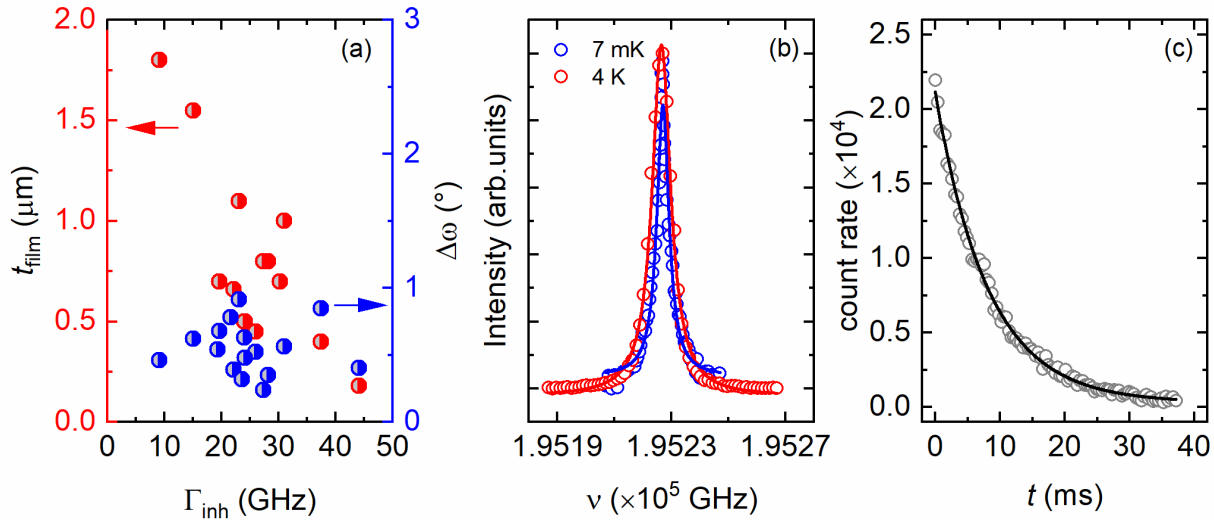

Figure 18 (a) A strong linear correlation is seen between PL linewidth and the film thickness (red), a comparison of the two metrics of disorder in the crystal quality, optical inhomogeneous linewidth (y-axis) and rocking curve FWHM (x-axis) however, shows no correlation (blue). (b) The narrowest linewidth obtained in our samples is 7.9 GHz at 4K (red) and 5.1 GHz in the same sample at 7mK (blue) (c) Optical excitation decay rate at the C_2 site was measured as 8.1 ms.

2.5 CONCLUSION

The rare earth ion, Er^{+3} offers attractive properties suitable for use as a quantum memory: a spin-optical interface, narrow photoluminescence linewidth, low spectral diffusion, and an emission wavelength in the telecom band. This, paired with Y_2O_3's low absorption in that wavelength range and epitaxial compatibility with Si makes Er:Y_2O_3 thin films on Si a promising materials platform for quantum technologies. We have successfully demonstrated the growth of Er:Y_2O_3 epitaxial thin films on Si(111) and, using spectroscopic techniques demonstrated that the erbium substitutes for yttrium in the bixbyite structure at both the C_2 and C_{3i} sites where the optical decay lifetime obtained for the C_2 sites is comparable to that of bulk crystals. We have further carried out a detailed microstructural and optical study of these epitaxial films. We have shown how, bottom and top spacer (or buffer) layers are needed in the stack in order to optimize the Er photoluminescence linewidths. We show, importantly, that unlike band edge related

photoluminescence in semiconductors the photoluminescence of the Er^{3+} emission (Γ_{inh}) is unaffected by crystal quality as determined by X-ray rocking curve linewidths. However, we show that the photoluminescence linewidths are directly correlated to film thickness indicating surface and interface effects and potential impurity effects related to surfaces/interfaces. Lattice engineering using La leads to improvement in the mismatch with silicon but degrades the Γ_{inh} significantly. Finally, we show that by optimizing the epitaxial growth conditions, we can obtain ultra-narrow linewidths of 5.1 GHz indicative of high quality Er^{3+} incorporation in a largely non-interacting host.

2.6 ACKNOWLEDGEMENTS

This work was supported in part by the Center for Novel Pathways to Quantum Coherence in Materials, an Energy Frontier Research Center funded by the U.S. Department of Energy, Office of Science, Basic Energy Sciences under Award No. DE-AC02-05CH11231. A.P., T.R., and T.Z. acknowledges support from the Argonne National Laboratory's Laboratory Directed Research and Development (LDRD) program. Use of the Center for Nanoscale Materials, an Office of Science user facility, was supported by the U.S. Department of Energy, Office of Science, Office of Basic Energy Sciences, under Contract No. DE-AC02-06CH11357. S.G. acknowledges the Vannevar Bush Fellowship under the program sponsored by the Office of the Undersecretary of Defense for Research and Engineering (OUSD (R&E)) and The Office of Naval Research as the executive manager for the grant.

2.7 SUPPLEMENTAL MATERIALS

Epitaxial Er-doped Y_2O_3 on Silicon for Quantum Coherent Devices

Manish K. Singh[1], Abhinav Prakash[1, 2], Gary Wolfowicz[1, 2], Jianguo Wen[2], Yizhong Huang[1], Tijana Rajh[2, †], David D. Awschalom[1, 2], Tian Zhong[1, †], Supratik Guha[1, 2, †]

[1]Pritzker School of Molecular Engineering, University of Chicago, Chicago, IL, USA, 60637

[2]Argonne National Laboratory, Lemont, IL, USA, 60439

[†]Corresponding authors: Supratik Guha (guha@uchicago.edu), Tian Zhong (tzh@uchicago.edu) and Tijana Rajh (rajh@anl.gov)

Figure 19(a) shows the linewidth (ΔB) of 2.25±0.02 gauss that we calculate using a Lorentzian fit. Angular dependence of the EPR spectrum was studied by rotating the sample using a goniometer such that the angle between the (111) crystallographic plane and the magnetic field, B can be varied in one plane. Figure 19(b) shows EPR scans of our sample demonstrating angular dependence of the derivative peak (ΔB and peak center). This dependence gives further evidence that the Er substitutes for Y in the crystal lattice. All EPR data presented in this paper is from the same sample.

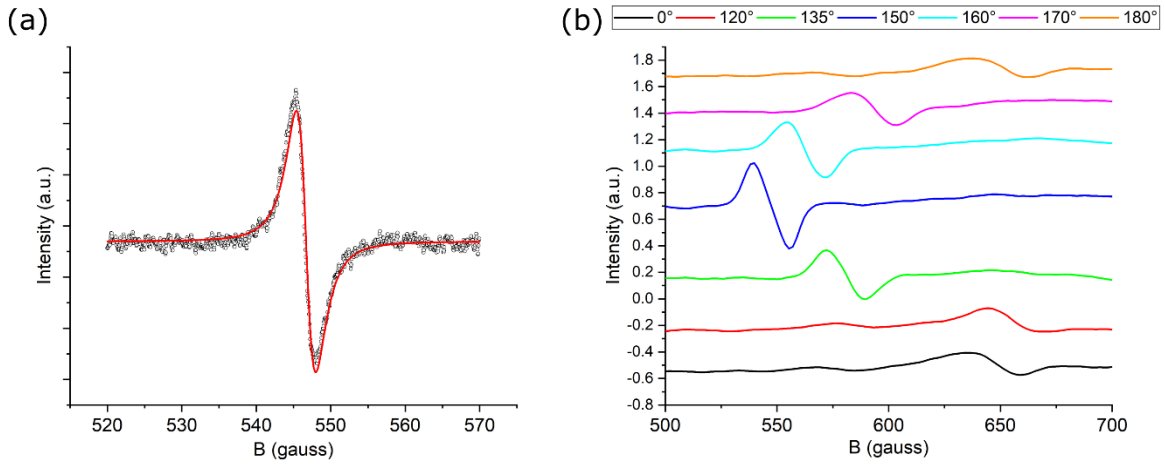

Figure 19 (a) Derivative peak obtained from EPR gives an effective g=12.2 and shows a linewidth (ΔH) of 2.25±0.02 gauss using a Lorentzian fit. (b) The peak shift and broadening with rotation of the sample with respect to the magnetic field suggests Er substitution in the bixbyite crystal for Y.

Atomic force microscopy (AFM) using Veeco Multimode 8 Scanning Probe Microscopy was used for surface roughness characterization, an important factor for optical waveguides. A root mean square (RMS) roughness of 0.8 nm was for a 50 nm on Si (111) (figure 20)

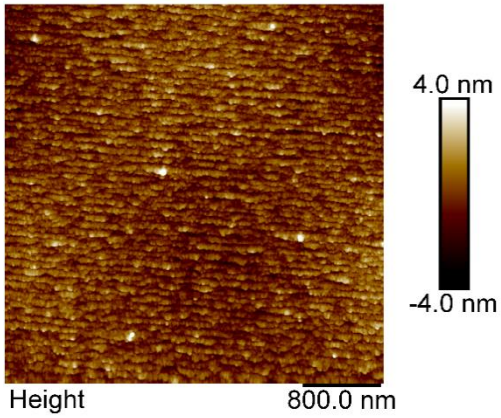

Figure 20 AFM image for Si 111 sample (50nm film thickness) showing a roughness of 0.8nm (RMS)

3 DEVELOPMENT OF A SCALABLE QUANTUM MEMORY PLATFORM—ER DOPED TiO_2 THIN FILMS ON SILICON

Manish Kumar Singh[1], Gary Wolfowicz[2], Jianguo Wen[2], Sean Sullivan[2], Abhinav Prakash[2], Alan Dibos[2], David Awschalom[1,2], F. Joseph Heremans[1,2], Supratik Guha[1,2]*

[1]Pritzker School of Molecular Engineering, University of Chicago, Chicago, IL, USA 60637

[2]Argonne National Laboratory, Lemont, IL, USA, 60439

*Corresponding author: Supratik Guha (guha@uchicago.edu)

A version of this work is submitted to the journal AIP materials for review and publication

3.1 ABSTRACT

Rare-earth ions (REI) have emerged as a strong candidate for solid-state qubits, particularly as a quantum memory. Their 4f-4f transitions are shielded by the fully filled 5s and 5p orbitals, giving them some degree of protection from external electric fields. Embedded in an oxide host, REI could enable a qubit platform that has significant memory capabilities (>1 s for erbium). Furthermore, a silicon-compatible thin film form factor will enable us to use semiconductor fabrication techniques to achieve massive scalability and build a functional quantum network. Towards this goal, we present our study of erbium-doped TiO_2 thin films. We have studied growth on lattice-matched (r-sapphire, $SrTiO_3$) and on Si (100) (no lattice match) substrates and found that the inhomogeneous linewidth is better for the polycrystalline films on silicon (compared to single-crystal thin films). Further experiments to investigate the effect of film/substrate and film/air interface were performed, where we discovered that the inhomogeneous linewidth and spectral diffusion can be improved significantly by adding a bottom buffer and a top capping layer of undoped TiO_2. We also established that in the regime investigated; the inhomogeneous linewidth does not appear to be limited by erbium concentration or substrate temperature.

3.2 INTRODUCTION

Quantum memories are a key part of proposed quantum communication networks capable of establishing entanglement-based links over long distances[1,5,16,47–49]. Solid-state rare-earth memories are of interest because of (1) the form factor offers ease of handling and potential of massive scalability and (2) rare earth ions have been shown to be great candidates for quantum memory. A variety of oxides have been studied as potential hosts for these rare earth ion-based qubits[46,50] and both implanted bulk crystals and thin films form factor is being actively explored to understand the material system. Embedding these RE atom qubits in thin-film wide band-gap

solid state hosts have emerged as a promising platform [48,51,52], where the primary advantage comes from these systems being inherently scalable. Towards this end multiple studies in the recent years have started exploring the potential for using thin films hosts which can take advantage of established semiconductor industry processes. One important driving force in this area has been key demonstrations of interaction with single atoms using nanophotonic structures for both Purcell enhanced increase in emission rates as well as optical access of the active rare earth ion[53,54].

Motivated by this, we investigated and present here the growth and characterization of Er-doped polycrystalline TiO_2 thin films on silicon substrates as a promising scalable platform. The choice of Er^{3+} is motivated by the fact it has its first optical excited state emission in the telecom C-band (1530 - 1565 nm). This means that photons from Er^{3+} qubits can be directly transmitted over existing long-distance optical fibers without the need for wavelength conversion. In addition, this telecom emission is an intra-4f transition with narrow linewidth, as the 4f shells are shielded by the 5s and 5p levels which provide protection from the local environment. The choice of TiO_2 thin films is motivated by its compatibility with Si process technology for future on-chip integration, which has been explored in the past as a high dielectric constant gate oxide for silicon MOSFETs [55,56]. Furthermore, TiO_2 has a wide band gap (3.2 eV), an inert near-nuclear spin free (87%) host environment for Er, and TiO_2 is relatively free of trace rare earth impurities, unlike many rare-earth oxides. Additionally, recent investigations of Er in bulk TiO_2 in the context of quantum information science (QIS) have revealed promising optical properties of Er emission (linewidths, lifetime etc.)[57].

In this study we explore Er doped TiO_2 thin films grown on silicon and other substrates. We report insights in the host material's effect on the optical properties of Er dopants. First, the polycrystalline TiO_2 films on silicon is shown to have better inhomogeneous linewidth compared

to the single crystal films on lattice matched substrates hinting at other factors influencing these properties. Second, we show that the phase (rutile, anatase) can be controlled using growth temperature when growing on silicon. Third we show that using undoped TiO_2 bottom buffer and top capping layers we can engineer the inhomogeneous linewidth. This is also shown to depend on the erbium density, albeit at concentrations higher than our baseline, and on the temperature of the sample. Finally, we show that the spectral diffusion linewidth can also be engineered using concentration and film stack.

3.3 METHODS

3.3.1 Growth

The films were deposited by molecular beam epitaxy (MBE) using a Riber oxide MBE system. Titanium tetraisopropoxide (TTIP) from Sigma-Aldrich with a purity of 99.999% (trace metal basis) was used as the titanium precursor. The TTIP flux was precisely controlled using a computer-controlled needle valve: details of TTIP based MBE of TiO_2 has been described in detail by Jalan et al.[58]. The erbium doping in these films is in the range 10-1000 ppm and was carried out by the evaporation of erbium (5N, rare-earth basis, obtained from Ames Lab) using a high temperature effusion cell whose temperature was varied in the range (800-1200). Films were grown over a range of substrate temperatures (480-850 °C). TiO_2 growth rates were held at ~ 60 nm/hr. Molecular oxygen flow was kept at 0.55 sccm. The substrates used were, r-plane sapphire, Al_2O_3 (012), $SrTiO_3$ (STO) (100) and Si (100). The STO and sapphire substrates each had a 350 nm thick Ta layer on the backside for improved radiative heat transfer between the heater and substrate. Prior to growth the oxide substrates were cleaned in-situ using 20 min of O_2 plasma. For the silicon substrate, we performed an RCA clean followed by an HF dip (for native oxide

removal) and the cleanliness of the substrate was signaled by the 2x1 surface reconstruction. After growth, the films were cooled to 200 °C in a partial oxygen environment via a 0.55 sccm O_2 flow. The default concentration for the films discussed is estimated at 36 ppm (unless otherwise specified). The concentration was estimated using data from an Er_2O_3 film grown at 1200 °C and extrapolating the vapor pressure[59] to the lower concentrations.

3.3.2 Characterization

The growth and substrate reconstruction were monitored in-situ using reflection high-energy electron diffraction (RHEED). Ex-situ film characterization was performed using X-ray diffraction (XRD, Bruker D8 discover), Atomic Force Microscopy (AFM, Bruker Dimension Icon) high resolution transmission electron microscopy (HRTEM), and optical spectroscopy. TEM characterization used the Argonne chromatic aberration-corrected TEM (ACAT), a FEI Titan 80-300ST with a spherical and chromatic aberration imaging corrector, and an FEI Talos 200X scanning transmission electron microscope.

Optical spectroscopy measurements were performed in a custom-built cryogenic confocal microscope using a closed cycle cryostat (Montana Instruments) with a base temperature of 3.5K. All spectroscopic measurements are performed at this temperature unless otherwise noted. Laser light is focused on the sample to a diffraction-limited spot using an external 50x objective (OptoSigma, NA 0.67). Off-resonant measurements were performed using a 905 nm excitation laser (QPhotonics QFLD-905-200S). Broadband Er^{3+} photoluminescence was collected with a fiber-coupled spectrometer and a liquid nitrogen-cooled InGaAs camera (IsoPlane-320 and PyLoN-IR, Teledyne Princeton Instruments) using a 300 g/mm diffraction grating blazed for 1.2 μm light, achieving a spectral resolution of approximately 0.3 nm. On resonant, photoluminescence excitation (PLE) spectroscopy is performed using a tunable C-band laser

(PurePhotonics). Light is collected (emitted) from (into) free-space from a single collimator into a polarization maintaining fiber. The fiber is connected to a bidirectional 2x1 acousto-optic modulator switch (Brimrose) which switches between a collection and an excitation path. During excitation, the switch routes laser light onto the sample, while during collection the switch routes the photoluminescence to a fiber-coupled superconducting nanowire single photon detector (SNSPD, Quantum Opus). Two additional acousto-optic modulators (AA-Optoelectronic) on the excitation path fully attenuate any cross-talk from the excitation laser to well below the SNSPD dark noise (< 100 counts/s). Spectra are obtained by sweeping the wavelength of the tunable laser and exciting for a pulse duration between 0.1 and 1 ms. The photoluminescence is collected after a buffer delay of 100 μs after the excitation pulse and is measured for a duration between 1 and 15 ms. Spectral diffusion measurements are realized using an intensity electro-optic modulator (10 GHz, Thorlabs), biased at the quadratic point, to create the probe sidebands. The sideband frequency is set and swept by a driving external microwave signal generator.

3.4 FILM STRUCTURE

TiO_2 crystallizes into two main phases, anatase ($I4_1/amd$, a = 3.7845 Å, c = 9.5143 Å; Z = 4) and rutile ($P4_2/mnm$ a = 4.5937 Å, c = 2.9587 Å; Z = 2). Of these, rutile has been grown epitaxially on r-plane sapphire (012)//TiO_2 (101), with a mismatch of 3.7% along $[010]_{TiO_2}$ and 6.04% along $[\bar{1}01]_{TiO_2}$[60]. Similarly, STO substrates have been used for stabilization of the anatase phase and STO (100)//anatase-TiO2 (001) (a mismatch of 3.1%[61]).

Our results for both TiO_2 phases grown on r-plane sapphire, STO (100) and Si (100) are summarized in Figure 21 which also shows the cross-sectional TEM used to study microstructures of these films (fig 21(a)-(h)). The streaky RHEED images (fig 21(m), (o)) shows that TiO_2 films

deposited sapphire and STO substrates are single crystal. Selected area electron diffraction (SAED) pattern in fig 21(i) further confirms that the film has a rutile structure with its crystallographic orientation relationship to sapphire substrate as follow: $[101]_R//[211]_S$, $(-101)_R//(10\text{-}2)_S$, $(020)_R//(1\text{-}20)_S$. The film/substrate interface shown in the HRTEM image (fig. 21(e)) is difficult to distinguish, likely indicating a rutile film epitaxially grown on the sapphire substrate without any intermediate layer. On the STO substrate, we see anatase films growing epitaxially (fig 21(c), (g), (k), (o)) with crystallographic orientation relationship: $[100]_A//[001]_S$, $[010]_A//[100]_S$, $[001]_A//[010]_S$.

Thin films grown on silicon substrates at 750 °C are polycrystalline with an average grain size of ~50 nm (fig 21(b)). HRTEM image of the interface shows the film/substrate interface is wavey (fig 21(f)) and an intermediate layer with an average thickness of 3-4 nm is observed between the film and substrate. Line profiles of X-ray energy dispersive spectroscopy (EDS) as shown in the supplementary information (SI) show the intermediate layer is a SiO_x layer, which is formed due to the reaction of oxygen in the TiO_2 film with the substrate. Although the film is polycrystalline, the integrated SEAD pattern from 25 areas along the film shows there is a certain degree of epitaxial relationship of rutile TiO_2 on Si as shown in the SI. This suggests that the intermediate layer SiO_x is formed following the growth of the film.

When the deposition temperature is lowered to 480 °C, the film grown on Si is found to be polycrystalline anatase with average columnar grain size of ~10 nm (fig 21(d)). HRTEM image of the interface shows the film/substrate interface is smooth and an intermediate layer with an average thickness less than 1 nm is observed between the film and substrate. Integrated SEAD patterns from 25 areas along the film shows there is certain degree of epitaxial relationship of anatase TiO_2 on Si as shown in the SI.

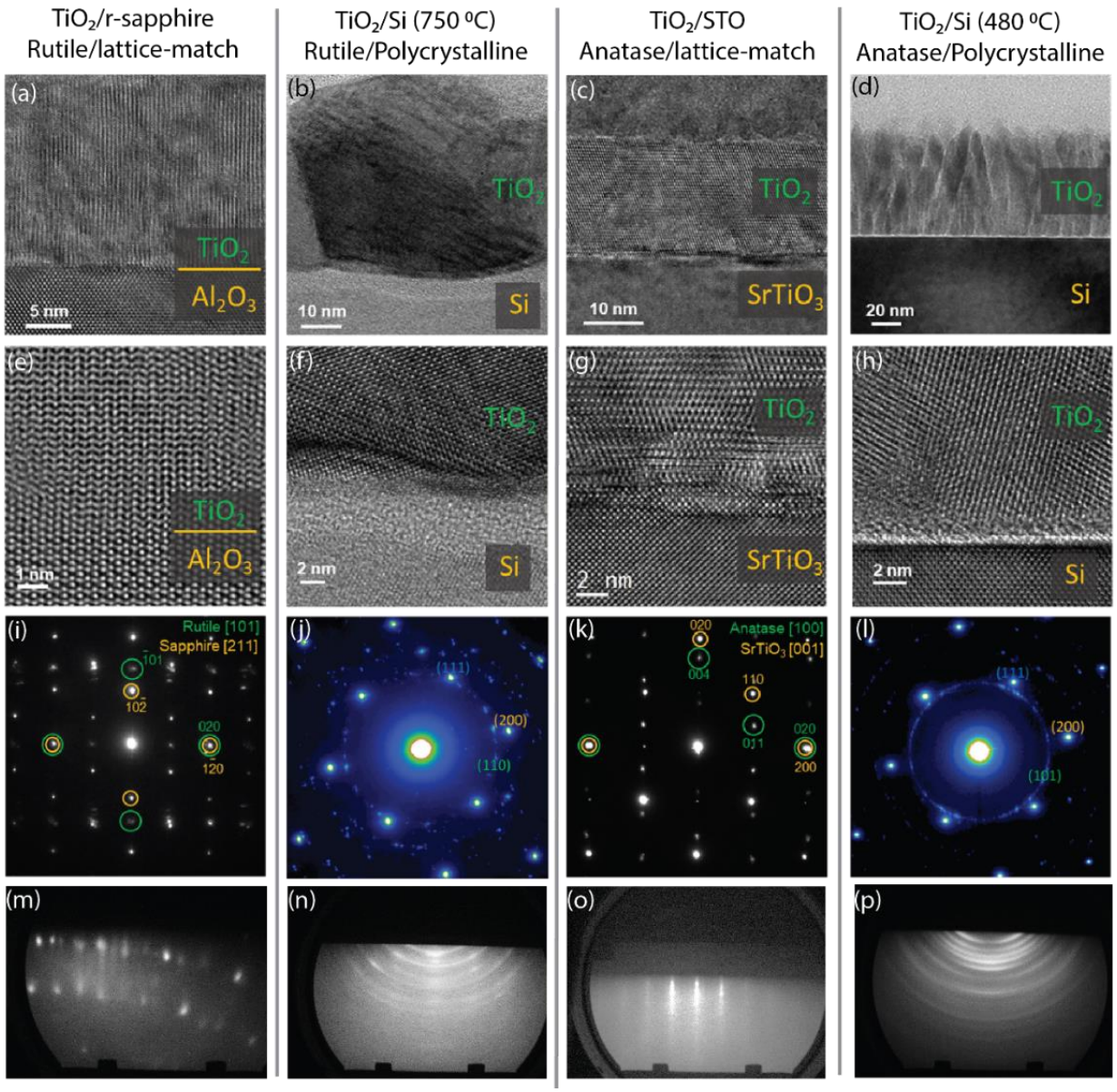

Figure 21. TEM, RHEED and XRD data for the TiO_2 films/substrates investigated is shown here – growth on STO and sapphire shows an epitaxial relationship and single crystal growth while growth on Si is polycrystalline. (a)-(d) TEM showing the films on the substrates (as labelled) (e)-(h) zoomed in image of the interface shows how the interface compares in the four cases, showing epitaxy (e & g) and showing an oxide interface (f & h). (i-l) Selected area electron diffraction (SAED) confirms the epitaxial relationship for sapphire (i) and STO (k). (m-p) Streaky RHEED pattern is indicative of single crystal growth (m & o) and rings observed in n & p are indicative of poly-crystalline growth.

3.4.1 Spectroscopic characterization

For single crystal rutile (on Sapphire) we get a prominent erbium emission peak around 1520 nm which is consistent with the data supporting erbium substituting for Ti in the TiO_2 unit cell[57] at low concentrations. For single crystal anatase (on STO) we get a prominent erbium emission peak around 1533 nm in line with what has been reported for erbium doped anatase in literature[62,63] and corresponds to the $^4I_{13/2} \rightarrow {}^4I_{15/2}$ transition. We find the same emission peaks for films grown on Silicon, polycrystalline rutile (high growth T) and anatase (low growth T). As discussed above, the intermediate growth temperatures show peaks corresponding to both phases. The intermediate growth temperature, where there is a mixed phase, then enables the interesting possibility for multiplexing qubits at two different wavelengths within the same volume. This can be particularly useful, for instance, in the case of quantum optical sensing—often two wavelength responses are evaluated for better accuracy.

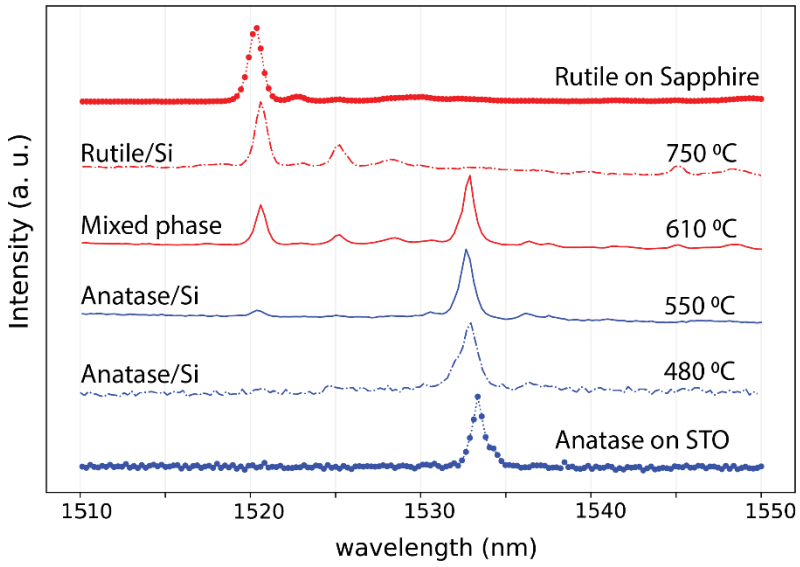

Figure 22. Photoluminescence (PL) spectra of Er:TiO_2 on silicon grown at different temperatures. Er^{3+} in rutile TiO_2 has an emission wavelength of ~1520 nm and in anatase of ~1533 nm. As the growth temperature is increased from 480 °C to 750 °C, the rutile peak intensity increases while the anatase peak decreases. Er:TiO_2 on sapphire and STO PL data is included for reference. Note that the offset is articficial, added for clarity.

It is important to note that the linewidths of the peaks in figure 22 are limited by the resolution of the spectrometer grating. Therefore, we also performed photoluminescence excitation spectroscopy using a tunable, narrow laser to measure the inhomogeneous linewidth (Γ_{inh}) of the peaks of interest. Γ_{inh} is an important metric for characterizing the non-uniformities (compared to traditional metrics like XRD) when it comes to quantum relevant properties[64,65]. A narrow linewidth is important as (1) it enables higher optical depth allowing us to access smaller ensembles in the material system at lower erbium concentration and (2) it allows optical pumping of spin levels[3,53,66], e.g., in the case of erbium it allows for simpler, faster initialization of quantum states.

In figure 23, we compare the optical inhomogeneous linewidth obtained using Lorentzian fit for the various TiO_2 films. For the single crystal films, we observed a linewidth of 108 GHz for rutile (on sapphire) with a 28 nm Er doped film. Compared to the value from Phenicie et al.[57], where they study erbium implanted in bulk TiO_2, this inhomogeneous linewidth is significantly broader (108 GHz Vs 0.46 GHz). However, it is important to note that this is a through doped TiO_2 that has not been optimized via layer engineering, described later, which could lead to lower linewidths. Single crystal TiO_2 film (10 nm undoped bottom buffer/10 nm doped layer/5 nm undoped cap) on STO (anatase) gave an inhomogeneous linewidth of 18.9 GHz. A surprising observation was that the polycrystalline samples (on Silicon) had narrower linewidths compared to the single crystal films – with 91 GHz for polycrystalline rutile (~15% improvement) and 11.1 GHz for polycrystalline anatase (~41% improvement).

The improvement going form single to polycrystalline can be partly attributed to the strain relaxation (see the section III.C) due to the absence of epitaxial constraints in the polycrystalline growth. However, the dissimilar amount of improvement in the two phases hints at other possible

reasons, potentially suggesting that the position of the erbium and the coordination number for the two phases in the TiO_2 lattice in the two phases may play a role[67], and is an interesting topic for further study. Here, we focus on polycrystalline anatase on silicon to study the effect of the interface, concentration, and sample temperature, as it offers the overall narrowest linewidth, C-band wavelength, and the technological advantages of integrating with silicon based platforms.

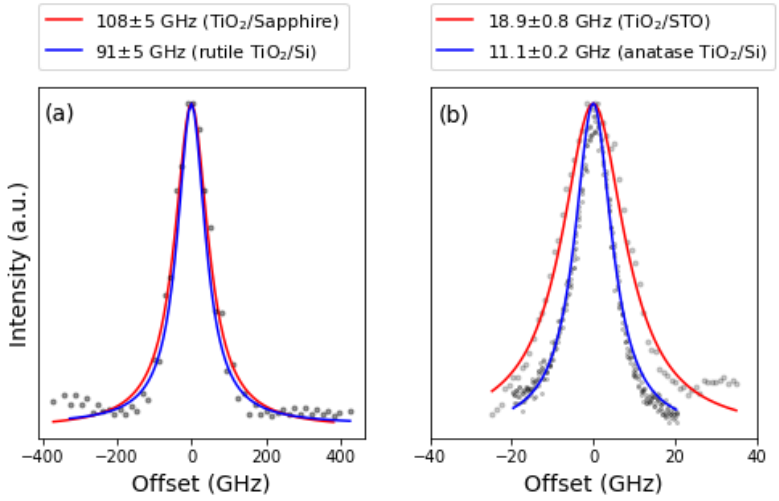

Figure 23. (a) The rutile phase in both single crystal and polycrystalline forms shows inhomogeneous linewidths >90GHz. (b) The anatase phase, by contrast, shows an inhomogeneous linewidth much smaller compared to that in the rutile phase, the polycrysailline anatase on Silicon demosntrates a narrower linewidth compared to single crystal anatse on STO (by ~ 41%)

3.4.2 Engineering thin film properties

In our earlier investigations of epitaxial Er:Y_2O_3 [64], we have showed that distance of the Er doped layer from the substrate-film interface had a significant effect on the inhomogeneous linewidth (Γ_{inh}) of the optical emission from the Er. To explore this effect in TiO_2, we carried out experiments using a film stack of undoped TiO_2 bottom buffer/Er:TiO_2/undoped top cap. The thickness of the undoped bottom buffer was varied between 10 to 60 nm while the doped and top cap layer thicknesses were kept constant at 10 nm and 5 nm respectively. The results, plotted in Figure 4, show a clear reduction in Γ_{inh} with the linewidth reducing from ~31 GHz (with no buffer

or capping) to ~5.2 GHz with a bottom undoped buffer of 60 nm and capping layer of 5 nm. This is similar to the trend observed earlier in the case of Er:Y_2O_3, indicating a broader underlying phenomenon. Comparison with the Y_2O_3 results also imply that the phenomena is independent of whether the films are epitaxial or polycrystalline. Additionally, it also platform independent, as this approach of adding a capping/buffer layer to the doped films has also been suggested by Harada et al.[68] for their Eu doped Y_2O_3 system.

Elastic strain or extended defect concentration variations in the host crystal can lead to changes in the emission wavelength due to variations in the local electric field interacting with the Er atoms embedded in the host. This could be one possibility. However, we have observed an insensitivity of PL linewidths relative to the X-ray linewidths in Er:Y_2O_3, and the observation (noted earlier in this paper) of narrower linewidths in polycrystalline TiO_2 films when compared to single crystal films makes unlikely that defect density variations or a systematic variation in elastic strain is responsible for this. A second, more likely possibility is the distribution of charge defects within the oxide/silicon heterostructure. Almost all wide band gap oxides that are strongly ionic, have a rich defect chemistry that arises from non-stoichiometry[69,70], leading to charged vacancies on the cationic or anionic sites and their complexes. The presence of non-uniform distributions of such charged defects in the vicinity of the Er can lead to PL broadening. In this case, the experimental results would indicate that the charge defects have a higher concentration near the substrate interface.

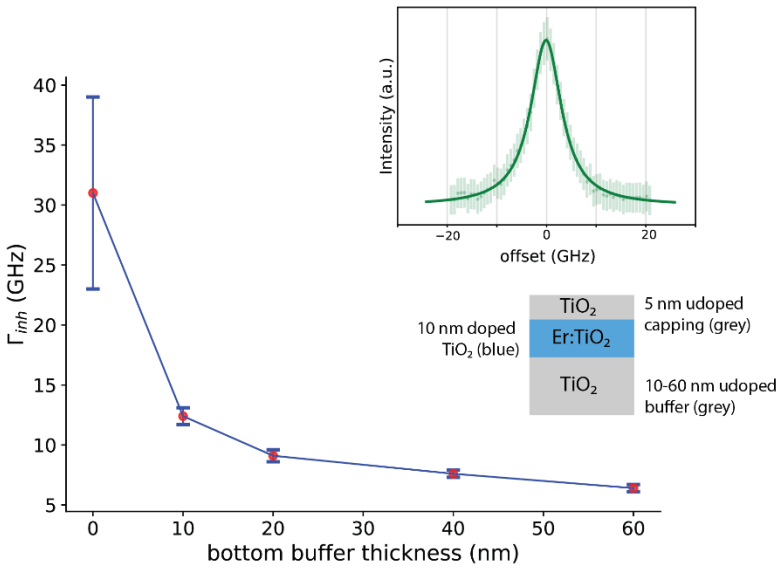

Figure 24. Inhomogeneous linewidth of Er:TiO_2 on silicon as a function of bottom buffer layer thickness between the silicon and the TiO_2. The narrowest linewidth was obtained for the 60-nm bottom buffer (inset). The schematic shows an erbium doped thin film (blue) with a top cap and bottom buffer of undoped TiO_2 (grey).

We also explored the effect of Er concentration and temperature upon the broadening of Γ_{inh}. We prepared a series of anatase films with structure 40 (undoped bottom buffer)/10 (doped film)/5 (undoped cap) nm and with different Er doping concentrations (by the varying Er source temperature) and with the substrate temperature at 480 C. The results of the measured Γ_{inh} values are shown in Figure 5(a). For our baseline erbium density (36 ppm) we estimate ~$3.2*10^{18}$ erbium atoms per cm^3, (avg. spacing between Er then is ~6.8 nm). It is clear from the data that at (and under) this concentration, the inhomogeneous linewidth is not degraded by concentration effects.

For the temperature dependence we used a film with a structure of undoped bottom buffer (40 nm), doped film (20 nm) and undoped cap (10 nm) and measured the linewidth at 3.5K, 6K, 10K, 20K and 40K. From the curve fitting we see that the temperature effect does not seem to offer improvement in the linewidth at lower temperatures (<3.5K) as the temperature effect plateaus off.

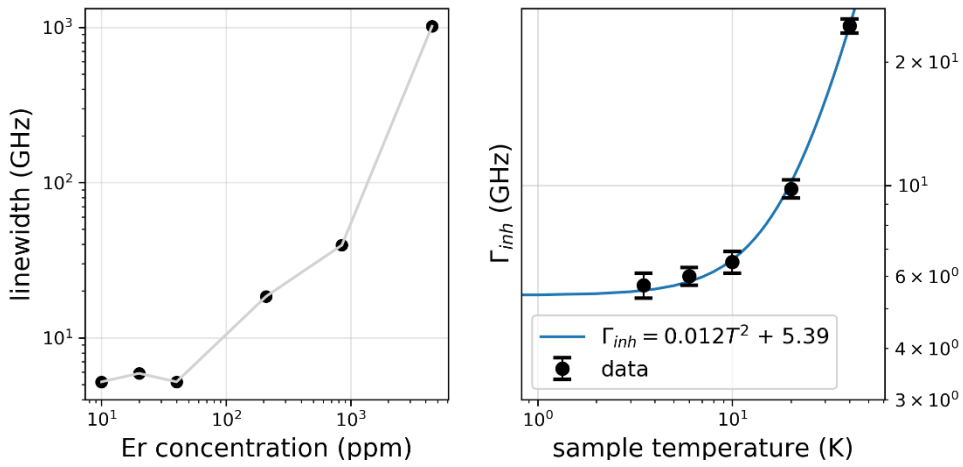

Figure 25 (a) We assess the contribution to Γ_{inh} coming from erbium concentration and (b) sample temperature. We find that our baseline concentration is low enough to not be a source of linewidth broadening; no major gains are expected from going to a lower temperature (<3.5K) either.

Following the measurement of the inhomogeneous PL linewidth, it is also important to measure the optical dephasing rate (T_2*) as a metric for qubit applications. While we were unable to perform the direct measurement due to the fast-dephasing time, we were able to extract an upper limit on T2* via an indirect method (described briefly in the methods section) based on transient hole burning as described by Weiss et al.[71] Through this, we are able to get an upper limit on homogeneous and spectral diffusion linewidth of the erbium ensemble.

We measured the spectral diffusion on several samples with varying bottom buffer thickness, capping layer thickness, and dopant concentration and the results are summarized in Figure 26. Three observations can be made regarding the spectral diffusion linewidth: (1) there is an improvement with the buffer layer thickness, consistent with the results for the inhomogeneous PL linewidths; (2) there appears to be a slight improvement with a lower doping density, specifically a ~20% decrease the spectral diffusion linewidth with a three-fold reduction in the Er^{3+} concentration; and (3) an increase in the capping thickness from 10 to 20 nm yielded a large reduction in spectral diffusion linewidth (~50%). These factors are likely due to higher sensitivity

of spectral diffusion to charge defects at, and the proximity to the surface. We note that such ionic oxides can be affected by moisture penetration from the ambient air[72]. Together, these three factors suggest that we can be optimized further to improve spectral diffusion.

3.5 DISCUSSION

Several conclusions can be made from the above results, in terms of positioning such RE: wide gap host films for solid-state quantum devices. Firstly, the PL linewidths seem fairly insensitive to the crystallinity of the host films. This is an important finding as it implies that PL quality and the optical linewidth is currently limited by other materials effects. From a practical perspective, the use of polycrystalline host material might make device fabrication easier. The insensitivity of the PL to extended defects is unlike the case of PL in semiconductors (such as the III-V compounds) and is likely due to the protected f-shell radiative transitions and less "band-like" characteristics of the participating states. We speculate that the PL may be controlled by other defects such as charged point defects that arise from deviations in stoichiometry, and which are well known to exist in such ionic oxides. These effects, if relevant, would point to the future exploration of detailed annealing studies. Secondly, we show that the growth of a suitable buffer and a top capping layer is necessary for improved optical properties (both homogeneous and inhomogeneous linewidth). Thirdly, we point out that a combination of these techniques enables the ability to engineer thin film properties to get to a useful range of relevant properties (linewidth, spectral diffusion etc.). We will note that while erbium doped TiO_2 (anatase) system has been studied over the last several decades[73], it has been done in a different context (catalysis, upconversion etc.) with no direct point of comparison for the QIS relevant properties discussed here.

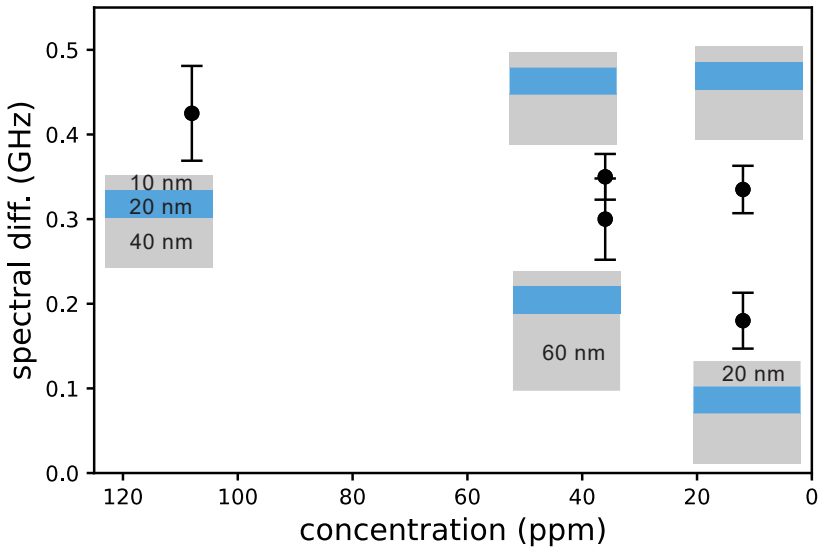

Figure 26. The optical spectral diffusion bandwidth as a function of Er concentration and the thickness of the top/bottom buffer layers. Each datapoint is accompanied by a layer structure, unless otherwise noted the top cap layer is 10 nm (gray); the doped region is 20nm (blue) and the bottom buffer is 40 nm (gray).

3.6 CONCLUSION

Our primary goal with this study was to characterize TiO_2 as a host material for erbium especially when it comes to controlling the emission wavelength within the C-band. We have shown that we can engineer the properties of erbium doped thin films, using a combination of substrates and doped/undoped structures. One of the key findings has been that the polycrystalline films show better inhomogeneous linewidth compared to the single crystal thin films. The better performance of the polycrystalline cannot be attributed simply to fully relaxed nano crystallites, and hint at other mechanism at play that are not fully understood at this point. We also show that, by adding bottom buffer and top capping layers, we can bring the inhomogeneous linewidth to target levels while keeping the overall film thickness small. Further, the spectral diffusion can be controlled through the erbium concentration and by adding undoped buffers. Spectral diffusion is seen to be

more sensitive to the thickness of the top capping than the bottom buffer emphasizing the role of defects on the top interface.

Silicon compatibility and the ability to integrate these polycrystalline films directly with silicon device fabrication, enables a significant technological advantage. Future work involves using this platform to fabricate sparsely doped thin films into high-Q resonators to achieve good coupling between Er^{3+} ions and optical fields to push toward coupling with small ensembles and possibly single ion quantum memories. The increased optical depth offered by a photonic device on this platform would also allow us to probe lower concentrations and develop capabilities to directly measure key quantum properties of the erbium dopant such as the coherence time – allowing us to investigate the nature of the Er/defect interactions dictating the linewidth and spectral diffusion.

3.7 ACKNOWLEDGEMENT

This work was primarily supported by the Center for Novel Pathways to Quantum Coherence in Materials, an Energy Frontier Research Center funded by the U.S. Department of Energy, Office of Science, Basic Energy Sciences under Award No. DE-AC02-05CH11231. This material is also based upon work supported by the U.S. Department of Energy, Office of Science, National Quantum Information Science Research Centers, under Award Number DE-FOA-0002253. Use of the Center for Nanoscale Materials, an Office of Science user facility, was supported by the U.S. Department of Energy, Office of Science, Office of Basic Energy Sciences, under Contract No. DE-AC02-06CH11357. S.G. acknowledges the Vannevar Bush Fellowship under the program sponsored by the Office of the Undersecretary of Defense for Research and Engineering (OUSD (R&E)) and The Office of Naval Research as the executive manager for the grant.

3.8 SUPPLEMENTARY MATERIALS

Development of a Scalable Quantum Memory Platform—Materials Science of Erbium-Doped TiO2 Thin Films on Silicon

Manish Kumar Singh[1], Gary Wolfowicz[2], Jianguo Wen[3], Sean Sullivan[2], Abhinav Prakash[3], Alan Dibos[2,3], David Awschalom[1,2], F. Joseph Heremans[1,2], Supratik Guha[1,2]*

[1]Pritzker School of Molecular Engineering, University of Chicago, Chicago, IL, USA 60637

[3]Materials Science Division, Argonne National Laboratory, Lemont, IL, USA, 60439

[2]Center for Nanoscale Materials, Argonne National Laboratory, Lemont, IL, USA, 60439

[†]Corresponding authors: Supratik Guha (guha@uchicago.edu)

In figure 27, the EDS scan of the interface for TiO2 on silicon shows that the interface is primarily SiOx and is about 3.5nm for the rutile (fig 27(c)) and about 1.5 nm for the anatase sample (fig 27(d)). This is likely from the oxidation and in-diffusion of oxygen to the interface from the surface and is higher for the rutile film grown at higher temperature compared to anatase (750 °C vs 480 °C).

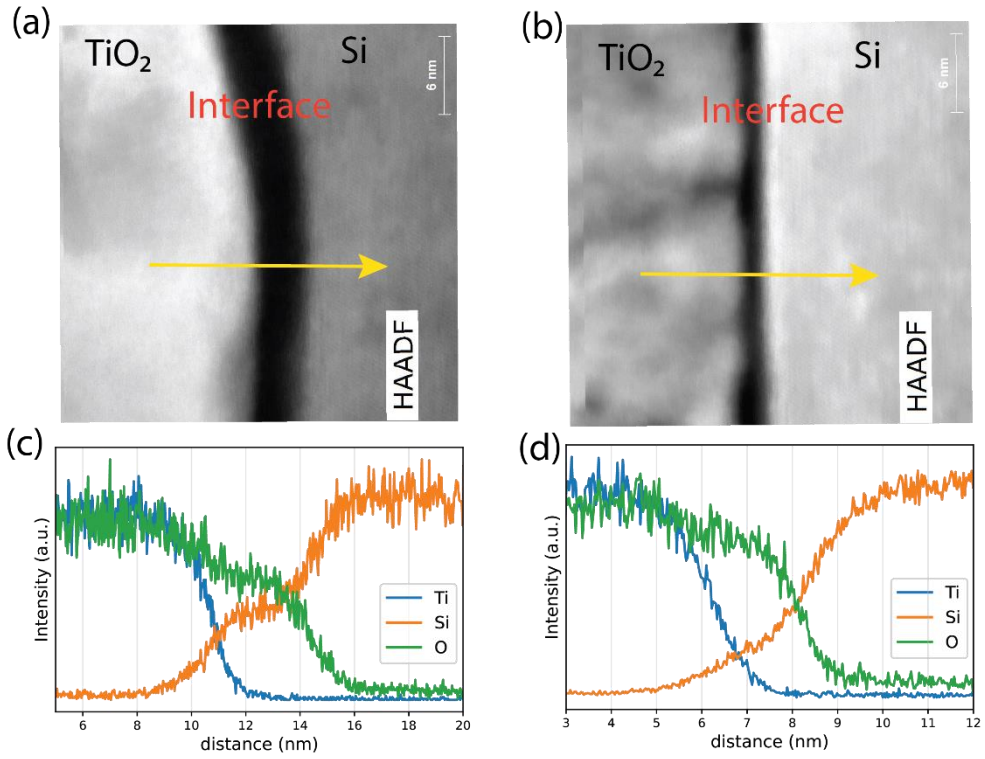

Figure 27 (a-b) A high contrast image of the region scanned by energy dispersive spectroscopy (EDS). The yellow arrow indicates the direction of scan. (c) EDS scan for the rutile sample (in (a)) shows the presence of an interfacial layer that is primarily SiO_x and about 3.5 nm in thickness (d) EDS scan for the anatase sample shows an SiO_x layer ~1.5 nm in thickness. The difference is likely due to the higher growth temperature of the rutile sample.

Integration of selective area electron diffraction images taken over 25 different areas on the film cross section – for both the rutile and anatase polycrystalline films – confirms that there is a preferential growth direction. It also suggests some degree of epitaxial relationship with the Si

(100). This might be secondary to the fact that the rutile (110) and anatase (101) are the thermodynamically preferred growth directions. The data is presented in figure 28.

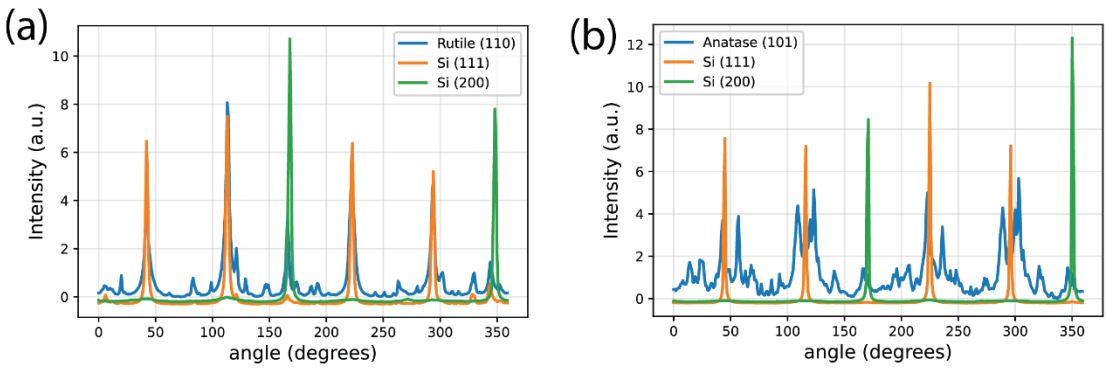

Figure 28 (a) Comparing intensities corresponding to Si (111), Si (200) and rutile using SAED data averaged over 25 points. The rutile is primarily (110) indicating the predominant growth direction and structure and appears well aligned to the Si(111) (b) Comparing (b) Intensities across anatase, Si (111) and S(200) shows that (101) is the preferred direction for anatase. The alignment is not very clear but appears aligned with Si 200.

Atomic force microscopy (AFM) using a Bruker Dimension Icon was used for surface roughness characterization, an important factor for optical waveguides. The scan was done over an area of 2um square. Root mean square (RMS) roughness of 0.8 nm was observed for a 9.9 nm (fig 29(a)) and 1.7 nm for a 35 nm sample (fig 29(b)) for films on Si (100). Overall, as the fit in fig 29(c) shows the relationship appears to be linear and monotonic.

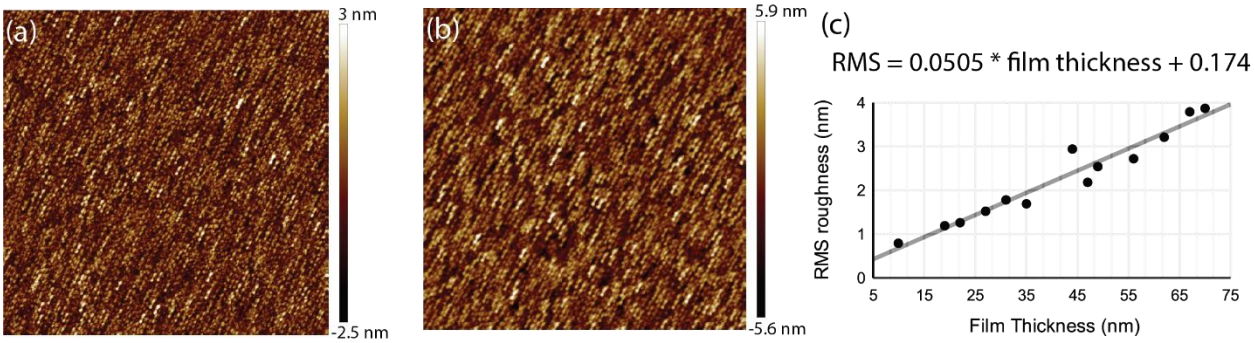

Figure 29 Results of AFM characterization are summarized. (a) a 9.9 nm anatase film grown on Si (100) shows a roughness of 0.8nm (RMS). (b) This rises to 1.7 nm for a thicker sample of 35nm (c) Overall, the relationship between film thickness and roughness appears to the linear.

4 NANOFABRICATION TECHNIQUES

Nanofabrication, the ability to create structure on substrates, forms the basis of high-tech gadgets today. This is the set of technologies that have impacted every aspect of the modern world. For example, in cars, this has led to improvements such as automated safety features and nanofabrication enabled technologies is what is pushing the envelope on autonomous driving; in phones, this has enabled cameras to get small enough to fit in our phones and through the ever-improving microprocessor has turned the old "cellular phones" into powerful computers.

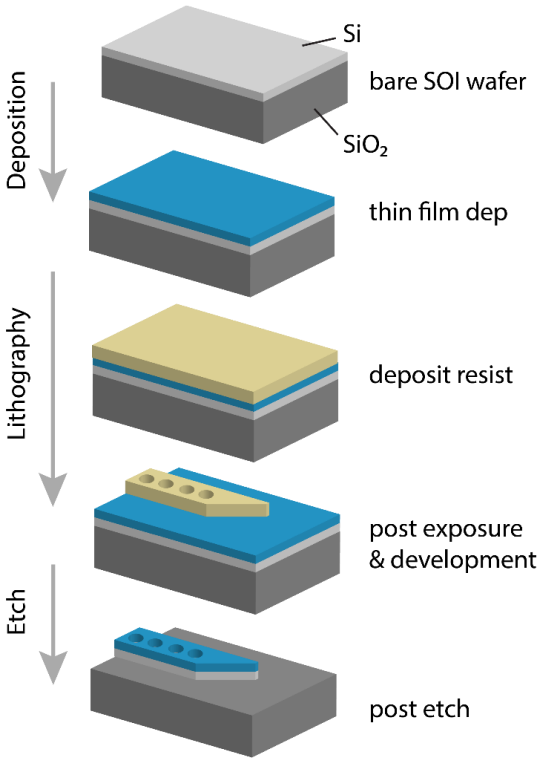

Figure 30 A schematic of steps that would create a device on our platform using nanofabrication techniques.

4.1 PROCESS FLOW

A typical fabrication flow for one short cycle would consist of deposition of the following step: 1. Deposition of desired material 2. Photoresist and development (lithography) 3. Pattern transfer via etching. Note that what is outlined in steps 1-3 is a simplified subtractive process, and steps 2 and 1 could be switched, and steps like chemical mechanical polishing added to make this an additive process. 100s of these cycles are used in the modern electronics industry is what allows us to go from silicon to a microprocessor. A schematic of device fabrication process flow is shown in figure 30 – the schematic shown is for the development of 1D photonic crystals, but the same flow series of steps can be used for waveguides, ring resonators, disk resonators, etc.

4.1.1 Deposition

Deposition of the desired films can be done using any of the techniques briefly described in chapter 1 – sputter, CVD, ALD, MBE, whichever one is best suited to obtain the desired properties. In some cases, the deposition might simply be a standard hard mask – a term that refers to a sacrificial layer that protects the films/substrate of interest in cases where the etch selectivity between resist and substrate is not sufficient for the pattern transfer.

4.1.2 Lithography

Pattern definition is achieved using photolithography – a technique that derives its name from the Greek for "writing with light." As the needs of the semiconductor industry have grown, the capability of defining lower and lower dimensions using lithography has also improved – going all the way to extreme-ultraviolet (EUV) techniques for the 3-5nm nodes. In the academic lab environment, we typically do not have access to these high-end industrial techniques, and the capabilities typically available are (1) lithography using 405 or 375 laser, which works very well for features of size 0.8um or larger (2) e-beam writing – this is a slow process but has the advantage of defining very small features up to 10 nm using a focused e-beam. Both require specialized chemicals (photoresist or e-beam resist) that can be developed following an exposure using either a light or high-energy beam. These can be positive resists where the exposed portion becomes the solution and is removed during development or negative photoresist which behaves in the opposite manner – each useful for its specific process. There is a wide selection of these resists that have been developed to give a high degree of accuracy for pattern transfer, feature control, high selectivity during the etch process that follows development.

4.1.3 Etching

For etching, there are two major approaches – we can use wet etching, which involves using a liquid etchant to remove the desired materials from the substrate. This works very well when it comes to removing a blanket film – native oxide or a hard mask. One important example is the wet etching of silicon using tetramethylammonium hydroxide (TMAH), where the high selectivity between Si (100) and Si (111) is used to etch features that are eventually used to engineer electron mobility. Wet etch, in general, is an isotropic etch, i.e., etch rates are direction agnostic, a property used for achieving uniform etches. Dry etch, which relies on a combination of physical and chemical processes, on the other hand, is generally anisotropic and has high directional dependence. A property that is used to achieve faithful feature transfers from the photoresist to the substrate. The degree of isotropy and etch uniformity, however, can be controlled by a combinator of factors – bias voltage, plasma power, the chemical composition of the etchant, etc. – and is useful for controlling features such as sidewall angles and roughness[74]. Dry etching relies on the formation of volatile reaction compounds that can easily desorb or can be gently sputtered away using a mixture of heavy gases such as argon with the primary reactant like Cl, F, BF_3, CH_3F, etc. The reaction is typically plasma-enhanced – this results in better directionality and more reactive species, making plasma, bias, flow rate, and the ratio of the reactive gases primary optimization parameters. A wet clean step is also added toward the end in most cases to remove any debris resulting from the etch. A wet clean for debris removal works through the principle of electrostatic repulsion between the substrate/feature and debris – this becomes especially important in cases with suspended and high aspect ratio structures where the use of a physical approach would not be possible.

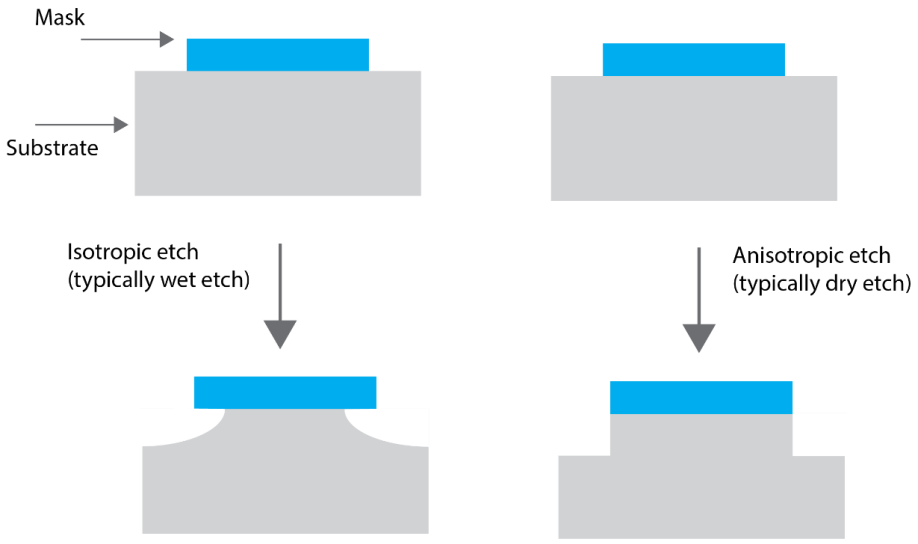

Figure 31 Schematic illustrating isotropic and anisotropic etching

4.2 PROCESS CHALLENGES FOR Y_2O_3 AND TiO_2

For oxides that do not form volatile halides (CeO_2, Y_2O_3, etc.), the primary method of etching is physical – this involves using heavy gases accelerated over a large potential to sputter away the material. This physical etching necessitates the use of hard masks (SiO_2, SIN, Cr, etc.), which, compared to the photo or e-beam resist, can withstand the process with a favorable etch selectivity $\left(\frac{rate_{film}}{rate_{hardmask}} > 1\right)$. However, this reduces the degree of control over structure roughness and sidewall angle. To give a better idea of the challenge here, figure 32 shows the SEM images of the results from the Y_2O_3 etch. This was an attempt at developing etch recipes for Y_2O_3 films grown on silicon. A range of thicknesses 50nm – 400 nm was used for the recipe development, and we see some dependence on the film thickness and hard mask. Two different hard masks were used the easily removable SiO_2 for the thinner films and Chromium for the thicker films. Figure 32(a & b) shows the rough sidewall that we get on Y_2O_3 etch – the submicron roughness is apparent. This was improved in later runs by reducing the argon flow rate and the bias and plasma power, but the roughness is still apparent (fig 32(f)). The baseline design pattern used for these test runs in figure

32(c) consisted of disks (20um and 100um in diameter) and a rectangular pattern for inspecting sidewall roughness – using a straight line as a reference. After the argon etches of the Y_2O_3 layer, SF6 was used for a somewhat isotropic dry etching of silicon; the resulting resonant disks are shown in Figures 32(d) and 32(e) – where the former is 20um in diameter and the latter is 100um. However, due to the strained nature of the film, the smaller disk is very clearly warped. The warping is not very clear in the other case due to the larger diameter in the other case. Due to the sidewall roughness and warping in these films, attempts to couple with these disk resonators failed. It might have been possible to achieve this using a thin film grown on a silicon-on-insulator (SOI) wafer. However, that avenue was not pursued further due to discouraging sidewall roughness, unavailability of SOI substrate, and unavailability of the test setup at the time.

Finally, the inhomogeneous linewidth that we observed in erbium-doped Y_2O_3 was much broader than anticipated – one potential reason for that is stress from the lattice mismatch. To characterize the stress, we tried fabricating cantilever and suspended using Argonne, and XeF_2 recipes are also shown in figure 32(f) (g) for the former and 32(h) for the latter. However, due to the warped film in all three cases, these structures were useful for further optical characterization.

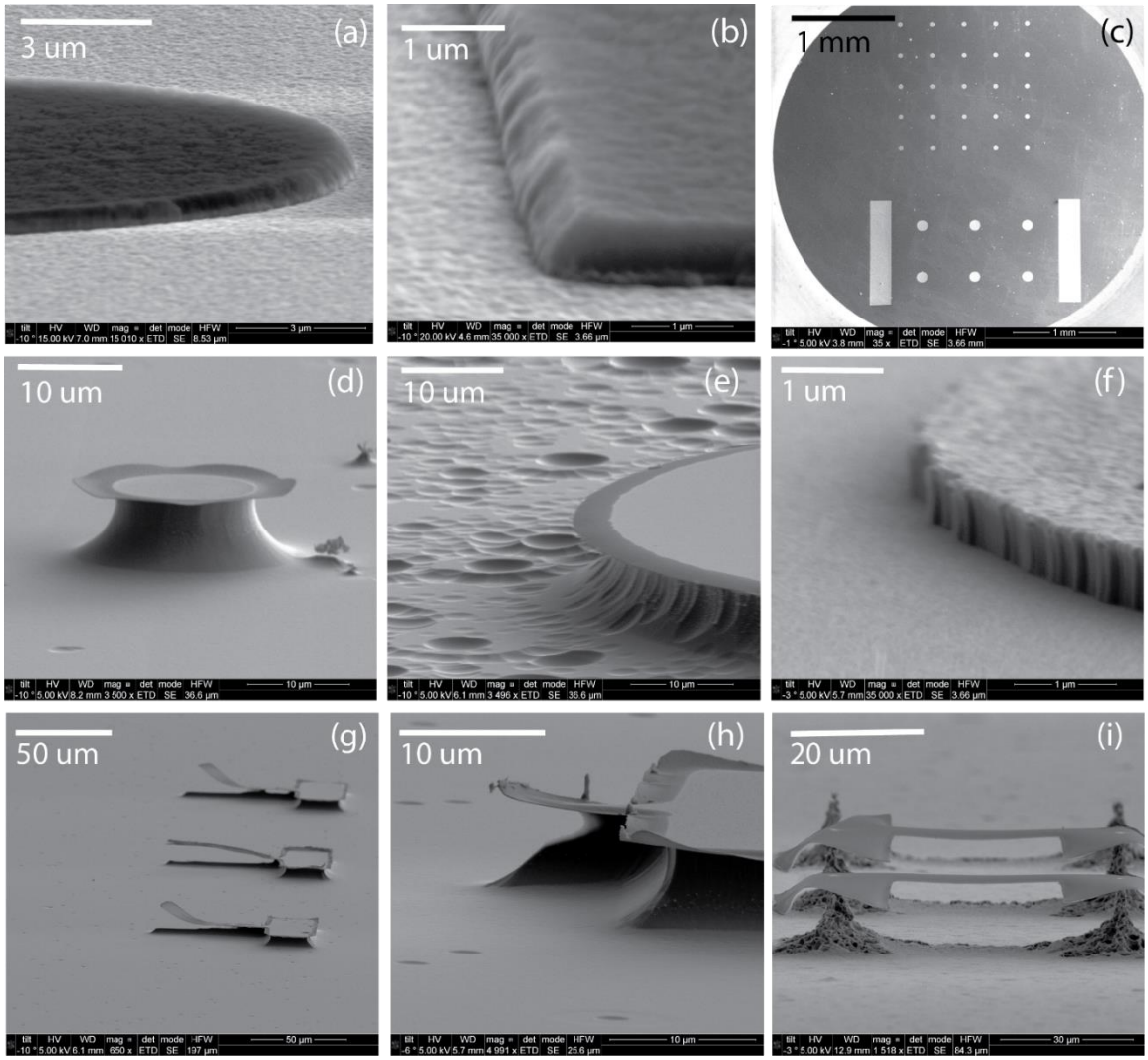

Figure 32 Fabrication attempts using Y_2O_3 had many issues, stemming primarily from Y not having volatile halides; additionally, low etch rates led to poor etch selectivity and control (a-b) SEM of circular and rectangular features etched on Y_2O_3 shows sub-micron roughness (SiO_2 hard mask) (c) Pattern used for the test etch runs (rectangles, disks of 100um and 20 um diameter) (d) disk resonators with a diameter of 20um showed clear signs of films warping, evidence that the film was strained (due to the epitaxial matching condition) (e) disk resonators with a diameter of 100um did not show warping for the same amount of under etch. (f) For thicker films (using Cr as hard mask) the edge roughness on the disks was very poor (g-h). Cantilevers and suspended structures were fabricated to allow for characterization of strain-free thin films. However, the warping coupled with characterization setup limitations meant that it could not be used as intended. [fabrication and SEM by Manish Singh]

Sidewall roughness is typically controlled using a mixture of physical and chemical methods (e.g.,

Ar + SF_6 in the case of silicon) and optimizing the ratio of the two. However, as has been noted,

due to the purely physical nature of the etch – this avenue was not available. For the case of TiO_2 and silicon, we clearly see the angled sidewalls in figure 33(a) - this gives the range of options with TiO_2, and silicon can be optimized for a better sidewall angle. However, the structure with angled sidewalls is good enough for the current goal, and the ease of etching using straightforward chlorine chemistry means that the optimizations remain to be performed. The roughness and feature definition of etching is seen in the SEM of the photonic crystal (figure 33 (b)). There are, however, potential issues with residue post-etch (figure 33 (c), rightmost waveguide) – this might be leading to an uncharacterizable device, a wet etch will be a useful step to add in future runs.

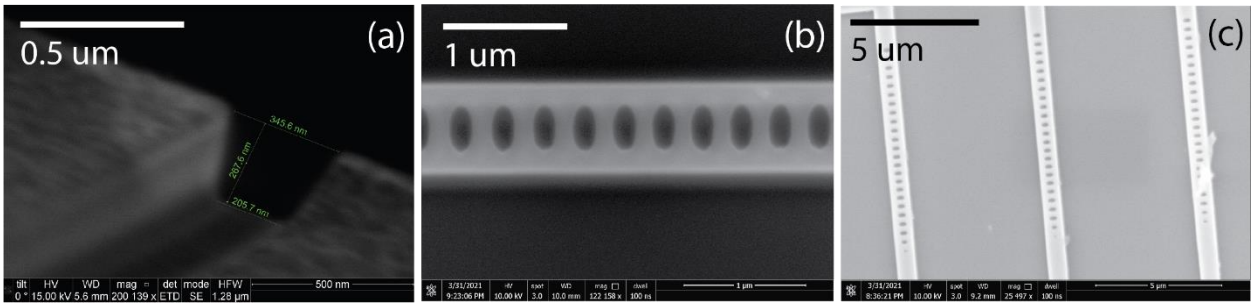

Figure 33 Compared to Y_2O_3, TiO_2 fabrication was relatively straightforward as Cl is known to be a good etchant and several recipes are available in the literature. (a) SEM image of a waveguide structure used to quantify the combined etch rates of TiO_2 & Si (b) A high-magnification SEM image of the 1D photonic crystals shows smooth sidewalls and well-defined sub-micron features (post-etch) (c) batches of devices fabricated had some debris (center and right waveguides) [fabrication by Alan Dibos, SEM by Manish Singh]

4.3 ADDITIONAL CHALLENGES

The primary characterization and optimization of Er-doped TiO_2 films were performed on Silicon 100. To be able to fabricate a nanophotonic device, we transferred this know-how from Silicon to SOI and worked with our collaborator (Dr. Dibos) to use this platform to demonstrate the fabrication of devices, characterization of the one-dimensional cavity, and demonstration of Purcell enhancement. SOI is a dominant platform for high-contrast waveguide-based design – with silicon nitride (SiN) being another popular alternative for photonic systems. Commercially

available SOI has a silicon wafer as a "handle layer," with a 2um SiO_2 layer on top called the buried oxide or BOX and on top of this is another 220 nm silicon called the device layer.

Having optimized the film growth of Er:TiO_2 on Si (100), the direct transfer to a Si (100) device layer on SOI was straightforward. However, we discovered through spectroscopy that the expected phase of TiO_2 was different on SOI than that obtained on Si. In order to investigate this, we used the eutectic point of Au and Al to compare the behavior of the two substrates. Using the Al eutectic, we found that for the eutectic point, the SOI corresponds to higher silicon temperature – a trend supported by the Au eutectic. This highlights the difficulty and additional due diligence needed for transferring growth techniques even for similar substrates. Note that this might not entirely be the effect of the layered structure. The size of the substrate and the substrate holders during growth is also different and might contribute to the observed differences.

4.4 DEVICE FABRICATION AND KEY DEMONSTRATIONS

Photons are capable of traveling long distances without loss as they have minimal interaction with the environment – and hence are an ideal form for transferring quantum information as what's called "flying qubits." On the other hand, in order to store, manipulate this information interaction, we need to interface this with an atom or ensemble – this is where the property that makes light a good flying qubit becomes detrimental, and further engineering is needed to achieve storage and manipulation. The simplest system here is the interaction between a photon and atom – this is described by what's called the Jaynes-Cummings Hamiltonian. By using carefully designed photonic cavities, we can engineer the system such that a single optical mode interacts strongly with the atom. This photonic cavity acts similar to a "cage" where the photon gets trapped in an engineered segment – bouncing around inside before exiting the cavity. The goodness of such a

cavity is characterized by the quality factor – which measures the cavity's ability to store energy and is estimated in the figure below using

$$Q = \frac{\lambda_{cav}}{\delta\lambda_{fwhm}}$$

Where λ_{cav} is the absorption peak and $\delta\lambda_{fwhm}$ is the FWHM of the peak obtained using a Lorentzian fit. The cavity also modifies the density of optical states – around the emitter wavelength as engineered – leading to an increase in emission rate. This result of this effect on emission rate serves as another important metric called the Purcell factor esmitated as $P = \Gamma_0/\Gamma$ where Γ is the modified optical decay rate and Γ_0 the unmodified rate.

The goal of this thesis was to develop a platform that is a viable candidate for silicon-compatible integrated quantum photonics. Working with our collaborators, we have been able to demonstrate these two key elements. The first is the demonstration of fabricability through high Q photonics crystals. Figure 34(a) shows a nanophotonic cavity with a Q of ~160,000 underscoring the fabricability of this platform (Er:TiO_2 on SOI). A 40nm TiO_2 film on SOI was used for this fabrication. The characterization was done at room temperature – the resonant frequency of 1535.16 nm at room temperature shifts to ~1521 nm at a temperature of 3K.

The second is a demonstration of engineerability and control through Purcell enhancement. This is especially important as the erbium atoms in TiO_2 are only evanescently coupled with the erbium atoms in the thin film layer atop silicon – the demonstrated Purcell enhancement of ~165 is particularly promising. Figure 34(b) shows the change in the time constant for optical excitation decay as the cavity was detuned from the Er:TiO_2 (rutile) transition at 1520.56. The measurement was performed at 3K. A full discussion of these results will be presented in a paper currently under preparation.

Further improvements in films quality, interface, and fabrication recipes should be able to push the Q higher and give us a higher Purcell factor, allowing access to a regime where we can interface with single erbium atoms.

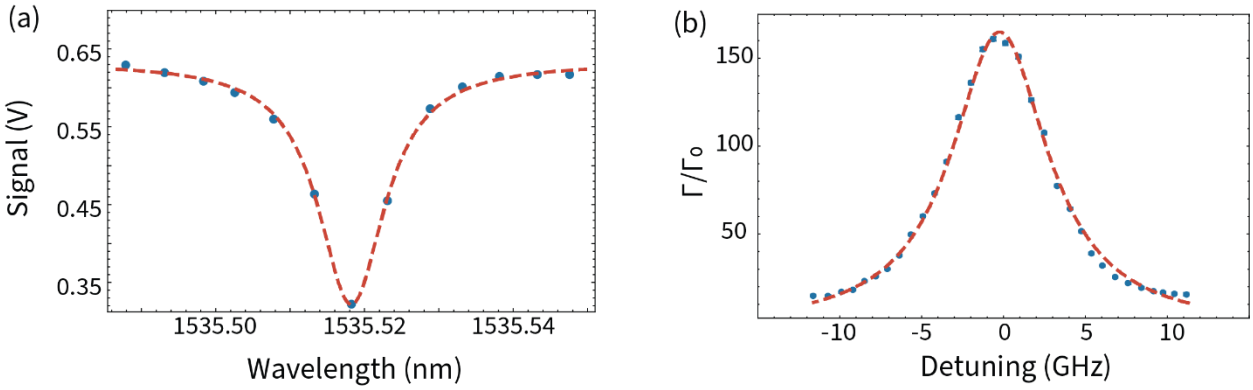

Figure 34 (a) The absorption peak of a high Q device, the Lorentzian fit to the data gives a Q of ~160,000 (b) The Purcell factor as estimated by the optical decay time constant is plotted as a function of detuning from the cavity. At resonance, we get a Purcell factor of ~165. Together these plots demonstrate the fabricability and promise of the Er:TiO_2 platform.

5 KEY DEVICE AND MATERIALS SPECIFICATIONS FOR A REPEATER ENABLED QUANTUM INTERNET

Manish Kumar Singh[1, +], Liang Jiang[1], David D. Awschalom[1,2], Supratik Guha[1,3]

[1]Pritzker School of Molecular Engineering, University of Chicago, Chicago, IL 60637, USA

[2]Center for Molecular Engineering and Materials Science Division, Argonne National Laboratory, Lemont, IL 60439, USA

[3]Center for Nanoscale Materials & Physical Sciences & Engineering Directorate, Argonne National Laboratory, Lemont, Illinois 60439

[+]Author to whom correspondence should be addressed: manishks@uchicago.edu

 The published manuscript is available at DOI: 10.1109/TQE.2021.3098440

5.1 ABSTRACT

Entangled photons can be used to create a truly secure communication link between two parties. However, the distance over which this can be achieved is limited by the transmission losses associated with optical fibers. One potential solution is using quantum repeaters (QRs) where initial entanglement is created over short distances and then extended via entanglement swapping. The system level performance metrics (data rate, fidelity of entanglement etc.) impose demands upon the hardware components (of a QR) which can be used to guide applied materials and device design towards these objectives. This has become increasingly important with an expanding list of candidates for quantum technologies, as the physical realization of each qubit or detector technology brings its own set of advantages and disadvantages. In this paper, we present a framework that uses a modular model of a QR and highlights the trade-offs that exist between technological component modules. Using reported values, we take a near-term perspective and show the achievable range of rates as a function of distance and the corresponding requirements on matter qubit properties.

5.2 INTRODUCTION

The major challenge in efficient communication of information using entangled photons over long (>100 km) optical fiber links comes from the transmission loss of photons [75,76]. Quantum repeaters (QRs) have been proposed [77,78] to overcome this by enabling the distribution of an entangled pair over long distances (referred to henceforth as a quantum link). Analogous to classical repeaters, these act as nodes between short-haul distances along the fiber but unlike classical repeaters do not amplify signal or transport photons, rather serving only as intermediaries during the quantum link creation. Direct quantum links between two points over optical fiber has been demonstrated for up to a few tens of kms [79] [80] for matter based memory nodes and over >1000 km through space

using a satellite based quantum link [81] for distribution of photonic states. A recent experiment demonstrated an important step forward for the former approach – the capability to create links using three memory nodes [82].

Much theoretical work has been done towards analyzing and improving the performance of a quantum link. This includes protocols and analysis for using different platforms, multimode memories [83], minimizing physical resources [84], new experiments [85,86], encoding [87,88], error correction [89–91]; and network level analysis [92–96]. As interest develops in building practical links [97,98], there is a need to translate system level performance into targets at the device and materials level for engineering impact. This is an approach that has been pioneered by the silicon microelectronics community (see for example refs. [99,100]). In this work we present a codesign perspective for quantum repeaters. Building on existing models ([78], [101], [102]), and modifying the analysis for real world performance of solid state qubit platforms, we lay out a modular framework that evaluates attainable data rates for a QR enabled quantum link as a function of various material and device parameters of interest. This approach is then used to outline benchmarks based on demonstrated properties of materials and devices.

We use a first generation, heralded quantum communication model (that we believe has the most potential for successful deployment in the shorter term; described in SI) for our estimates and adapt a recently proposed scheme [101] for analysis. Many of these principles and discussion directly map across qubit platforms and can be a straightforward extension to other systems.

5.3 BUILDING A REPEATER

The QR node should be capable of (1) initializing the qubits in the superposition state (2) creating qubit-photon entanglement and (3) executing an entanglement swapping operation. With multiple

repeater nodes, the nearest neighbor entanglement is performed asynchronously, motivating the need for a quantum memory [47] characterized by the qubit's coherence time (T_2).

Figure 35 shows the case of two QR nodes where we identify four major technology blocks that constitute a repeater chain. An *excitation block* (lasers and related components) used towards initialization, entanglement creation, retrieval of the qubit state etc. (yellow); a *control block* performs single and multi-qubit operations such as entanglement swapping (green), and a *memory block* which has the matter qubits (blue). Finally, there is a photodetector based BSM setup for entanglement creation: the *detector block.* A more detailed description of the entanglement process (along with references) is provided in the SI. A list of some of the key parameters for these blocks are defined here and will be used in the following discussion.

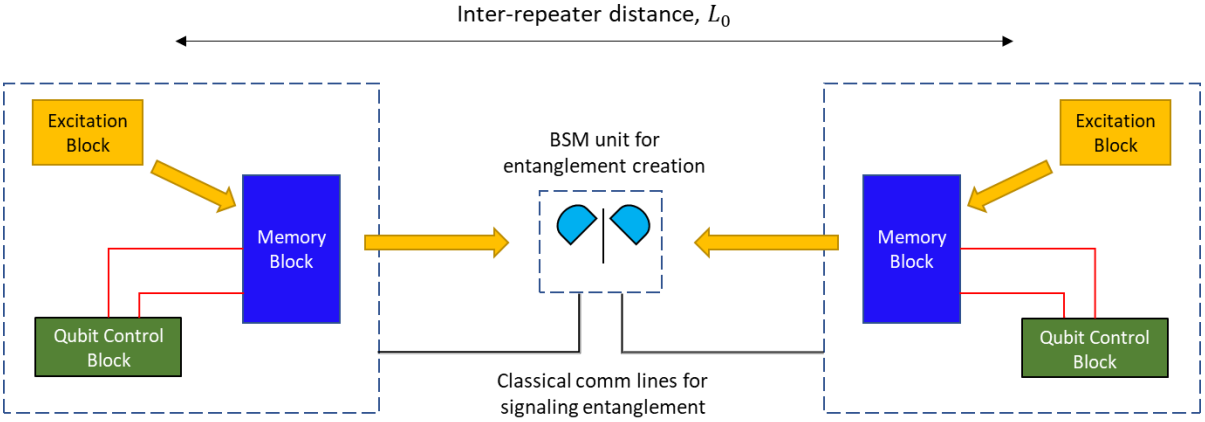

Figure 35 The figure shows a block diagram view of a quantum repeater and an elementary link. We show a BSM unit shared between two QRs separated by a distance L_0. The important components can be classified as "detector block (includes the BSM setup)", "excitation block", "memory block" and the "control block". The rectangle made by dotted line identifies what could qualify as a QR unit.

- Network level
    - L_0 – distance between neighboring repeaters

- L – total distance between end nodes
- η_t – transmission efficiency (photon loss)
    - Estimated as $\eta_t = e^{-\frac{L}{L_{att}}}$ with L_{att} ~21.7 km for 0.2 db/km loss
- η_{FC} – efficiency of frequency conversion if emission is not in telecom band
- η_c – coupling efficiency for light emitted by the quantum memory (inside a suitable nanophotonic structure)
- $t_0 - \frac{L_0}{c'}$ minimum time required for classical information transfer between QR nodes (c' is the speed of light in fiber ~2x10^5 km/s)

- Node components
    - Detector Block
        - η_d – detector efficiency (% of incidences correctly reported by detector)
        - D – dark count (false positive)
        - t_{dead} - dead time
    - Excitation Block and Memory Block
        - t_{coh} – coherence time for memory qubit (also referred to as T_2 in the literature)
        - T_0 – time to generate an entangled pair
        - F_0 – entanglement fidelity between two qubits
    - Control Block
        - p_s – success probability of the entanglement swapping operation
        - t_{swap} – time for the two-qubit swap operation
        - η_{swap} – efficiency of the swap gate
        - t_{init} – time to re-initialize the qubit from an arbitrary state

Platform	Demonstrated properties			
	Coherence time (t_{coh})	**Entanglement Fidelity* (F_0)**	**Single Qubit Gate fidelity**	**Two Qubit gate fidelity**
NV center in diamond	0.58 s [103]	0.92(3) [79]	0.99995(6) [104]	0.9920(1) [104]
Trapped Ion	~600 s [105]	0.940(5) [106]	0.999934(3) [107]	0.999(1) [107]
Neutral atom	~7 s [108]	>0.92 [109]	0.9983(14) [110]	≥0.965(3) [111]
Rare Earths$^+$	1.3 s ($^{167}Er^{3+}$)[30] >10^4 s (Eu^{3+})[4]	-	-	-
Defects in SiC	64 ms [112]	-	0.99984(1) [113]	-
Si-V defects in diamond	>200 ms [114]	-	-	0.59(4) [114]

Table 1 Key properties that can serve as benchmark for quantum memory qubits as reported in literature. Quantum dots and superconducting qubits with much lower coherence times (< 1ms) have not been shown here. *Values for qubits at macroscopic distances. $^+$Values for rare earths are from ensemble measurement

We now analyze three of the key components of a repeater network, starting with memory. We focus on the single defect center or dopant based spin-optical interfaces as a memory element due to their scalability and chip scale compatibility [25]. Many candidates show promise and offer a range of values for storage time and operation fidelities. For first-level comparison the reported values of the coherence time are used. The values listed (table 1) are the highest reported values including the use of dynamic decoupling or other techniques. Other comparison points in Table 1 include demonstrated entanglement fidelity (F_0) as well as single and two qubit gate fidelities. A gain in t_{coh} as well as gate fidelity can be realized through material and heterostructure engineering. This includes studies using isotopically enriched NV centers [115], enriched Si for quantum dots [116], and selected isotopes for REI [6,30].

Second, we turn to optical transmission. A qubit with emission in the C-band is desirable (see SI for representative data) to minimize absorption losses in existing buried optical fiber networks.

This however limits the materials selection and highlights the need for efficient frequency conversion methods [117] for non-telecom wavelength emitters. We therefore include a related conversion efficiency (η_{FC}) in our analysis that is relevant when comparing material qubits.

Finally, we turn to the detectors. Ideally, the detector should detect every incident photon ($\eta_d = 1$), detect on-demand ($t_{dead} = 0$) and without false positives ($D = 0$). A summary of reported values for InGaAs based single photon avalanche diode detectors (SPAD) and superconducting nanowire single photon detectors (SNSPD) are given in table 2 for C-band operation. The SNSPDs offer significantly superior, and as will be discussed later –acceptable – performance but require low temperatures for operation (<10 K). This may significantly impact practicality, operation cost and scalability particularly for repeater stations in remote areas. The telecom range SPADs have a complex trade-off between (η_d, D, t_{dead}) with dark count and dead time varying directly with efficiency. They also suffer from unwanted defects that lead to after-pulsing, and their current performance capabilities are inadequate [118]. However, SPADs are increasingly being explored for other applications such as ranging [119], and improvements in performance can lead to scalable and higher temperature operation

(Telecom C Band)	SPAD [120–123]	SNSPD[124]
Detector efficiency ($\boldsymbol{\eta_d}$)	10-60%	96%
Dark counts (D)	100-1000 Hz	<100 Hz
Dead time ($\boldsymbol{t_{dead}}$)	0.1 – 100 us	<50 ns

Table 2 Comparing reported values of key metrics for SPAD and SNSPDs in the 1550nm telecom wavelength. For SPAD the dark counts, detection efficiency varies widely with the operation parameters

5.4 Quantum Link Performance

We will now lay out a model to evaluate a functional link comprised of the components outlined earlier and estimate the average time to connect (alternatively, rate of connection) as a performance

metric. Asadi et al.[101] give a relationship for the average time (T_L) it takes to create a repeater enabled quantum link of total length L and an inter-repeater distance of L_0:

$$T_L = \frac{f(m) * (L_0/c' + t_{init})}{p_{en} p_s^{m-1}} \quad (1)$$

Here, the number of QR nodes is $\left(\frac{L}{L_0} + 1\right)$, and m $\left(= \frac{L}{L_0}\right)$ is the number of segments in the link. The term $f(m) = 0.64 \log_2(m) + 0.83$ captures the average number of entanglement attempts needed (step 1 in figure 41), t_{init} is the qubit initialization time and p_{en} is the probability of creating an entanglement between two nodes (estimated as $\frac{\eta_t^2 \eta_c^2 \eta_d^2}{2}$). The analysis in Asadi et al. assumes that the $(m-1)$ entanglement swapping operations are performed simultaneously using deterministic gates ($p_s \sim 1$) and is accurate under the condition that the time for gate operations and readout is negligible compared to T_L. Considering that high fidelity deterministic gates are expected to be more challenging to implement on solid state qubit platforms and are therefore further out in the future [125], the above assumption of m-1 successful swaps to occurring simultaneously to create the end-to-end link may not be realistic for modeling currently implementable systems.

We therefore modify this equation for a probabilistic entanglement swap operation where the result of the gate operation involved in the swap needs to be communicated classically, this also holds true other aspects of control too. This approach has been recently used for instance in the feed-forward in three node entanglement swapping demonstration [126].

The required relation is obtained as follows. We proceed with entanglement swapping at alternate repeater nodes (figure 41 shows the case for 9 repeaters, m=8), first extending quantum links to a distance $2L_0$ (step 2, m/2 swap operations). In the next step, this is extended to $4L_0$ (step 3, m/4

operations) then to length $8L_0$ (step 4, m/8 swap operations) and so on in the case of higher number of repeaters till the end nodes are connected. The first set of m/2 swaps adds $t_0 = L_0/c'$ for classical communication, the second set adds $2t_0$ and so on with the final step adding $2^{n-1}t_0 = \left(\frac{L}{2}\right)/c'$ (where $n = \log_2 m$). This leads to a modified relation for T_L that considers the additional classical heralding overhead brought about by a probabilistic entanglement swap as noted earlier and results in the form given in equation 2. Note that there are other time consuming steps but reported values are small in comparison to the time to entangle e.g. t_{init}<100us [113], t_{swap}<1ms [127] and therefore have been ignored. We include t_0 as it increases with m and is further amplified for small p_s in the denominator.

$$T_L = \left(\left(\left(\left(\frac{f(m) \times \left(\frac{L_0}{c'}\right)}{p_{en}} \right) / p_s^{\frac{m}{2}} + t_0 \right) / p_s^{\frac{m}{4}} + 2t_0 \ \ldots \right) / p_s^2 + 2^{n-2}\, t_0 \right) / p_s + 2^{n-1} t_0 \qquad (2)$$

Using equation 2, we then simulate expected data rates as a function of device/material parameters using the following methodology. Included in the expression for T_L are two competing loss terms: (1) transmission loss (η_t), through the p_{en} dependence and, (2), operation loss ($\eta_{swap}, \eta_c, \eta_d$). In our simulations we identify an optimal L_0 (to the nearest km) for a given set of parameter values that balances these two losses to maximize the data rate. The operation loss depends on the form of p_s, for example, the model that we use is based on a modified Barrett-Kok scheme [101], which involves measurement of both qubits giving $p_s = \eta_{swap}(\eta_c\, \eta_d)^2$ – the scheme is robust against photon loss and is a representative example of a probabilistic entanglement swapping operation.

Furthermore, the rate at which we can create such links is also limited by the loss of fidelity from all the operations. As in [101] an estimate on the end-to-end fidelity can be obtained using the product of individual operations' fidelities: 2m qubit initializations (F_{init}), m qubit-qubit entanglement ($F_{entangle}$) and finally the (m-1) swapping operations which consist of one gate operation and two readouts ($F_{gate}, F_{readout}$). Putting this together yields $F_{end-to-end} = (F_{init})^{2m}\left(F_{entangle}\right)^{m}\left(F_{gate}F_{readout}^{2}\right)^{m-1}$. This final fidelity, a measure of the quality of the link needs to be above 0.5 for additional techniques like purification [128] to be applied and is similarly constrained for some encryption protocols [129]. This requirement implies that we constrain $F_{end-to-end}$ to > 0.5 – this limits the maximum value of m (as defined for equation 1 and 2) which limits the number of QR nodes and thereby the rate. We use the values provided in [101] for these fidelities (F_{init} =0.9996, $F_{entangle}$ =0.9996, F_{gate} =0.9996, $F_{readout}$ =0.9998) to enforce this constraint in our simulation.

To explore the dependence on each variable we choose a baseline set of detector, coupling, and gate swap efficiencies($\eta_d = 0.96,\ \eta_c = 0.9, \eta_{swap} = 0.9$) and vary one parameter at a time over a range that is guided by reported data and is shown in figure 36. Figure 36(a) shows the rate for variation in η_d between the low of reported SPAD value (0.6) and a high of 0.99; figure 36(b) shows η_c over a range of 0.4 and 0.99 based on the reported value for waveguide fiber coupling [62, 63]; figure 36(c) shows η_{swap} with a low of 0.5 (highest efficiency possible using the detector based BSM setup) and a high of 0.99 (close to predicted efficiencies in [101]). Given the polynomial dependence on m, it is unsurprising that the value of T_L spans multiple orders of magnitude at larger distances.

To get the full set of possible rates we also simulate a range of $(\eta_{swap}, \eta_c, \eta_d)$ values for link lengths of (200 - 2000 km). η_{FC} comes into play for emitters not in the telecom wavelength and based on the reported down-conversion value of 0.17 for NV center [117], we use $\eta_{FC} = 0.2$ in these estimates.

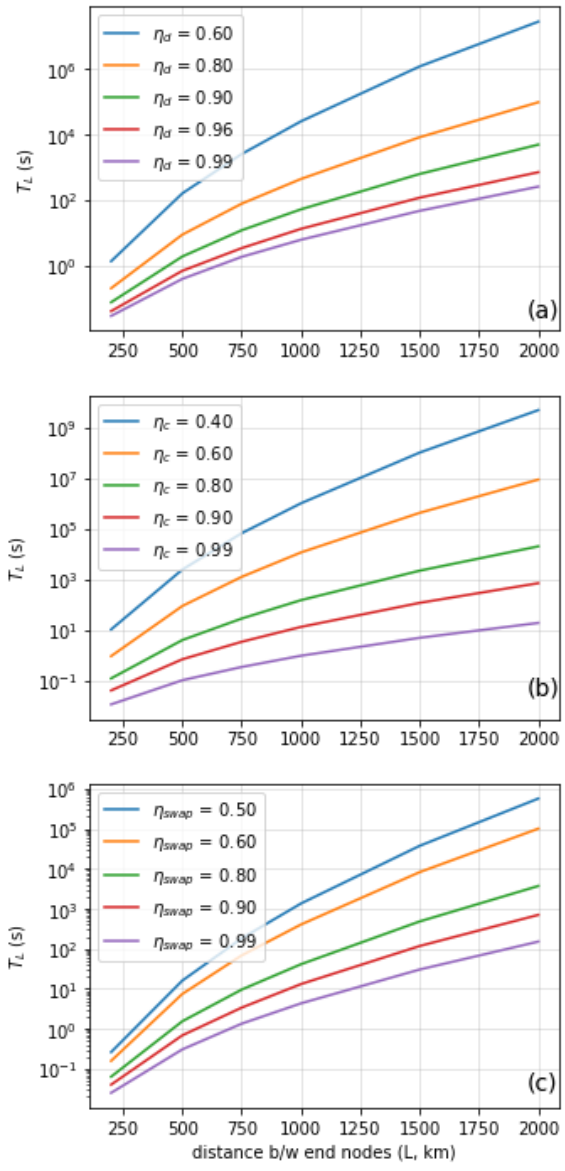

Figure 36 Variation in the time to connect (T_L) for a single variable with a given baseline of other variable from the baseline set of $(\eta_d = 0.96,\ \eta_c = 0.9, \eta_{swap} = 0.9)$

The maximum rates accessible for a range on constraints over four representative distances (200, 500, 1000, 2000) km is shown in table 3. We note that even for near ideal values (efficiencies up to 0.99) the maximum possible rates at 200km is ~300Hz which drops to 100 Hz (<20 Hz with frequency conversion) at 500 km. When we impose η_d= 0.96 and η_c =0.9 the rates drop to under 100 Hz at 200 km and under 10 Hz at 500 km. With limits on gate efficiency, rates drop further – as explored in figure 37, where we have chosen fixed values of L (200, 500, 1000) km and η_d (0.6, 0.96, 0.99) – the values for η_d are for SPAD, SNSPD. For η_{swap} and η_c, where there is still significant room for improvement, we have shown values in the larger range (0.4, 0.99).

From the contour plot it is clear that using SPAD it is impossible to achieve meaningful rates (>1 Hz) at distances of 500, 1000 km (figure 37(b) and 37(c)). It should however be possible to demonstrate such data rates at these representative distances using SNSPD efficiencies that have already been demonstrated - as shown in figure 37(d), a rate over 10 Hz should be achievable for L=200 km for a range of η_c, η_{swap} values. Improvements putting η_c, η_{swap} over 0.9 would further allow rates over 100 Hz. Similarly, improvements in detector efficiency to 0.99 will allow a larger range of η_c, η_{swap} values (figure 37(g)-(i)).

We should note that memory requirement (t_{coh}) is only dependent on the average time needed to create entanglement (step 1 in figure 41) and the additional time for classical communication. This can be estimated as $t_{coh} = T_0 + \sum_{k=0}^{n-1} 2^k t_0$ and sets the minimum $t_{coh}$for a given parameter set. Values corresponding to the parameter sets in figure 41 span the range 1.1-275ms [SI]. This range suggests that based on the values in table 1, several qubit platforms should be able to satisfy this requirement. Additionally, recent computational work [130] identifies a large number of materials with t_{coh} in this range.

It should also be added that the maximum data rate estimates we have made for the linear links above can be improved somewhat based upon specific algorithms and optimizations that increase the effective rate through resource management, fidelity tracking, optimal architecture etc. (see for instance refs. [90,92–94]). These benefits can have varying gains but need more resources. We also propose a method [SI] to utilize the idle repeaters in a linear chain to achieve a modest boost (up to 13% based on our estimates) in connection rate without using additional resources.

In the case of a high-fidelity deterministic gate ($p_s \sim 1$), eq (1) may be used directly. The rate thus obtained will be much higher than the case of probabilistic gates due to the lack of lossy operation terms and is given by the cyan curve in figure 38. This at the current stage can be viewed as an aspirational limit.

Projected maximum rate (Hz)				
Distance (km)	**unconstrainted**	$\eta_{FC} = 0.2$	$\eta_d \leq 0.96$	$\eta_d \leq 0.96$; $\eta_c \leq 0.9$
200	356.4	25.3	171.7	39.7
500	106.6	6.0	32.4	3.3
1000	30.0	1.5	6.1	0.2
2000	5.3	0.2	0.6	0.007

Table 3 Maximum rate at representative distances and conditions. The first column represents the max values in the full range simulated and the following columns show the values for addition conditions listed in the heading.

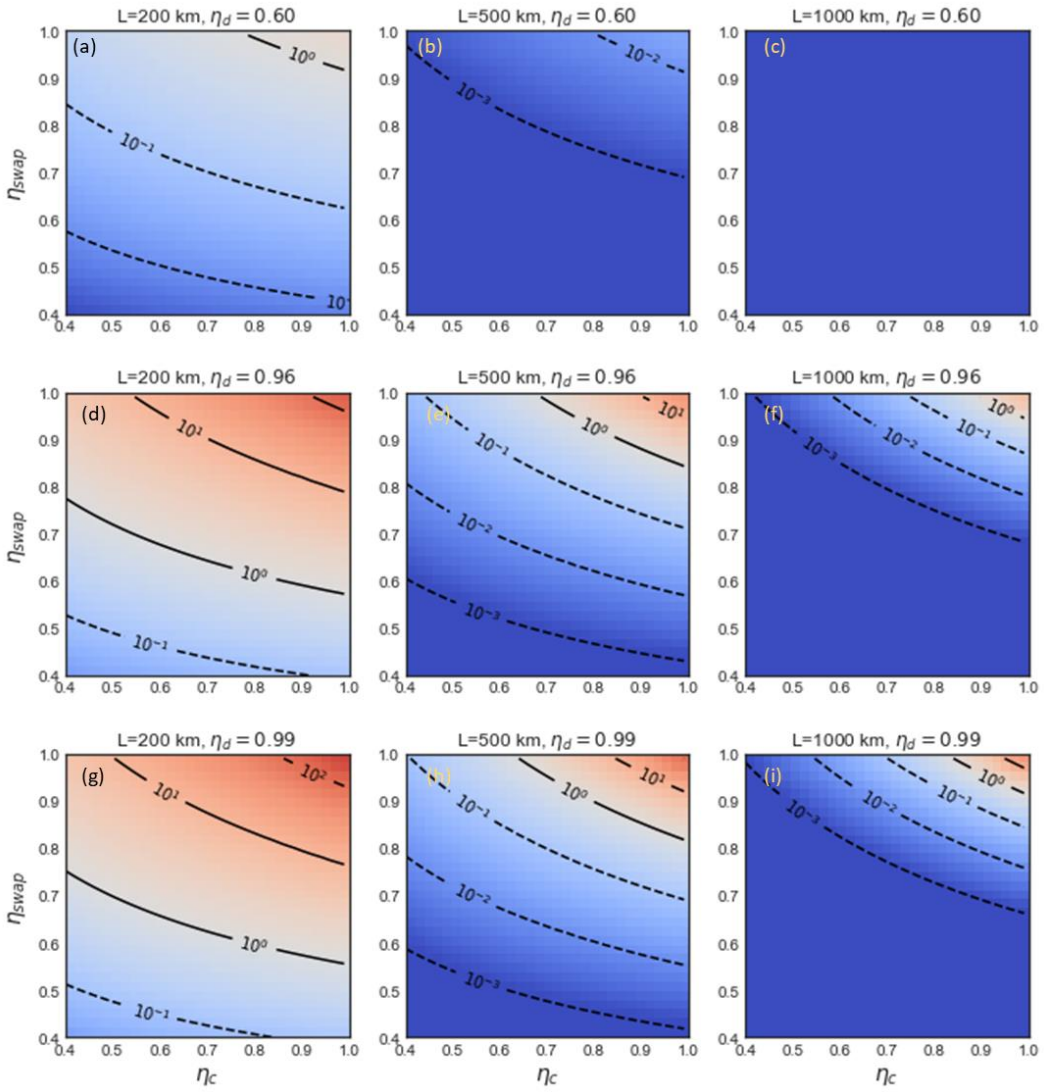

Figure 37 Contour plots showing variation in rates (Hz, labeled contour lines) for a range of η_c and η_{swap} values. The fixed values of η_d represent the reported values for SPAD (0.6) and SNSPD (0.96); 200 km, 500 km, 1000 km are representative distances. The color scale is provided as a visual guide and is consistent through subplots.

5.5 COMPARING GROUND-BASED AND SATELLITE-BASED QUANTUM LINKS

A prospect that emerges at large distances is the possibility of using satellites to establish the quantum link. By sending data directly through space the need for a QR and associated complexities can be side stepped. The curves shown in the figure 38 serve as first order approximation on rates. We show curves for ground-based link (GBL) using first generation

repeaters (with $\eta_d = 0.96, \eta_c = 0.9$) – non-deterministic gates with $\eta_{swap} = 0.9$ (green) and deterministic gates with $p_s = 1$ (cyan). For satellite-based link (SBL), there are several models that have been analyzed in literature. These cover the use of low earth orbit (LEO, at 500-2000 km), middle earth orbit (MEO) and geostationary (GEO, at 36000 km) satellites along with various combinations of ground/satellite receiver/transmitter configurations, as reviewed in [131]. LEO offers the highest rates (due to proximity and thereby lower loss) but a limited operation time window due to its high relative velocity. MEO (GEO) satellites, on the other hand, have lower (zero) relative velocity but suffer from higher losses [132]. For comparison with GBL we consider the scenario where a LEO satellite serves as the transmitter i.e. the source of the two photon Bell pair. For this case, a value of 1.1 Hz has been reported in literature and this has been included in figure 38 as a reference (dashed black line) [133]. To estimate for the case of a single LEO satellite, we used the reported value of 64 dB channel loss, which is been treated as constant for the length range shown here as it satisfied the criterion (>15 degree satellite elevation) over which the research report a steady 64-68.5 dB loss [133]. Further, based on the reported values, we assume an entangled pair source of 10^7 Hz. The rate obtained after these considerations is then adjusted to account for the fact that the LEO satellite had a window of ~275s per day for communication with the stations of interest. This gives us the solid black line which shows that it performs better than GBL (green line) at distances over 1500 km. The reported value of 1.1 Hz would be achievable (when averaged over a day) with more such satellites giving continuous coverage. These estimates are comparable to that presented in a recent work on satellite networks [134]. This implies that the GBL to SBL threshold will be between 500-1500 km based on the number of satellites (figure 38).

We also note that changes in any of the underlying assumptions will shift these curves and change these crossover points. Our intent here is to show that we can expect such crossover points to

emerge over a few hundred kms for a reasonable set of values. These estimates support the idea that the first generation GBL might be best suited for short distances and could be supported over longer distances supplementing with LEO satellites and even longer ranges using GEO satellites, ultimately utilizing a mixed architecture [47] for a globe spanning quantum link.

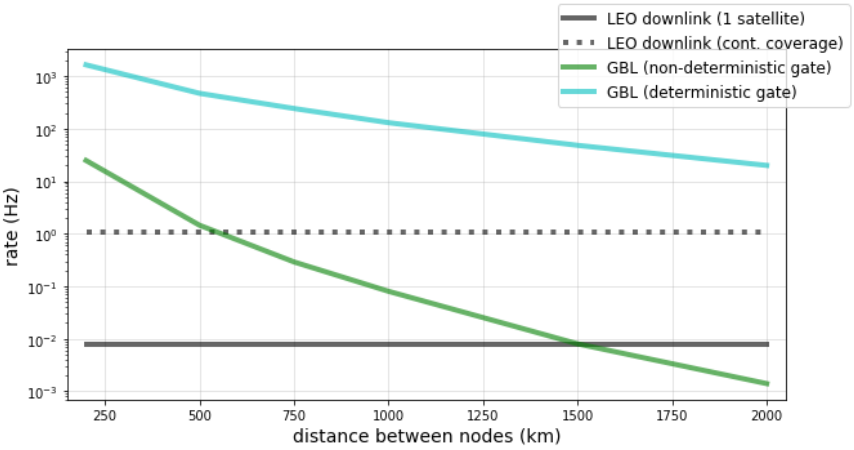

Figure 38 We compare the average rate between two end nodes via ground based link (GBL) with first generation QR using ($\eta_d = 0.96, \eta_c = 0.9, \eta_{gate} = 0.9$) – using non-deterministic (green) and deterministic (cyan) gates ($\eta_{gate} = 0.99$). Also shown are values for LEO satellite capable of transmitting photon Bell pairs (at 10^7 Hz) for the case of a single satellite (solid black) and continuous coverage using multiple satellites (dashed black) based on reported data.

5.6 CONCLUSION

In this paper we have examined the effect of device and material parameters for key components of a scalable solid-state QR on the system level performance of a quantum link using established models.

A host of improvements in detector and material technologies is moving us to the point where short links of low data rate repeaters might soon become practical. We estimate that using reported detector and estimated coupling efficiencies, rates over 10 Hz at 200 km are possible. This drops to ~1Hz for 500 km and sub-Hz values for links > 1000 km. Higher data rates over longer distances using first generation QRs will require major improvements in these efficiencies. Further, even

with near-ideal detectors and coupling efficiency practical rates at inter-city distances are only possible with deterministic swap gates. We also estimate that the required coherence time of the matter qubits, for the values explored in figure 37, is in the range 1.1 - 275 ms – a condition that is satisfied by many of the candidates. Finally, we compare the rates for GBL and SBL and estimate the crossover distance to be somewhere between 500-1500 km.

Our analysis of near-term outlook has allowed us to lay out a framework that could guide the goals for material scientists (e.g. the rate targets can guide coherence time goals) and engineers (e.g. choice of protocol, form of device) interested in the device aspect of quantum technologies. The *detector* and *memory blocks* in our estimates are "ready" with more development needed on the *control block* and the interfaces between these blocks. Our next step would be to bring in the energy/operation and production costs associated with building such a system.

5.7 ACKNOWLEDGEMENT

The authors would like to thank H. Bernien (University of Chicago), S. Chatterjee (University of California, Berkeley) and T. Ladd (Hughes Research Laboratory) for helpful discussions. This work was supported by the "Center for Novel Pathways to Quantum Coherence in Materials", an Energy Frontier Research Center funded by the U.S. Department of Energy, Office of Science, Basic Energy Sciences, under Award No. DE-AC02-05CH11231. This work was also supported by the U.S. Department of Energy, Office of Science, Office of Basic Energy Sciences (Grant #KC0202022). This work was also supported by the U.S. Department of Energy, Office of Science, Q-NEXT National Quantum Information Science Research Center. S.G. acknowledges the Vannevar Bush Fellowship under the program sponsored by the Office of the Undersecretary of Defense for Research and Engineering [OUSD (R&E)] and the Office of Naval Research as the executive manager for the grant. L.J. acknowledges the support from the NSF (EFMA-1640959) and the Packard Foundation (2013-39273).

5.8 SUPPLEMENTARY INFORMATION

Key device and materials specifications for a repeater enabled quantum internet

Manish Kumar Singh[1, +], Liang Jiang[1], David D. Awschalom[1,2], Supratik Guha[1,3]

[1]Pritzker School of Molecular Engineering, University of Chicago, Chicago, IL 60637, USA

[2]Center for Molecular Engineering and Materials Science Division, Argonne National Laboratory, Lemont, IL 60439, USA

[3]Center for Nanoscale Materials & Physical Sciences & Engineering Directorate, Argonne National Laboratory, Lemont, Illinois 60439

[+]Corresponding author: Manish Kumar Singh (manishks@uchicago.edu)

5.8.1 Creating long quantum links

We discuss a linear link of length L between two points A and B (fig 39(a)). The direct transmission has a limited range as the efficiency drops sharply with L when sending a photon directly as shown in figure 40 for three representative wavelengths – emission from Sr^{+} (422 nm, loss ~30dB/km), diamond NV center (637nm, loss ~6dB/km) and C-band Er^{3+} (~1536nm, loss 0.2dB/km). To overcome this, the distance can be divided into shorter segments of length L_0 (fig 39(b)) with a QR at each node. Each QR (represented by black rectangles) has two matter qubits (red and blues circles). An entanglement is established between each repeater pair (fig 39(c), (d)) using a Bell state measurement (BSM) setup using two single photon detectors [1]–[3]. This is followed by entanglement swapping - a series of operations on the qubits at QR1 that extends the entanglement to the outer nodes A and B (fig 39(e)). This swapping can be performed using either two photon quantum interference [4] or using non-linear quantum gates in some systems e.g. trapped ions [5], NV center in diamond [6].

In a first-generation link with multiple QR nodes, the entanglement swap is performed in a series of steps (fig 39) and the success/failure or measurement result from each step is transmitted between nearest neighbors in the link using classical channels. This limits the maximum achievable rates for a given value of L and L_0. Second and third generation QR operations that are not limited by heralded classical communication have challenging materials demands, and the anticipated realization is further out in time [7]–[9]. Our discussion therefore will be focused on nearer-term feasible first-generation repeaters.

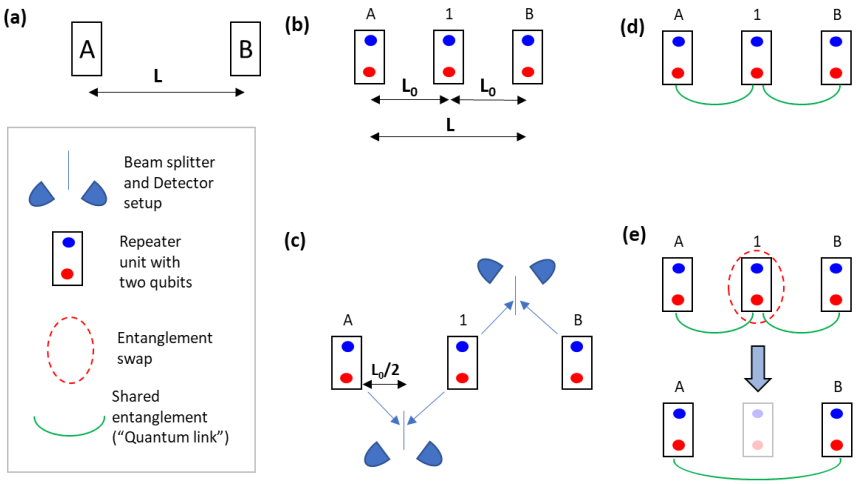

Figure 39 (a-b) A repeater reduces the distance over which a photon needs to be directly transmitted, here from L to L/2. (c-d) Using a BSM setup entanglement can be created between the nodes at A & 1, and 1 & B (e) An entanglement swapping operation connects the two separate entanglements creating a longer "quantum link".

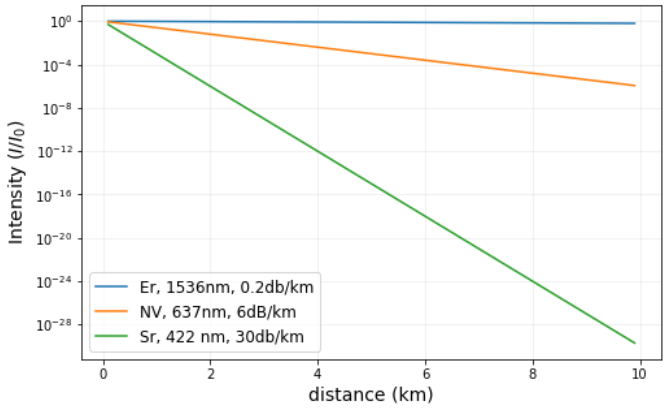

Figure 40 Comparing transmission losses for different photon-travel-distances in the state-of-the-art fiber optics cable used in communication for three candidates. This highlights the need for frequency conversion.

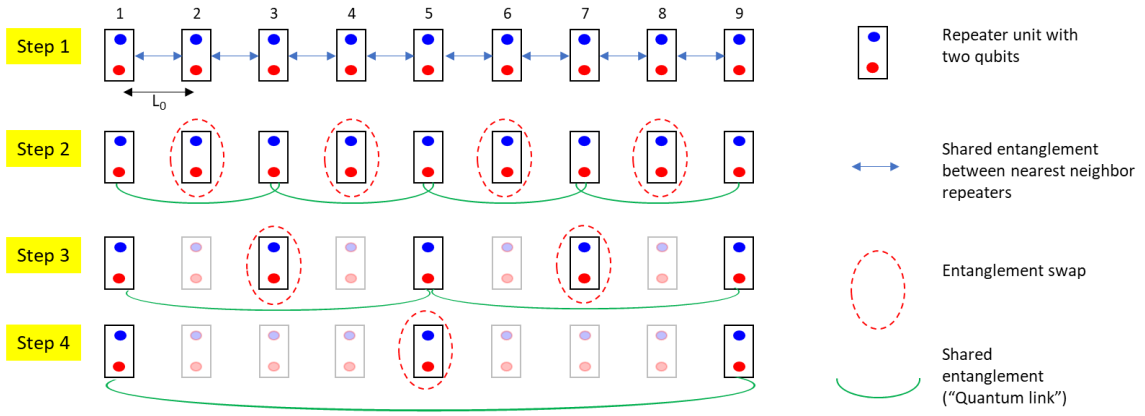

Figure 41 Standard approach in the first generation QR involves sequential extension of entanglement through swaps (Step 2-4).

5.8.2 A method to improve link rates using idle repeaters

In the standard approach that was introduced in the previous section (figure 41), more and more repeaters become idle as the chain progresses, with half the repeaters idle at step 3 and 75% by step 4. We propose a new method (triQ) that utilizes these idle repeaters in the standard approach to improve the time it takes to entangle the qubits. For the case of nine repeaters, we start at step T1 by creating an entanglement between QRs 2&3, 3&4, 6&7, 7&8. In step T2 we concurrently do the following: (a) entanglement swap at QR 3&7 such that the entanglement now extends to 2&4 and 6&8 as show in figure 42. (b) entanglement creation between QR 4-5 & 5-6. For step T3, we again perform two concurrent processes: (a) entanglement swap at QR 4 and 6, which extend the entanglement to 2&5 and 5&8. (b) entanglement creation between QR 1&2 and QR 8&9. At the step T4, two swap operations are performed at QR2 and QR8 resulting in links between QR 1&5 and QR 5&9. At the final step, T5, an entanglement swap at QR5 results in the desired quantum link between QR 1&9. At this step we also concurrently start the inner loop using the repeaters 2,3,4 and 6,7,8 that are free at the beginning of this step. Note that this is the same operation as in step T1 and this is how we now start an *inner loop* while the original loop progresses to higher link lengths. At step 9, a similar *inner loop* can again be created, as three contiguous QR

again become free. The proposed method can readily be generalized to N steps. For a process with N steps, the number of possible *inner loops* existing simultaneous at different levels is given by ⌊N/4⌋. Used in conjunction with the standard QR approach (figure S5) modest gains can be achieved. This algorithm is presented in figure S6 as a flowchart.

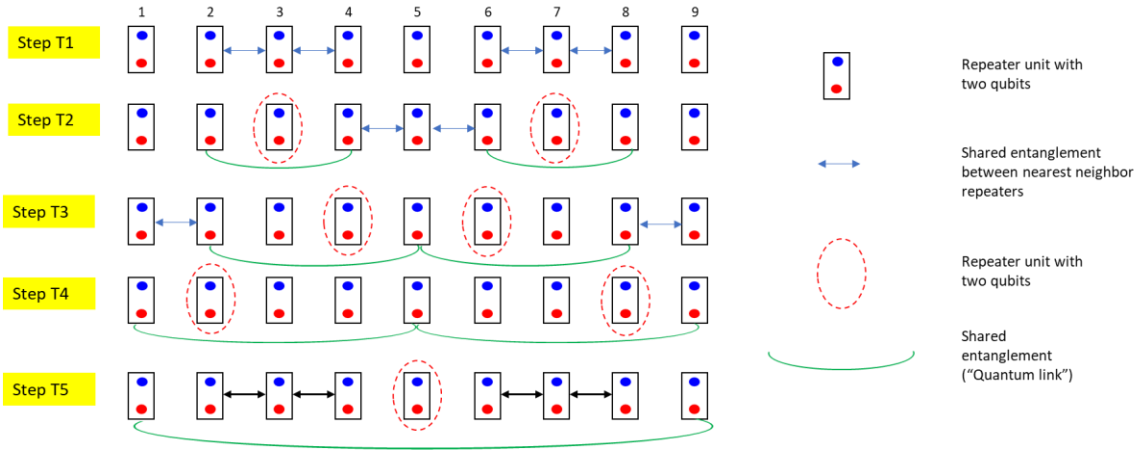

Figure 42 Proposed method (TriQ) utilizes the idle resources to start an inner loop thus giving gains in time required to connect.

To estimate the gains from this approach a monte carlo simulation was performed, and the results are shown in figure 45 – TriQ results in modest gains in the time it takes to entangle (up to 13% in our example).

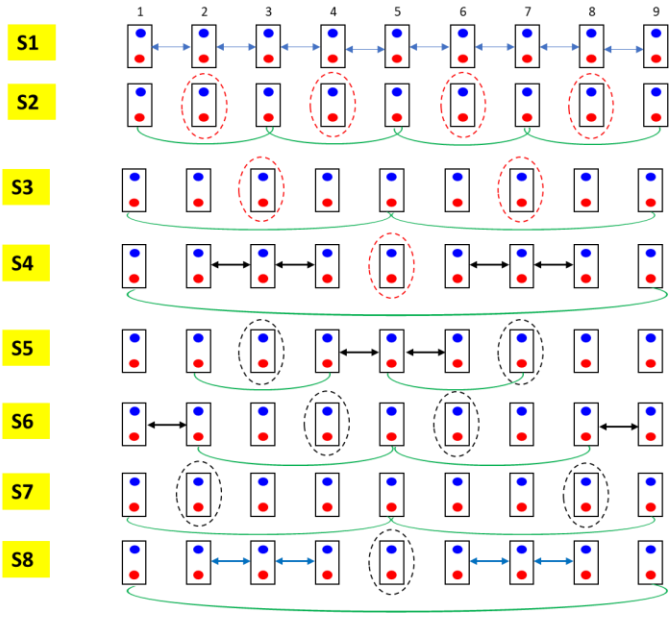

Figure 43 A schematic for the case of 9 repeaters (8 links) where triQ is used in conjunction (starting at step S5) with the standard approach

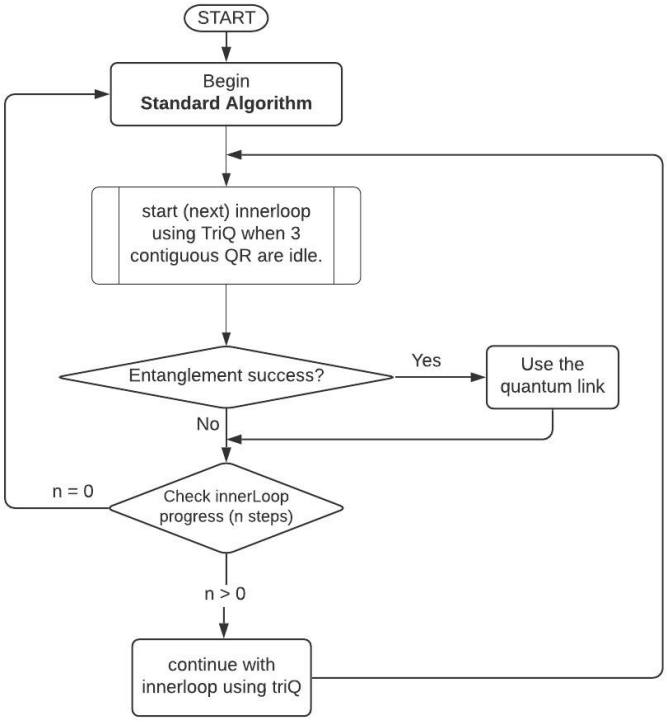

Figure 44 The algorithm for implementing the proposed approach (triQ) in conjunction with the standard approach

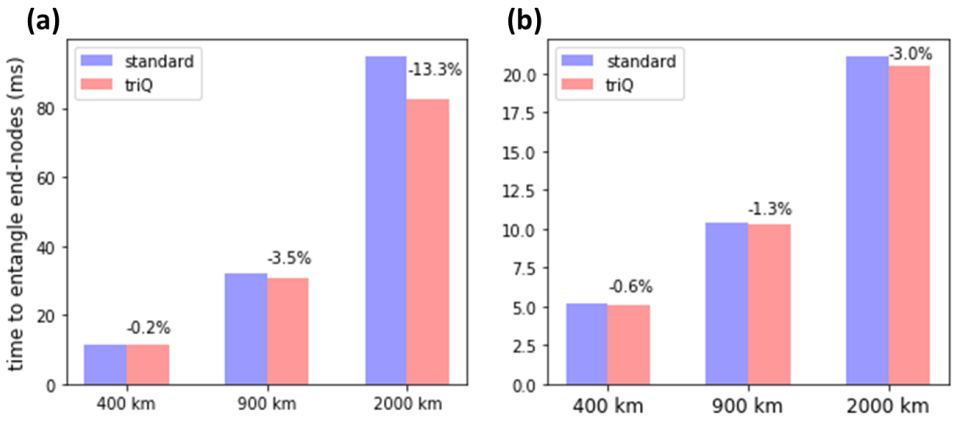

Figure 45 We compare the entanglement time for the standard approach (blue) and triQ (red). There are modest increases in speed (>10%) for triQ in the given scenario. L0=20 was used. (a) This represents the case for the value set ($\eta_d = 0.9, \eta_c = 0.6, p_{sg} = 0.9$) (b) This simulates the results for the value set ($\eta_d = 0.99, \eta_c = 0.99, p_{sg} = 0.99$). Clearly, the improvements are more significant in the case of lower efficiency components

5.8.3 Additional parameters of interest for quantum link performance

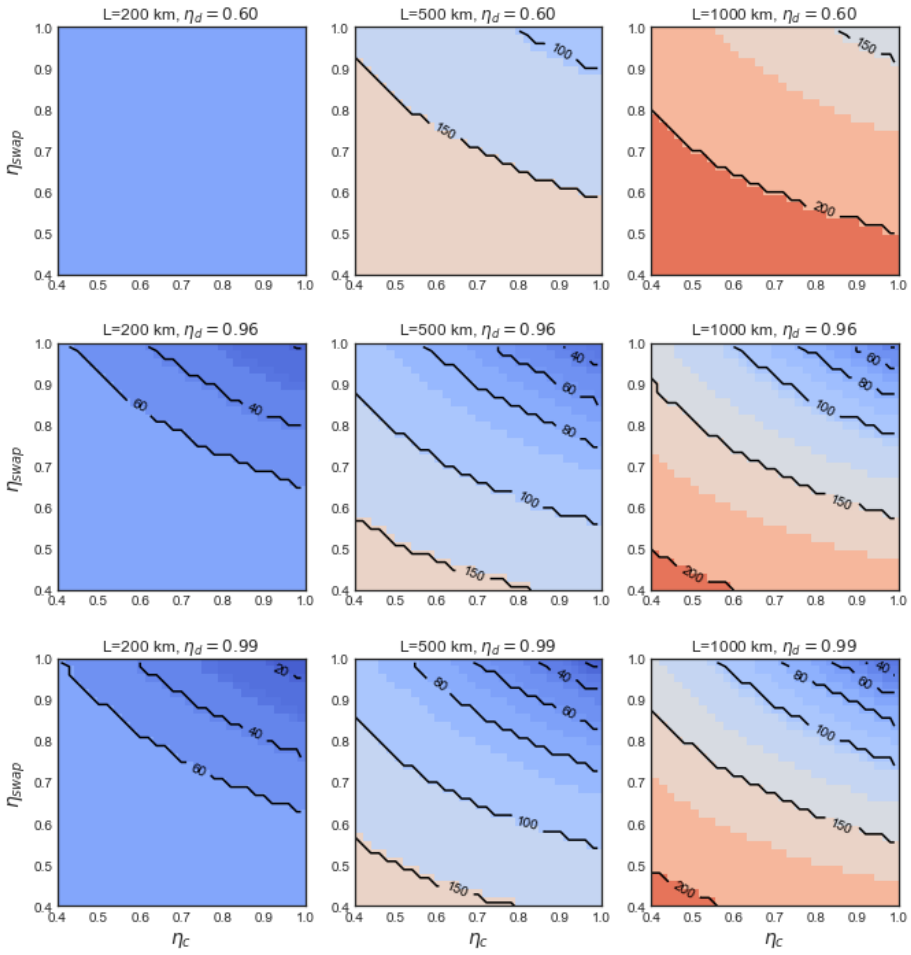

Figure 46 Optimal L_0 for the case depicted in fig 37. The trade-off between lower operation vs transmission loss leads to large L_0 at low operational efficiencies and smaller L_0 at higher efficiencies

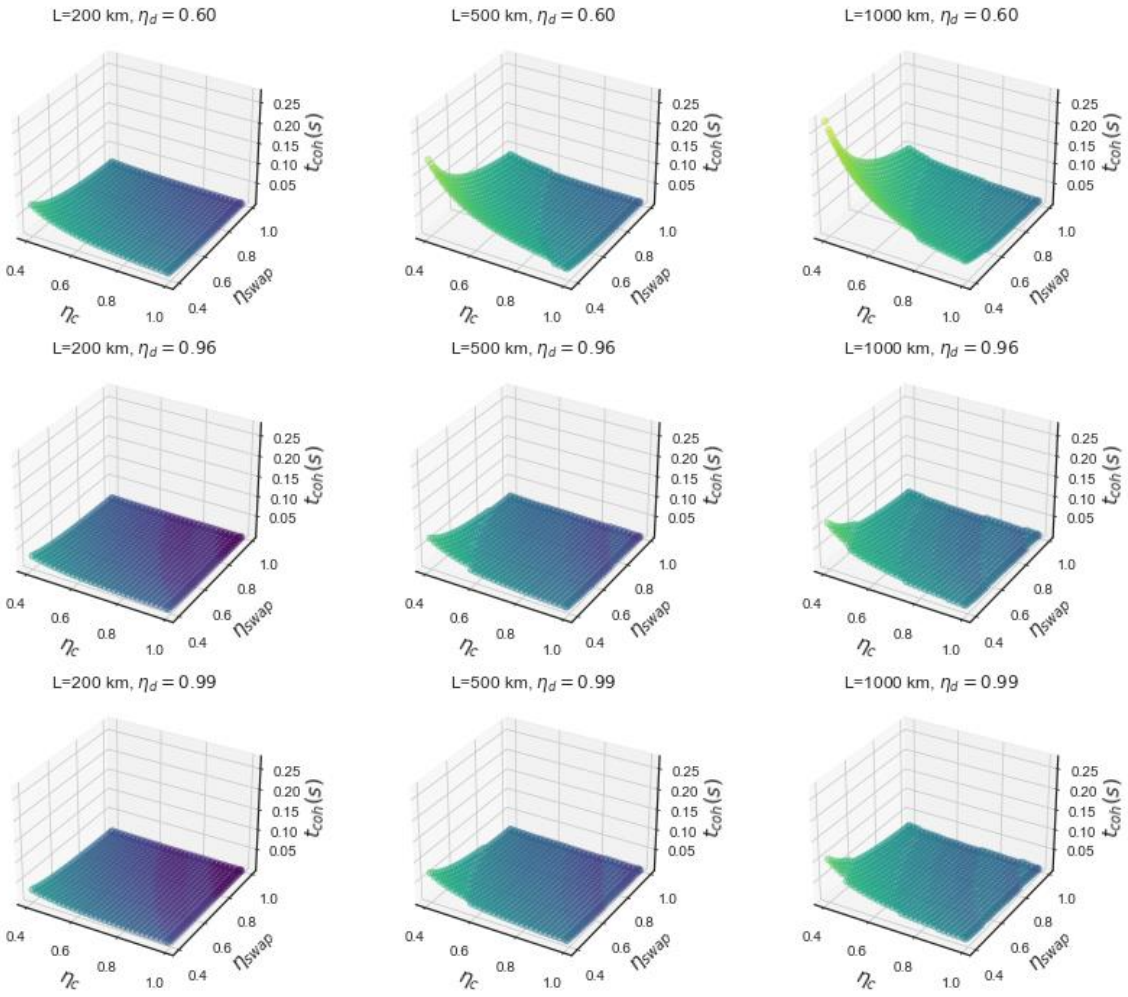

Figure 47 Memory requirement on the matter qubit (t_{coh}) is dictated primarily by the first step that creates entanglement creation between nearest neighbors and by additional from any classical communication that is required. As a result, the minimum required t_{coh} is highest for long distance connection with low efficiency component. The requirement for the case discussed in fig 37 varies between 1.1-275 ms – this is a range that a variety of qubits can meet.

6 OUTLOOK

REIs offer a promising candidate for quantum memories, and recently protocols for performing gate operations using these ions have also been proposed, laying out a path to quantum computing[48,52,143,144]. The shielding of 4f electrons by the full 5s, 5p is unique to REIs and gives them the ability to largely retain their optical and spin properties irrespective of the host lattice that they are in, as it shields the atoms from the local electric fields[28]. This important property allows us to embed REI in a suitable host that is silicon compatible. In a thin film form factor with silicon compatibility, this would unlock the ability to borrow nanofabrication methods from the semiconductor industry and develop quantum devices on this platform at scale.

However, thin-film growth and tailoring of the qubit properties using material engineering is only part of the challenge. To truly leverage the scalability potential, the thin film needs to satisfy additional criteria. As highlighted throughout the thesis and especially in chapter 4, fabricability is key for unlocking scale. The material stack should be processable in a silicon photonics foundry – preferably using an inductive plasma-based reactive ion etch (ICP RIE). For example, thick films of Y_2O_3 have been hard to fabricate with multiple issues from sidewall roughness to film warping; TiO_2, on the other hand, is easily etched using a chlorine-based etch and can be improved further using an optimized mixture of etchants. CeO_2 and STO, the other films that our group is exploring – while useful for understanding the nature of defect/host interaction – are also expected to have similar issues as Y_2O_3 with etch pattern transfer and roughness.

A material scientist, by training, is familiar with the methods of material growth and characterization, which involves discovering the direct growth window, material quality characterization using AFM, TEM, XRD, etc. In the past, driven by the needs of the semiconductor industry, electron mobility (and factors impacting it) had become an important metric. It becomes

a little more challenging for a "quantum material scientist" working on materials for quantum/quantum-optics application as the material of interest is not the thin films itself, but the active dopants/defects in there, a different set of metrics focused on the dopant becomes important as a part of primary characterization – inhomogeneous and homogeneous linewidth, spectral diffusion etc. Additionally, surface roughness becomes especially important for optics application – as it leads to scattering losses in waveguides and other structures. It is then paramount that a fast cycle time between growth and these new characterizations be established to accelerate material optimization. It is also important to understand that in some cases, the concentration of these defects needs to be below direct detection limits and additional fabrication of waveguides/photonic crystals on the platform becomes necessary (as it increases the optical depth) to characterize the properties listed above. This might require the researcher to build a dedicated setup and/or establish close collaborations with colleagues across fields. From my perspective, the next step for material development would be the optimization of existing thin-film stacks and the development of more complex heterostructures, e.g., Si/film/Si, to enable a platform that could be used to fabricate slot waveguides. This would involve development, optimization, and simultaneous integration of multiple growth techniques – a challenging problem. Given the long chain of dependencies, the key here would be minimizing the cycle time for fast feedback and development. Once we have such a platform with the desired properties, the next step is the development of devices that allow us to engineer the light-matter interaction, giving us the capability to address single atoms and couple light in and out of these structures with high efficiencies.

When looking at this in the context of integrated quantum photonics and erbium-doped oxide on SOI could provide the central platform on which several of these capabilities could be directly integrated[145,146]. This includes capabilities that can be implemented in the Erbium-doped thin films

layer, such as memory (ensemble and single atom), potentially a quantum resource generator, transduction (optical to microwave) capabilities using erbium energy levels, etc. Other capabilities that have been developed on SOI, SIN, etc., such as squeezed light generation, quantum entanglement, and teleportation, could be developed onto the silicon layer. Furthermore, heterogeneous integration of other materials such as $LiNbO_3$ demonstrated on a silicon platform[147] can be brought in to add to these capabilities.

A silicon-compatible thin films platform for REI-based qubits has the potential to significantly improve our capabilities when it comes to generating, storing, and manipulating quantum information. In this work, we have (1) identified the key material properties that would be needed for a qubit platform used for a quantum network and (2) shown the promise and challenges of developing such a platform. Future efforts directed toward better understanding the material properties and demonstrating further integration can be expected to be extremely fruitful.

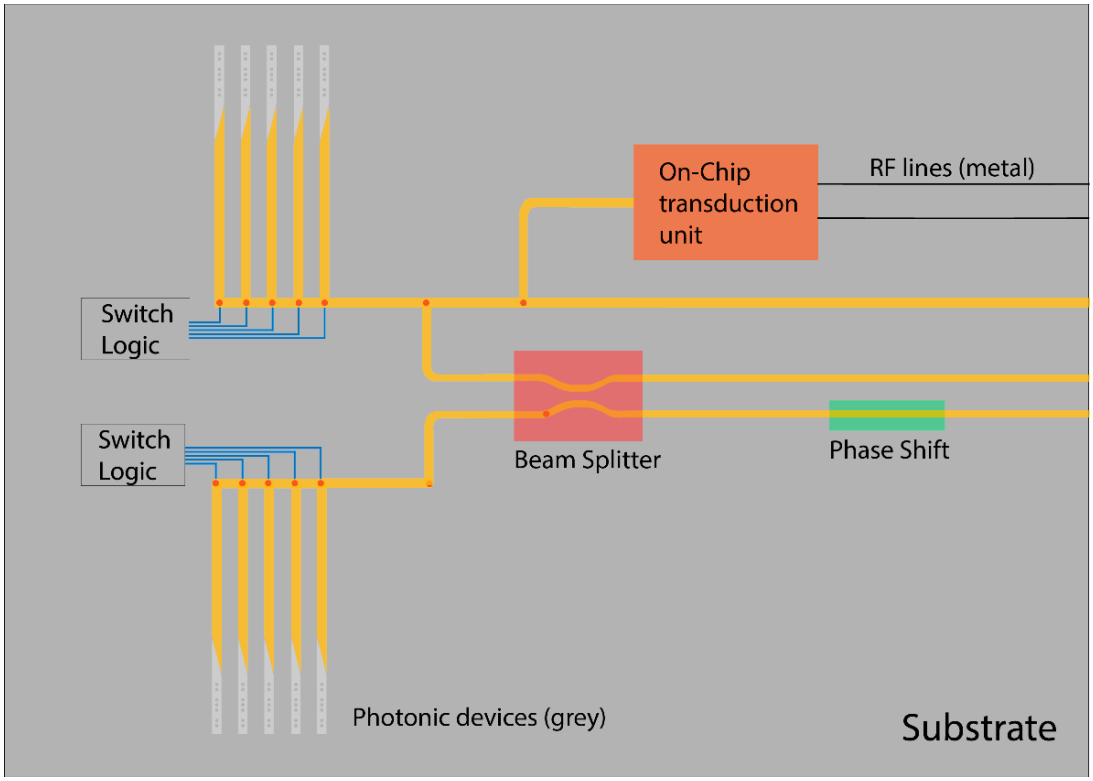

Figure 48 A schematic showing the range of capabilities – storage, transduction, etc. – that could potentially be integrated onto the REI/oxide platform. By integrating storage and control elements, full-fledged capabilities (both optical and microwave) could be developed.

REFERENCES

[1] M. Pompili, S.L.N. Hermans, S. Baier, H.K.C. Beukers, P.C. Humphreys, R.N. Schouten, R.F.L. Vermeulen, M.J. Tiggelman, L. dos Santos Martins, B. Dirkse, S. Wehner, and R. Hanson, Science (80-.). **372**, 259 (2021).

[2] V. Zepf, in *Rare Earths Ind.*, edited by I. Borges De Lima and W. Leal Filho (Elsevier, Boston, 2016), pp. 3–17.

[3] M. Rančić, M.P. Hedges, R.L. Ahlefeldt, and M.J. Sellars, Nat. Phys. **14**, 50 (2018).

[4] M. Zhong, M.P. Hedges, R.L. Ahlefeldt, J.G. Bartholomew, S.E. Beavan, S.M. Wittig, J.J. Longdell, and M.J. Sellars, Nature **517**, 177 (2015).

[5] M.K. Singh, L. Jiang, D.D. Awschalom, and S. Guha, IEEE Trans. Quantum Eng. **2**, 1 (2021).

[6] J.M. Kindem, J.G. Bartholomew, P.J.T. Woodburn, T. Zhong, I. Craiciu, R.L. Cone, C.W. Thiel, and A. Faraon, Phys. Rev. B **98**, 24404 (2018).

[7] J.G. Bartholomew, J. Rochman, T. Xie, J.M. Kindem, A. Ruskuc, I. Craiciu, M. Lei, and A. Faraon, Nat. Commun. **11**, 3266 (2020).

[8] C. Monroe, D.M. Meekhof, B.E. King, W.M. Itano, and D.J. Wineland, Phys. Rev. Lett. **75**, 4714 (1995).

[9] C.A. Sackett, D. Kielpinski, B.E. King, C. Langer, V. Meyer, C.J. Myatt, M. Rowe, Q.A. Turchette, W.M. Itano, D.J. Wineland, and C. Monroe, Nature **404**, 256 (2000).

[10] D. Kielpinski, C. Monroe, and D.J. Wineland, Nature **417**, 709 (2002).

[11] C.D. Bruzewicz, J. Chiaverini, R. McConnell, and J.M. Sage, Appl. Phys. Rev. **6**, 21314 (2019).

[12] J.M. Martinis and K. Osborne, ArXiv Prepr. Cond-Mat/0402415 (2004).

[13] M. Kjaergaard, M.E. Schwartz, J. Braumüller, P. Krantz, J.I.-J. Wang, S. Gustavsson, and W.D. Oliver, Annu. Rev. Condens. Matter Phys. **11**, 369 (2020).

[14] M. Ritala and M. Leskelä, in *Handb. Thin Film.* (Elsevier, 2002), pp. 103–159.

[15] A. Prakash, J. Dewey, H. Yun, J.S. Jeong, K.A. Mkhoyan, and B. Jalan, J. Vac. Sci. Technol. A **33**, 60608 (2015).

[16] H.J. Kimble, Nature **453**, 1023 (2008).

[17] A.I. Lvovsky, B.C. Sanders, and W. Tittel, Nat. Photonics **3**, 706 (2009).

[18] W. Tittel, M. Afzelius, T. Chaneliére, R. ~L. Cone, S. Kröll, S. ~A. Moiseev, and M. Sellars, Laser Photonics Rev. **4**, 244 (2010).

[19] D.M. Toyli, C.D. Weis, G.D. Fuchs, T. Schenkel, and D.D. Awschalom, Nano Lett. **10**, 3168 (2010).

[20] G. Wolfowicz, C.P. Anderson, A.L. Yeats, S.J. Whiteley, J. Niklas, O.G. Poluektov, F.J. Heremans, and D.D. Awschalom, Nat. Commun. **8**, 1876 (2017).

[21] A.M. Dibos, M. Raha, C.M. Phenicie, and J.D. Thompson, Phys. Rev. Lett. **120**, 243601 (2018).

[22] P. Goldner, A. Ferrier, and O. Guillot-Noël, Handb. Phys. Chem. Rare Earths **46**, 1 (2015).

[23] T. Zhong, J.M. Kindem, J.G. Bartholomew, J. Rochman, I. Craiciu, E. Miyazono, M. Bettinelli, E. Cavalli, V. Verma, S.W. Nam, F. Marsili, M.D. Shaw, A.D. Beyer, and A. Faraon, Science (80-.). (2017).

[24] N. Kunkel and P. Goldner, Zeitschrift Fur Anorg. Und Allg. Chemie **644**, (2018).

[25] D.D. Awschalom, R. Hanson, J. Wrachtrup, and B.B. Zhou, Nat. Photonics **12**, 516 (2018).

[26] M. Scarafagio, A. Tallaire, K.-J. Tielrooij, D. Cano, A. Grishin, M.-H. Chavanne, F.H.L. Koppens, A. Ringuedé, M. Cassir, D. Serrano, P. Goldner, and A. Ferrier, J. Phys. Chem. C **123**, 13354 (2019).

[27] J.G. Bartholomew, J. Rochman, J.M. Kindem, T. Zhong, I. Craiciu, A. Ruskuc, and A. Faraon, in *2018 Conf. Lasers Electro-Optics* (2018), pp. 1–2.

[28] G. Liu and B. Jacquier, editors , *Spectroscopic Properties of Rare Earths in Optical Materials* (Springer, 2005).

[29] S. Elliott, M. Fanciulli, and G. Scarel, *Rare Earth Oxide Thin Films* (Springer Berlin Heidelberg, 2006).

[30] M. Rančić, M.P. Hedges, R.L. Ahlefeldt, and M.J. Sellars, Nat. Phys. **14**, 50 (2017).

[31] T. Zhong, J.M. Kindem, E. Miyazono, and A. Faraon, Nat. Commun. **6**, 8206 (2015).

[32] S. Guha, N.A. Bojarczuk, and V. Narayanan, Appl. Phys. Lett. **80**, 766 (2002).

[33] C.W. Nieh, Y.J. Lee, W.C. Lee, Z.K. Yang, A.R. Kortan, M. Hong, J. Kwo, and C.-H. Hsu, Appl. Phys. Lett. **92**, 061914 (2008).

[34] S.C. Choi, M.H. Cho, S.W. Whangbo, C.N. Whang, S.B. Kang, S.I. Lee, and M.Y. Lee, Appl. Phys. Lett. **71**, 903 (1997).

[35] M.-H. Cho, D.-H. Ko, Y.K. Choi, I.W. Lyo, K. Jeong, T.G. Kim, J.H. Song, and C.N. Whang, J. Appl. Phys. **89**, 1647 (2001).

[36] J.M. McCormack, P.R. Platt, and R.K. Saxer, J. Chem. Eng. Data **16**, 167 (1971).

[37] J. Rosenthal and L. Yarmus, Rev. Sci. Instrum. **37**, 381 (1966).

[38] A.Y. Bresgunov, A.A. Dubinsky, O.G. Poluektov, G.A. Vorob'eva, and Y.S. Lebedev, J. Chem. Soc.{,} Faraday Trans. **86**, 3185 (1990).

[39] L. Pauling and M.D. Shappell, Zeitschrift Für Krist. **75**, 128 (1930).

[40] S. Guha and V. Narayanan, Phys. Rev. Lett. **98**, 196101 (2007).

[41] V. Narayanan, S. Guha, M. Copel, N.A. Bojarczuk, P.L. Flaitz, and M. Gribelyuk, Appl. Phys. Lett. **81**, 4183 (2002).

[42] B.M. Tissue, N.J. Cockroft, L. Lu, D.C. Nguyen, and W.M. Yen, J. Lumin. **48**–**49**, 477 (1991).

[43] K.W. Jang and R.S. Meltzer, Phys. Rev. B **52**, 6431 (1995).

[44](n.d.).

[45] J.B. Gruber, K.L. Nash, D.K. Sardar, U. V. Valiev, N. Ter-Gabrielyan, and L.D. Merkle, J. Appl. Phys. **104**, 023101 (2008).

[46] C.W. Thiel, T. Böttger, and R.L. Cone, J. Lumin. **131**, 353 (2011).

[47] C. Simon, Nat. Photonics **11**, 678 (2017).

[48] A. Faraon, A. Ruskuc, I. Craiciu, J.M. Kindem, J.G. Bartholomew, J.H. Rochman, and M. Lei, in *Quantum Comput. Commun. Simul.*, edited by P.R. Hemmer and A.L. Migdall (SPIE, 2021).

[49] D. Lago-Rivera, S. Grandi, J. V Rakonjac, A. Seri, and H. de Riedmatten, Nature **594**, 37 (2021).

[50] P. Stevenson, C.M. Phenicie, I. Gray, S.P. Horvath, S. Welinski, A.M. Ferrenti, A. Ferrier, P. Goldner, S. Das, R. Ramesh, R.J. Cava, N.P. de Leon, and J.D. Thompson, (2021).

[51] T. Zhong and G. Philippe, Nanophotonics **8**, 2003 (2019).

[52] A. Kinos, D. Hunger, R. Kolesov, K. Mølmer, H. de Riedmatten, P. Goldner, A. Tallaire, L. Morvan, P. Berger, S. Welinski, K. Karrai, L. Rippe, S. Kröll, and A. Walther, (2021).

[53] M. Raha, S. Chen, C.M. Phenicie, S. Ourari, A.M. Dibos, and J.D. Thompson, Nat. Commun. **11**, 1605 (2020).

[54] J.M. Kindem, A. Ruskuc, J.G. Bartholomew, J. Rochman, Y.Q. Huan, and A. Faraon, Nature **580**, 201 (2020).

[55] M. Kadoshima, M. Hiratani, Y. Shimamoto, K. Torii, H. Miki, S. Kimura, and T. Nabatame, Thin Solid Films **424**, 224 (2003).

[56] M.K. Bera and C.K. Maiti, Mater. Sci. Semicond. Process. **9**, 909 (2006).

[57] C.M. Phenicie, P. Stevenson, S. Welinski, B.C. Rose, A.T. Asfaw, R.J. Cava, S.A. Lyon, N.P. de Leon, and J.D. Thompson, Nano Lett. **19**, 8928 (2019).

[58] B. Jalan, R. Engel-Herbert, J. Cagnon, and S. Stemmer, J. Vac. Sci. Technol. A **27**, 230 (2009).

[59] R.W. Mar and R.G. Bedford, J. Less Common Met. **71**, 317 (1980).

[60] R. Engel-Herbert, B. Jalan, J. Cagnon, and S. Stemmer, J. Cryst. Growth **312**, 149 (2009).

[61] M.D. McDaniel, A. Posadas, T.Q. Ngo, A. Dhamdhere, D.J. Smith, A.A. Demkov, and J.G. Ekerdt, J. Vac. Sci. Technol. B **30**, 04E111 (2012).

[62] W. Luo, C. Fu, R. Li, Y. Liu, H. Zhu, and X. Chen, Small **7**, 3046 (2011).

[63] Y. Liu, W. Luo, H. Zhu, and X. Chen, J. Lumin. **131**, 415 (2011).

[64] M.K. Singh, A. Prakash, G. Wolfowicz, J. Wen, Y. Huang, T. Rajh, D.D. Awschalom, T. Zhong,

and S. Guha, APL Mater. **8**, 031111 (2020).

[65] N. Kunkel, J.G. Bartholomew, L. Binet, A. Ikesue, and P. Goldner, J. Phys. Chem. C **120**, 13725 (2016).

[66] E.Z.C. and A.T. and J.L. and A.F. and P.G. and N.G. and M. Afzelius, New J. Phys. **20**, 53013 (2018).

[67] M. Ishii, S. Komuro, and T. Morikawa, J. Appl. Phys. **94**, 3823 (2003).

[68] N. Harada, A. Tallaire, D. Serrano, A. Seyeux, P. Marcus, X. Portier, C. Labbé, P. Goldner, and A. Ferrier, Mater. Adv. (2022).

[69] H.S. Baik, M. Kim, G.-S. Park, S.A. Song, M. Varela, A. Franceschetti, S.T. Pantelides, and S.J. Pennycook, Appl. Phys. Lett. **85**, 672 (2004).

[70] F. Paumier, R.J. Gaboriaud, and A.R. Kaul, Cryst. Eng. **5**, 169 (2002).

[71] L. Weiss, A. Gritsch, B. Merkel, and A. Reiserer, Optica **8**, 40 (2021).

[72] S. Zafar, A. Callegari, V. Narayanan, and S. Guha, Appl. Phys. Lett. **81**, 2608 (2002).

[73] J.A.B. Pérez, M. Courel, R.C. Valderrama, I. Hernández, M. Pal, F.P. Delgado, and N.R. Mathews, Vacuum **169**, 108873 (2019).

[74] H.-C. Liu, Y.-H. Lin, and W. Hsu, Microsyst. Technol. **10**, 29 (2003).

[75] W.J. Munro, K. Azuma, K. Tamaki, and K. Nemoto, IEEE J. Sel. Top. Quantum Electron. **21**, 78 (2015).

[76] S. Muralidharan, L. Li, J. Kim, N. Lütkenhaus, M.D. Lukin, and L. Jiang, Sci. Rep. **6**, 20463 (2016).

[77] H.-J. Briegel, W. Dür, J.I. Cirac, and P. Zoller, Phys. Rev. Lett. **81**, 5932 (1998).

[78] W. Dür, H.-J. Briegel, J.I. Cirac, and P. Zoller, Phys. Rev. A **59**, 169 (1999).

[79] B. Hensen, H. Bernien, A.E. Dréau, A. Reiserer, N. Kalb, M.S. Blok, J. Ruitenberg, R.F.L. Vermeulen, R.N. Schouten, C. Abellán, W. Amaya, V. Pruneri, M.W. Mitchell, M. Markham, D.J. Twitchen, D. Elkouss, S. Wehner, T.H. Taminiau, and R. Hanson, Nature **526**, 682 (2015).

[80] Y. Yu, F. Ma, X.-Y. Luo, B. Jing, P.-F. Sun, R.-Z. Fang, C.-W. Yang, H. Liu, M.-Y. Zheng, X.-P. Xie, W.-J. Zhang, L.-X. You, Z. Wang, T.-Y. Chen, Q. Zhang, X.-H. Bao, and J.-W. Pan, Nature **578**, 240 (2020).

[81] J. Yin, Y.-H. Li, S.-K. Liao, M. Yang, Y. Cao, L. Zhang, J.-G. Ren, W.-Q. Cai, W.-Y. Liu, S.-L. Li, R. Shu, Y.-M. Huang, L. Deng, L. Li, Q. Zhang, N.-L. Liu, Y.-A. Chen, C.-Y. Lu, X.-B. Wang, F. Xu, J.-Y. Wang, C.-Z. Peng, A.K. Ekert, and J.-W. Pan, Nature **582**, 501 (2020).

[82] M. Pompili, S.L.N. Hermans, S. Baier, H.K.C. Beukers, P.C. Humphreys, R.N. Schouten, R.F.L. Vermeulen, M.J. Tiggelman, L. dos Santos Martins, B. Dirkse, S. Wehner, and R. Hanson, Science (80-.). **372**, 259 (2021).

[83] C. Simon, H. de Riedmatten, M. Afzelius, N. Sangouard, H. Zbinden, and N. Gisin, Phys. Rev. Lett. **98**, 190503 (2007).

[84] L. Childress, J.M. Taylor, A.S. S\orensen, and M.D. Lukin, Phys. Rev. A **72**, 52330 (2005).

[85] F. Rozp\ifmmode \mbox\ke\else \ke\fidek, R. Yehia, K. Goodenough, M. Ruf, P.C. Humphreys, R. Hanson, S. Wehner, and D. Elkouss, Phys. Rev. A **99**, 52330 (2019).

[86] J.B. Brask, I. Rigas, E.S. Polzik, U.L. Andersen, and A.S. S\orensen, Phys. Rev. Lett. **105**, 160501 (2010).

[87] L. Jiang, J.M. Taylor, K. Nemoto, W.J. Munro, R. Van Meter, and M.D. Lukin, Phys. Rev. A **79**, 32325 (2009).

[88] S. Muralidharan, C.-L. Zou, L. Li, and L. Jiang, Phys. Rev. A **97**, 52316 (2018).

[89] L. Childress, J.M. Taylor, A.S. S\orensen, and M.D. Lukin, Phys. Rev. Lett. **96**, 70504 (2006).

[90] L. Jiang, J.M. Taylor, N. Khaneja, and M.D. Lukin, Proc. Natl. Acad. Sci. **104**, 17291 (2007).

[91] S. Bratzik, H. Kampermann, and D. Bru\ss, Phys. Rev. A **89**, 32335 (2014).

[92] R. Van Meter, T.D. Ladd, W.J. Munro, and K. Nemoto, IEEE/ACM Trans. Netw. **17**, 1002 (2009).

[93] R. Van Meter, T. Satoh, T.D. Ladd, W.J. Munro, and K. Nemoto, Netw. Sci. **3**, 82 (2013).

[94] M. Pant, H. Krovi, D. Towsley, L. Tassiulas, L. Jiang, P. Basu, D. Englund, and S. Guha, Npj Quantum Inf. **5**, 25 (2019).

[95] P. van Loock, W. Alt, C. Becher, O. Benson, H. Boche, C. Deppe, J. Eschner, S. Höfling, D. Meschede, P. Michler, F. Schmidt, and H. Weinfurter, Adv. Quantum Technol. **3**, 1900141 (2020).

[96] F. Rozp\kedek, K. Goodenough, J. Ribeiro, N. Kalb, V.C. Vivoli, A. Reiserer, R. Hanson, S. Wehner, and D. Elkouss, Quantum Sci. Technol. **3**, 34002 (2018).

[97] N. None, (n.d.).

[98] D. Awschalom, K.K. Berggren, H. Bernien, S. Bhave, L.D. Carr, P. Davids, S.E. Economou, D. Englund, A. Faraon, M. Fejer, S. Guha, M. V Gustafsson, E. Hu, L. Jiang, J. Kim, B. Korzh, P. Kumar, P.G. Kwiat, M. Lon\ifmmode \checkc\else č\fiar, M.D. Lukin, D.A.B. Miller, C. Monroe, S.W. Nam, P. Narang, J.S. Orcutt, M.G. Raymer, A.H. Safavi-Naeini, M. Spiropulu, K. Srinivasan,

S. Sun, J. č\fikovi\ifmmode \acutec\else ć\fi, E. Waks, R. Walsworth, A.M. Weiner, and Z. Zhang, PRX Quantum **2**, 17002 (2021).

[99] P. Gargini, in *GaAs IC Symp. IEEE Gall. Arsenide Integr. Circuits Symp. 22nd Annu. Tech. Dig. 2000. (Cat. No.00CH37084)* (2000), pp. 3–5.

[100] S.T. Walsh, R.L. Boylan, C. McDermott, and A. Paulson, Technol. Forecast. Soc. Change **72**, 213 (2005).

[101] F.K. Asadi, S.C. Wein, and C. Simon, Quantum Sci. Technol. **5**, 45015 (2020).

[102] N. Sangouard, C. Simon, H. de Riedmatten, and N. Gisin, Rev. Mod. Phys. **83**, 33 (2011).

[103] N. Bar-Gill, L.M. Pham, A. Jarmola, D. Budker, and R.L. Walsworth, Nat. Commun. **4**, 1743 (2013).

[104] X. Rong, J. Geng, F. Shi, Y. Liu, K. Xu, W. Ma, F. Kong, Z. Jiang, Y. Wu, and J. Du, Nat. Commun. **6**, 8748 (2015).

[105] Y. Wang, M. Um, J. Zhang, S. An, M. Lyu, J.-N. Zhang, L.-M. Duan, D. Yum, and K. Kim, Nat. Photonics **11**, 646 (2017).

[106] L.J. Stephenson, D.P. Nadlinger, B.C. Nichol, S. An, P. Drmota, T.G. Ballance, K. Thirumalai, J.F. Goodwin, D.M. Lucas, and C.J. Ballance, Phys. Rev. Lett. **124**, 110501 (2020).

[107] C.J. Ballance, T.P. Harty, N.M. Linke, M.A. Sepiol, and D.M. Lucas, Phys. Rev. Lett. **117**, 60504 (2016).

[108] Y. Wang, A. Kumar, T.-Y. Wu, and D.S. Weiss, Science (80-.). **352**, 1562 (2016).

[109] J. Hofmann, M. Krug, N. Ortegel, L. Gérard, M. Weber, W. Rosenfeld, and H. Weinfurter,

Science (80-.). **337**, 72 (2012).

[110] T. Xia, M. Lichtman, K. Maller, A.W. Carr, M.J. Piotrowicz, L. Isenhower, and M. Saffman, Phys. Rev. Lett. **114**, 100503 (2015).

[111] H. Levine, A. Keesling, G. Semeghini, A. Omran, T.T. Wang, S. Ebadi, H. Bernien, M. Greiner, V. Vuleti\ifmmode \acutec\else ć\fi, H. Pichler, and M.D. Lukin, Phys. Rev. Lett. **123**, 170503 (2019).

[112] K.C. Miao, J.P. Blanton, C.P. Anderson, A. Bourassa, A.L. Crook, G. Wolfowicz, H. Abe, T. Ohshima, and D.D. Awschalom, (2020).

[113] A. Bourassa, C.P. Anderson, K.C. Miao, M. Onizhuk, H. Ma, A.L. Crook, H. Abe, J. Ul-Hassan, T. Ohshima, N.T. Son, G. Galli, and D.D. Awschalom, Nat. Mater. **19**, 1319 (2020).

[114] C.T. Nguyen, D.D. Sukachev, M.K. Bhaskar, B. Machielse, D.S. Levonian, E.N. Knall, P. Stroganov, R. Riedinger, H. Park, M. Lon\ifmmode \checkc\else č\fiar, and M.D. Lukin, Phys. Rev. Lett. **123**, 183602 (2019).

[115] T. Ishikawa, K.-M.C. Fu, C. Santori, V.M. Acosta, R.G. Beausoleil, H. Watanabe, S. Shikata, and K.M. Itoh, Nano Lett. **12**, 2083 (2012).

[116] R. Zhao, T. Tanttu, K.Y. Tan, B. Hensen, K.W. Chan, J.C.C. Hwang, R.C.C. Leon, C.H. Yang, W. Gilbert, F.E. Hudson, K.M. Itoh, A.A. Kiselev, T.D. Ladd, A. Morello, A. Laucht, and A.S. Dzurak, Nat. Commun. **10**, 5500 (2019).

[117] A. Dréau, A. Tchebotareva, A. El Mahdaoui, C. Bonato, and R. Hanson, Phys. Rev. Appl. **9**, 64031 (2018).

[118] J. Zhang, M.A. Itzler, H. Zbinden, and J.-W. Pan, Light Sci. Appl. **4**, e286 (2015).

[119] S. Chan, A. Halimi, F. Zhu, I. Gyongy, R.K. Henderson, R. Bowman, S. McLaughlin, G.S. Buller, and J. Leach, Sci. Rep. **9**, 8075 (2019).

[120] Y. Nambu, S. Takahashi, K. Yoshino, A. Tanaka, M. Fujiwara, M. Sasaki, A. Tajima, S. Yorozu, and A. Tomita, Opt. Express **19**, 20531 (2011).

[121] L.C. Comandar, B. Fröhlich, J.F. Dynes, A.W. Sharpe, M. Lucamarini, Z.L. Yuan, R. V Penty, and A.J. Shields, J. Appl. Phys. **117**, 83109 (2015).

[122] A. Tada, N. Namekata, and S. Inoue, Jpn. J. Appl. Phys. **59**, 72004 (2020).

[123] Y.-Q. Fang, W. Chen, T.-H. Ao, C. Liu, L. Wang, X.-J. Gao, J. Zhang, and J.-W. Pan, (2020).

[124] D. V Reddy, R.R. Nerem, A.E. Lita, S.W. Nam, R.P. Mirin, and V.B. Verma, in *2019 Conf. Lasers Electro-Optics* (2019), pp. 1–2.

[125] J. Borregaard, P. Kómár, E.M. Kessler, M.D. Lukin, and A.S. S\orensen, Phys. Rev. A **92**, 12307 (2015).

[126] M. Pompili, S.L.N. Hermans, S. Baier, H.K.C. Beukers, P.C. Humphreys, R.N. Schouten, R.F.L. Vermeulen, M.J. Tiggelman, L. dos S. Martins, B. Dirkse, S. Wehner, and R. Hanson, (2021).

[127] N. Kalb, A.A. Reiserer, P.C. Humphreys, J.J.W. Bakermans, S.J. Kamerling, N.H. Nickerson, S.C. Benjamin, D.J. Twitchen, M. Markham, and R. Hanson, Science (80-.). **356**, 928 (2017).

[128] C.H. Bennett, G. Brassard, S. Popescu, B. Schumacher, J.A. Smolin, and W.K. Wootters, Phys. Rev. Lett. **76**, 722 (1996).

[129] T.B.H. Tentrup, W.M. Luiten, R. van der Meer, P. Hooijschuur, and P.W.H. Pinkse, New J. Phys. **21**, 123044 (2019).

[130] S. Kanai, F.J. Heremans, H. Seo, G. Wolfowicz, C.P. Anderson, S.E. Sullivan, G. Galli, D.D. Awschalom, and H. Ohno, (2021).

[131] R. Bedington, J.M. Arrazola, and A. Ling, Npj Quantum Inf. **3**, 30 (2017).

[132] M. Aspelmeyer, T. Jennewein, M. Pfennigbauer, W.R. Leeb, and A. Zeilinger, IEEE J. Sel. Top. Quantum Electron. **9**, 1541 (2003).

[133] J. Yin, Y. Cao, Y.-H. Li, S.-K. Liao, L. Zhang, J.-G. Ren, W.-Q. Cai, W.-Y. Liu, B. Li, H. Dai, G.-B. Li, Q.-M. Lu, Y.-H. Gong, Y. Xu, S.-L. Li, F.-Z. Li, Y.-Y. Yin, Z.-Q. Jiang, M. Li, J.-J. Jia, G. Ren, D. He, Y.-L. Zhou, X.-X. Zhang, N. Wang, X. Chang, Z.-C. Zhu, N.-L. Liu, Y.-A. Chen, C.-Y. Lu, R. Shu, C.-Z. Peng, J.-Y. Wang, and J.-W. Pan, Science (80-.). **356**, 1140 (2017).

[134] S. Khatri, A.J. Brady, R.A. Desporte, M.P. Bart, and J.P. Dowling, Npj Quantum Inf. **7**, 4 (2021).

[135] J.-W. Pan, D. Bouwmeester, H. Weinfurter, and A. Zeilinger, Phys. Rev. Lett. **80**, 3891 (1998).

[136] H. Bernien, B. Hensen, W. Pfaff, G. Koolstra, M.S. Blok, L. Robledo, T.H. Taminiau, M. Markham, D.J. Twitchen, L. Childress, and R. Hanson, Nature **497**, 86 (2013).

[137] S.D. Barrett and P. Kok, Phys. Rev. A **71**, 60310 (2005).

[138] M. \ifmmode \dotZ\else Ż\fiukowski, A. Zeilinger, M.A. Horne, and A.K. Ekert, Phys. Rev. Lett. **71**, 4287 (1993).

[139] M. Riebe, T. Monz, K. Kim, A.S. Villar, P. Schindler, M. Chwalla, M. Hennrich, and R. Blatt, Nat. Phys. **4**, 839 (2008).

[140] N.M. Linke, M. Gutierrez, K.A. Landsman, C. Figgatt, S. Debnath, K.R. Brown, and C. Monroe, Sci. Adv. **3**, (2017).

[141] N. Ofek, A. Petrenko, R. Heeres, P. Reinhold, Z. Leghtas, B. Vlastakis, Y. Liu, L. Frunzio, S.M. Girvin, L. Jiang, M. Mirrahimi, M.H. Devoret, and R.J. Schoelkopf, Nature **536**, 441 (2016).

[142] R. Stricker, D. Vodola, A. Erhard, L. Postler, M. Meth, M. Ringbauer, P. Schindler, T. Monz, M. Müller, and R. Blatt, Nature **585**, 207 (2020).

[143] S. Bertaina, S. Gambarelli, A. Tkachuk, I.N. Kurkin, B. Malkin, A. Stepanov, and B. Barbara, Nat. Nanotechnol. **2**, 39 (2007).

[144] J.H. Wesenberg, K. M\olmer, L. Rippe, and S. Kröll, Phys. Rev. A **75**, 12304 (2007).

[145] J. Wang, F. Sciarrino, A. Laing, and M.G. Thompson, Nat. Photonics **14**, 273 (2020).

[146] E. Pelucchi, G. Fagas, I. Aharonovich, D. Englund, E. Figueroa, Q. Gong, H. Hannes, J. Liu, C.-Y. Lu, N. Matsuda, J.-W. Pan, F. Schreck, F. Sciarrino, C. Silberhorn, J. Wang, and K.D. Jöns, Nat. Rev. Phys. (2021).

[147] L. Chen, J. Nagy, and R.M. Reano, Opt. Mater. Express **6**, 2460 (2016).